AlloyManufacturingNet for discovery and design of hardness-elongation synergy in multi-principal element alloys

Sachin Poudel, Upadesh Subedi, Mohammed O.A. Hamid, Khem Gyanwali, Nele Moelans, Anna Timofiejczuk, Anil Kunwar

Graphical Abstract

AlloyManufacturingNet for discovery and design of hardness-elongation synergy in multi-principal element alloys.

Sachin Poudel,Upadesh Subedi,Mohammed O A Hamid,Khem Gyanwali,Nele Moelans,Anna Timofiejczuk,Anil Kunwar

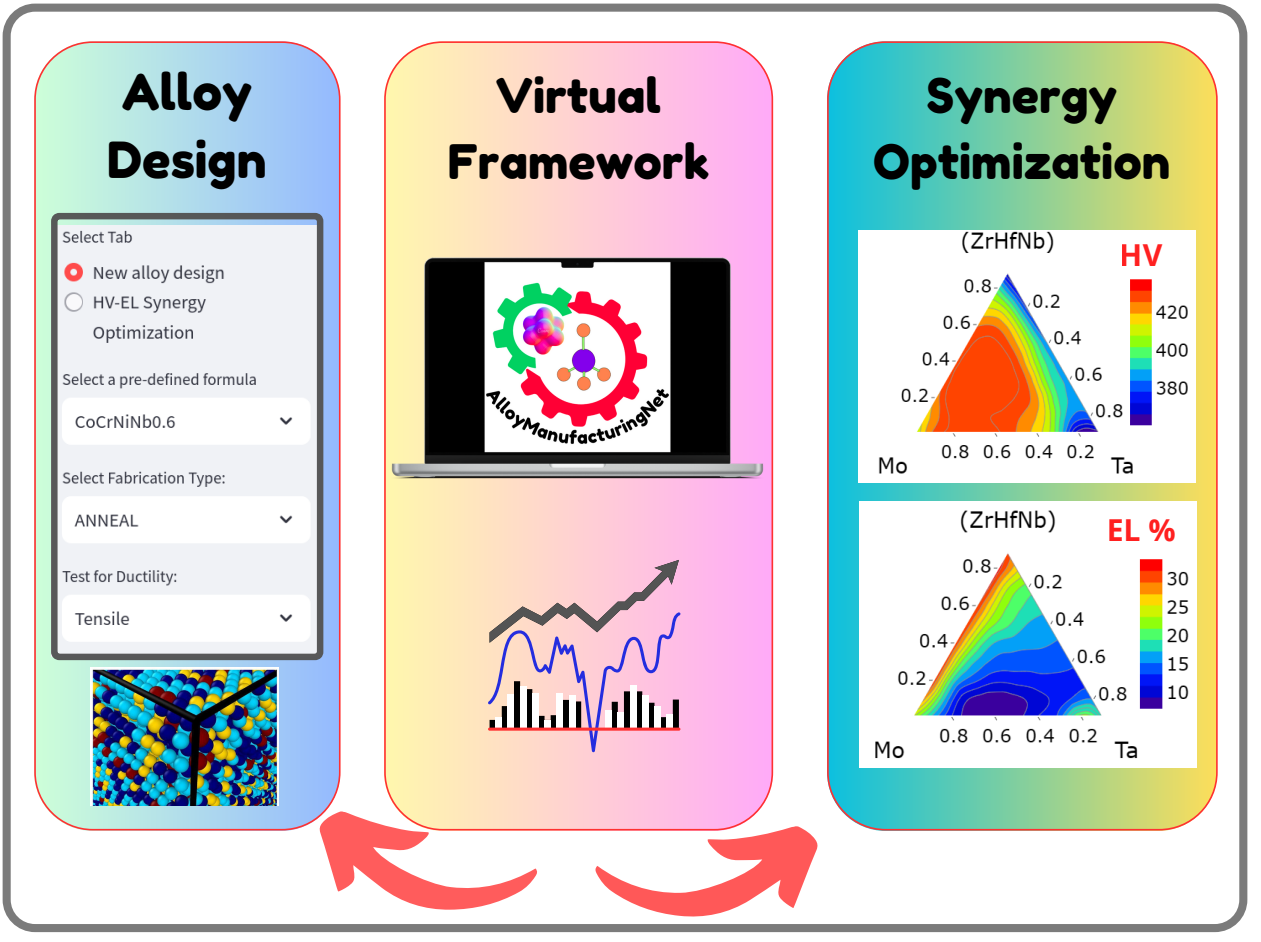

Highlights

AlloyManufacturingNet for discovery and design of hardness-elongation synergy in multi-principal element alloys.

Sachin Poudel,Upadesh Subedi,Mohammed O A Hamid,Khem Gyanwali,Nele Moelans,Anna Timofiejczuk,Anil Kunwar

- Elemental asymmetry factor a very relevant feature.
- Manufacturing route influences both hardness and elongation.
- Scale invariant composition optimization incorporated in AlloyManufacturingNet.
- Sintering maximizes hardness in Cr_x $W_y(ZrHfNb)_{1-x-y}$ and Cr_x $W_y(VNbTa)_{1-x-y}$ alloys.
- $CoCrNiNb_x$ alloy with x>0.25 exhibits hardness-ductility synergy.

AlloyManufacturingNet for discovery and design of hardness-elongation synergy in multi-principal element alloys.

Sachin Poudel[a,b], Upadesh Subedi[a], Mohammed O A Hamid[c], Khem Gyanwali[b,*], Nele Moelans[d], Anna Timofiejczuk[a] and Anil Kunwar[a,**]

[a]*Faculty of Mechanical Engineering, Silesian University of Technology, Konarskiego 18A, 44-100 Gliwice, Poland*

[b]*Department of Automobile and Mechanical Engineering, Thapathali Campus, Tribhuvan University, 44600 Kathmandu, Nepal*

[c]*Thermal Energy Systems Division, Mechanical Engineering Department, Faculty of Engineering, University of Khartoum, 11111 Khartoum, Sudan*

[d]*Department of Materials Engineering, KU Leuven, Kasteelpark Arenberg 44, 3001 Leuven, Belgium*

ARTICLE INFO

Keywords:
Multi-principal element alloys
Feature selection
Ensemble neural network
Hardness-ductility synergy
Scale invariant optimization
Digital Manufacturing

ABSTRACT

Located around the center of multicomponent phase space, multi-principal element alloys (MPEAs) are often characterized with a unique blend of contrasting physico-chemical properties, and have a good prospective of presenting hardness-ductility synergy. A datasets of MPEAs fabricated by casting, wrought, sintering, annealing procedures, was collected and the mean values for hardness and elongation was determined as 495.3 HV and 22.16 % respectively. After screening and processing the datasets with the help of feature selection by tools such as Pearson's correlation coefficient, multicollinearity analysis and principal component analysis, artificial neural networks (ANNs) were subsequently trained in this study. An ensemble of these networks known as AlloyManufacturingNet was then purposed as the prediction toolkit for the inverse alloy design in applications including metamorphic manufacturing. During the in-silico design of external elements doped ZrHfNb and VNbTa alloys for maximum hardness,the model has estimated that $Cr_{0.4}W_{0.5}(ZrHfNb)_{0.1}$ and $Cr_{0.5}W_{0.3}(VNbTa)_{0.2}$, both fabricated by sintering method, show hardness values of 684.49 and 733.42 HV respectively. While $Ti_{0.7}(ZrHfNb)_{0.3}$ prepared via annealing procedure shows the largest elongation of 43.52 % in the category of ZrHfNb-derived alloys, $Mo_{0.1}Ti_{0.8}(VNbTa)_{0.1}$ processed through the wrought process is estimated to have a maximum elongation of 34.36 % in the group of VNbTa-derived alloys. For establishment of the hardness-ductility synergy as required in structural applications, the composition spaces for given manufacturing routes have been searched with the machine learning model. In general, the MPEAs derived from base VNbTa alloy tend to perform better in context of possessing composition values having both the hardness and ductility above the aforementioned mean values. The machine learning based estimation was done in another MPEA, namely, $CoCrNiNb_x$ alloy to quantify the change in hardness with the change in Nb content, and the mechanistic insights were obtained via molecular dynamics simulations.

1. Introduction

The high entropy alloys (HEAs) ubiquitously also known as multi-principal element alloys (MPEAs) in literature are alloys that consist of five or more principal (or base) elements having an equal or near-equal proportion ranging from 5% to 35% of base elements in them [1, 2, 3, 4]. The Medium Entropy Alloys (MEAs) are the MPEAs consisting of three or four base elements [5]. The concept of HEAs was first introduced to the scientific community in 2004 by Yeh *et al.* [6]. Since their inception, HEAs have received attention in material design because of the possibility to obtain products with enhanced mechanical properties [7, 8, 9, 10], high hardness [11], greater wear resistance [12], outstanding high-temperature resistance [13, 14], fracture resistance [15], lower temperature ductility [16] among others. Thereby making multi component alloys an excellent choice for material design. The design of MPEAs is not a straightforward task as there can be an infinitely large combination of constituent elements and their proportions that can impart given set up features and propeties in the resulting alloys [17]. In addition to that, experiments on different

*Corresponding author
**Corresponding author
gyanwalikhem@ioe.edu.np (K. Gyanwali); anil.kunwar@polsl.pl (A. Kunwar)
ORCID(s): 0000-0003-1427-5550 (S. Poudel); 0000-0002-5527-1348 (U. Subedi); 0000-0001-7448-3584 (M.O.A. Hamid); 0000-0002-8740-159X (K. Gyanwali); 0000-0003-3361-2954 (N. Moelans); 0000-0003-2941-4955 (A. Timofiejczuk); 0000-0003-4295-5772 (A. Kunwar)

element compositions by trial and error consume both time and resources without any certainty of better outcomes. However, various techniques have been developed for the design of MPEAs from simple empirical rules [18, 19] to computational complex models like calculation of phase diagram (CALPHAD) [20], Density Functional Theory (DFT) [21], ab-inito calculations [22], and Molecular Dynamics (MD) [23, 24]. Recently, machine learning (ML) techniques have gained popularity in MPEA design because of their efficient computational time and cost in contrast to the first principal methods and CALPHAD [25, 26]. Artificial neural networks (ANN) are quite successful in phase prediction of compositionally complex alloys [27, 28].

Hardness is one of the crucial mechanical properties that have to be considered in material design because of its tendency to resist localized plastic deformation, indentation, and scratching. The dispersion in hardness values provides valuable physical and mechanical insights into material properties, reflecting inherent variability and aiding scientific understanding [29]. Wen et. al. presented an ML-based technique to obtain new MPEAs with high hardness values in Al-Co-Cr-Cu-Fe-Ni alloys taking 91 observations [30]. Although more datasets are available in the literature, this work studies the hardness of only specific MPEA systems. Chang et. al. used neural network model on 155 HEA samples [31] which considered an alloy system consisting of 8 elements only. Bhandari et. al. predicted the hardness of refractory HEA with 128 as-cast data observations [32]. All of these works show decent prediction accuracy. However, they are trained with at most 155 datasets and with a limited elemental framework of 6, 8 and a maximum of 17 by Bhandari et. al. This excludes considerable alloys, including refractory MPEA. Bakr et al predicted hardness on MPEA by taking 427 datasets consisting of 18 elements and manufactured by casting and powder metallurgy [33]. Beniwal et al presented an ensemble artificial neural network trained with 218 MPEAs consisting of 22 elements fabricated by casting, tested with separate 58 MPEAs (manufactured by casting and sintering method only) and features selected from 22 pool of alloys and elemental descriptors [34]. The study is successful in capturing the non-linear relationship between input features and hardness. However, the model was trained only for prediction of hardness feature, and does not include the estimation of elongation. It is therefore necessary to build an inclusive model that can express on the ducitility of MPEAs along with the information on the hardness. The ductility of material can be explained by yield strength, ultimate tensile strength, and elongation. Hard materials are unlikely to have large elongations. Liu et. al studied the empirical relation for the prediction of elongation on as-cast Al-Co-Cr-Fe-Ni MPEA by analyzing the volume fraction of different microstructures and the application of CALPHAD. Both root mean squared error and mean absolute error for the elongation obtained is 20.1 %. Among various properties predicted using the empirical method, the prediction of elongation has very low accuracy [20]. There has been no data-driven approach for the prediction of elongation in combination with hardness assessments for the MPEA.

The information on hardness is important as an alloy with high hardness usually has lower ductility which limits its design scope [37]. The high-temperature plastic deformation impacts the hardening kinetics, revealing differences in intensity tied to dislocation microstructure changes [38]. Also, the abrasion resistance of the material is dependent on the ductility in addition to the hardness. The hard and ductile alloy is found to have better wear resistance properties than the alloy with only a high hardness value [39]. Therefore, it is essential to study both hardness and elongation together in order to expand the design scope of the alloy. The percentage elongation is the ductility property of a material. Singh et al. [40] have recently introduced local-lattice distortion (LLD) metric as an estimator of the ductility for refractory multi-principal element alloys. The establishment of this quantum mechanical dimensionless metric for ductiliy opens the door to benchmark percentage elongation values of different sets of alloy compositions. Pugh's ratio, positive Cauchy Pressure and Valence Electron Concentration (VEC) are among the widely accepted indicators of material ductility [40, 41, 42, 43, 44, 45, 46]. A data-driven model constructed from the data encompassing these indicators can be a promising tool for the accurate foretelling of the percentage alloy of a new MPEA. The knowledge of both hardness and elongation is crucial so as to get desired applicability of the alloy. Most of the studies hitherto associated with hardness and elongation prediction uses small datasets, consisting of few elemental compositions, and fails to generalize the model for MPEAs manufactured by different techniques. Moreover, no study has been done to capture both the hardness and ductility of the MPEAs. There can be design limitations to come up with the desired combination of hardness and elongation in conventional alloys. That restriction can be avoided with the research in MPEA. Hence, a data-driven study on both hardness and elongation can provide an accelerated search for optimized MPEA.

Apart from the initial phases of digital manufacturing, computer numerical control (CNC) and additive manufacturing, a novel approach called metamorphic manufacturing, envisioned by researchers [47], has emerged. This method employs digitally controlled incremental forming [47, 48], including thermal manipulation, to create engineering components with site-specific properties governed by local microstructures [49]. HEA or MPEA are ideal for

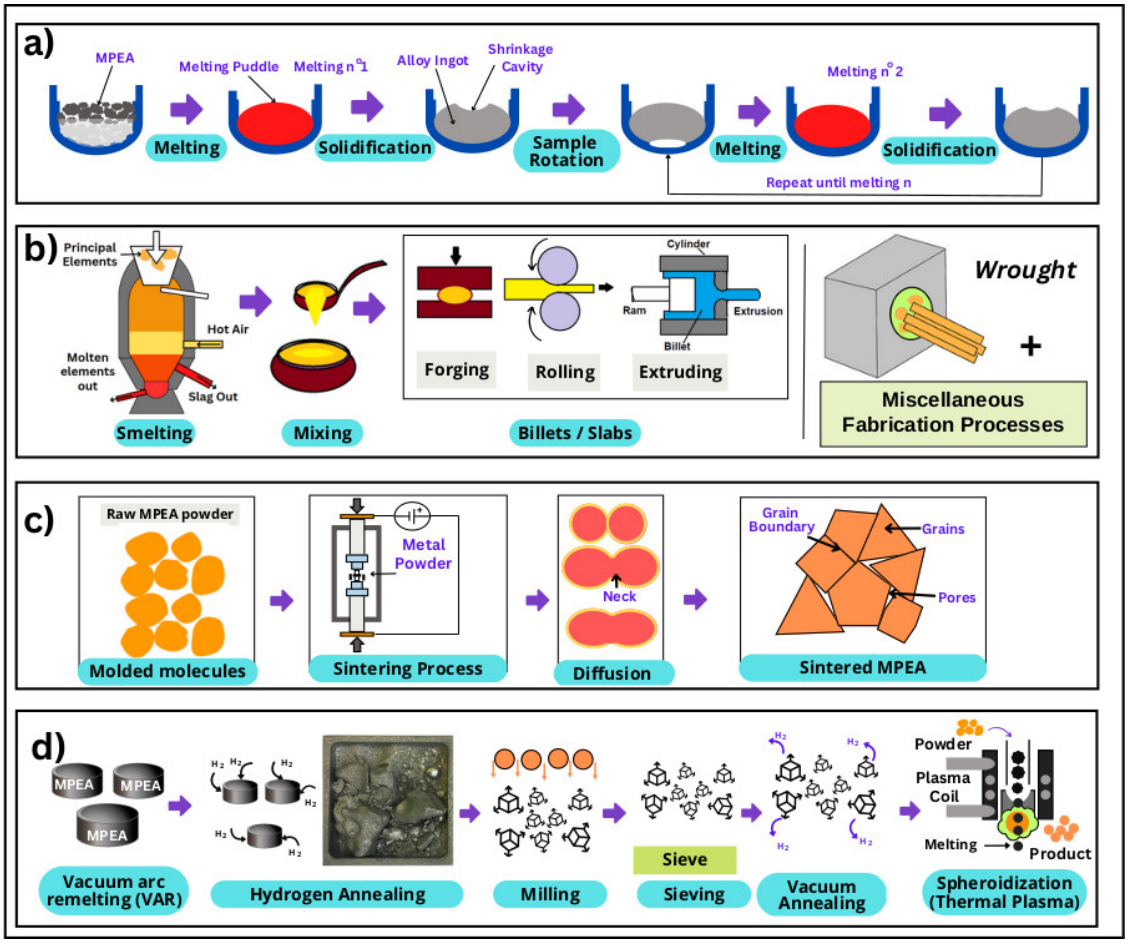

Figure 1: Common manufacturing routes for fabricating MPEAs. a) casting (CAT-A), **b)** Wrought and remaining all (CAT-B), **c)** powder metallurgy (CAT-C), and **d)** annealing (CAT-D). The image in a) is adopted from Paganotti et al [35] and in d) is adopted from Lee et al [36].

metamorphic manufacturing due to their capacity to modify structural and functional properties within a single alloy composition using diverse manufacturing methods or processing strategies [49]. Yet, the challenge lies in the limited availability of property databases for MPEAs at specific compositions and processing routes. Developing design charts encompassing material properties for a given MPEA at a particular composition across various manufacturing routes is crucial for advancing the metamorphic manufacturing sector rapidly.

In this study, alloy datasets were categorized into four main manufacturing routes: casting (CAT-A), wrought and miscellaneous (CAT-B), powder metallurgy (CAT-C), and annealing (CAT-D). Casting involves repeated cycles of melting and solidification using an MPEA crucible (Fig. 1 (a)) [35]. Wrought and miscellaneous processes encompass smelting, mixing, and forming billets or slabs (Fig. 1 (b)). Powder metallurgy includes sintering to create a sintered MPEA with pores between grains (Fig. 1 (c)), while annealing involves a series of processes like VAR, hydrogen annealing, milling, sieving, and vacuum annealing to form MPEA spheres from powder form using thermal plasma (Fig. 1 (d)) [36]. These categories correspond to different thermomechanical processing routes.

The machine learning toolkit **AlloyManufacturingNet** was developed to predict MPEA's contrasting mechanical properties: hardness and elongation. In our study, we emphasize the dataset's complexity's role in model accuracy. Simplifying complex datasets can enhance deep learning model accuracy, akin to "Kolmogorov complexity." Notable papers show reduced complexity boosts accuracy by curating and preprocessing data, striking a balance between advanced methods and data quality for better predictions [50, 51]. Extensive training data, including alloy and elemental descriptors, were obtained from published sources. Feature selection and hyperparameter tuning were used to

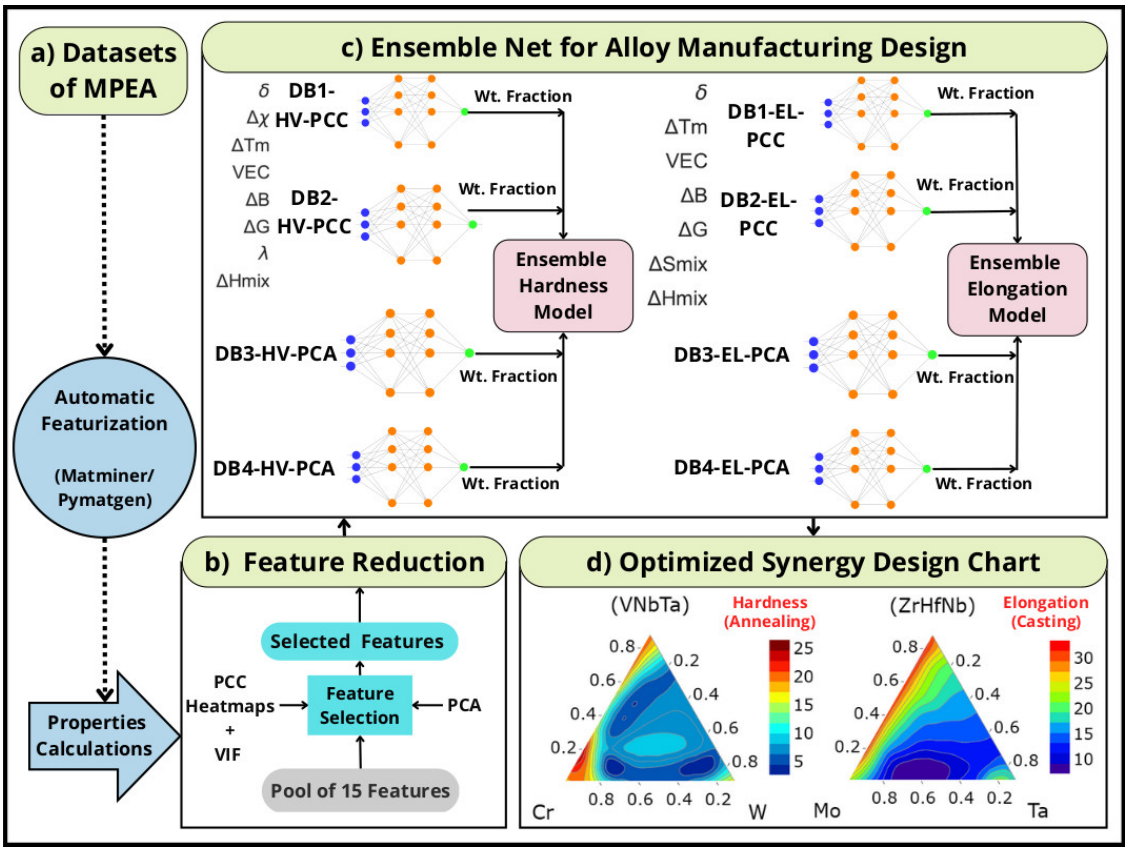

Figure 2: Schematic workflow for distilling the high entropy alloys dataset includes the processes such as auto featurization, feature reduction, learning the characteristics of data and designing property contours. a) The raw datasets obtained from the published literature is converted into numerical fingerprints, and the featurization is automated using Matminer and Pymatgen libraries. Property features are also obtained at this stage. **b)** The pool of property features is analyzed statistically using feature selection techniques such as PCC Heatmaps and principal component analysis (PCA). The datasets with reduced features are classified into different categories in accordance with the corresponding manufacturing technique. **c)** To account for the effects of categorical inputs, ensemble learning is implemented while training the neural network with hardness or elongation as an output feature. **d)** The prediction models are then utilized in the hardness and elongation design of a generic refractory MPEAs.

optimize the model. This trained model was applied to design alloys for hardness-ductility synergy, considering various constituent element compositions and manufacturing routes. Additionally, it assessed the impact of manufacturing routes on the properties of ZrHfNb and VNbTa alloys with different dopant elements and compositions. Molecular dynamics simulations were conducted for nanoindentation tests on $CoCrNiNb_x$ alloys produced by the casting process to elucidate predicted hardness properties.

2. Quantitative Profiling and Ensemble Machine Learning

The general workflow for data-driven design of hardness and elongation of multi-principal element alloys is presented in Fig. 2. As revealed in Fig. 2(a), it is first necessary to collect raw dataset of MPEAs from published literature. After performing numerical fingerprinting for the data, the designated features was screened for sorting out the important features as depicted in Fig. 2(b). This will help in the construction of a robust and physically intuitive machine learning model. In order to cope with the diversity in the origin ofdataset sources, ensemble models (Fig. 2(c)) can be trained with the data. The prediction models will then act as the source for generic design of MPEA materials.

2.1. Featurization and numerical fingerprinting

The first task in data-driven modeling is to collect the data from sources, and in this work, the data related to hardness and elongation were obtained from published works [6, 32, 34, 52, 53, 54, 55, 56, 57]. Only the experimentally validated and published data are considered in this work. The collected datasets are automatically featurized so as to obtain constituents element and their corresponding compositions. The pymatgen and matminer python libraries are used for the automatic featurization [58]. A pragmatic approach is taken by considering the nominal composition when the true composition of the material is unavailable or not well-documented. Additionally, for model training and testing, data specifically selected from tests conducted at room temperature is employed. The collected datasets in Fig. 3 encompass various alloy compositions, mechanical properties (hardness and elongation), fabrication methods, and phases. Four manufacturing route categories (CAT-A, CAT-B, CAT-C, and CAT-D) are depicted in bar charts for hardness (Fig. 3(a)) and elongation (Fig. 3(c)) data. Regarding the hardness data for MPEAs, initially, 706 observations were gathered, excluding binary alloys. To focus on high entropy alloys with 3 to 7 components, a filtering code was applied, resulting in 683 remaining observations, categorized by manufacturing type (Fig. 3(a)) and component count (Fig. 3(e)). The final hardness dataset included 22 elements (Fig. 3(b)). For the elongation datasets, comprising 353 observations with 26 elements (Fig. 3(c)), each MPEA had $3 \leq N \leq 9$ components shown in Fig. 3(g). Box plots visually conveyed phase structure information for hardness (Fig. 3(f)) and elongation (Fig. 3(h)) datasets, showing both single- and multi-phase MPEAs. Hardness values ranged from 109 to 1084 HV (Fig. 3(f)), while elongation values in Fig. 3(h) spanned from 0 to 96.2%. The experimental specimens reported in the abovementioned sources of the elongation test datasets of MPEAs all have the length / thickness within the range of few millimetres, strain rate in the range of 1.0×10^{-4}-10×10^{-4} s^{-1} and total loading time of 15-20 s. The specimens for compression based deformation were generally of cylindrical geometry whereas those for tensile ductility tests were found to be mostly of rectangular geometry. In order to accomodate the differential effects of tension and compression tests in the percentage elongation values, the data are categorized into compression test only, tensile test specimens only and mixed (compression + tensile tests)

To ensure the robustness of a data-driven approach for MPEA material design, it's essential that the selected features carry physically meaningful information. This task becomes particularly crucial given the high-dimensional materials design space, especially in the case of HEAs [58]. The feature pool, outlined in Table 1, encompasses diverse categories. The first category includes terms derived from Hume-Rothery rules, such as atomic size difference (δ), electronegativity ($\Delta\chi$), and Valence Electron Concentration (VEC). Features like δ and $\Delta\chi$ are relevant as they capture relative atomic sizes and chemical compatibility among constituent elements in MPEAs, respectively. Another category incorporates concepts from materials and alloy thermodynamics, encompassing Enthalpy of Mixing (ΔH_{mix}), Entropy of Mixing (ΔS_{mix}), Average Molar Heat Capacity (δ_{Cp}), Geometrical Parameter (λ), and Dimensionless Parameter (Ω). Notably, Ω stands out as a feature because it amalgamates ΔH_{mix}, ΔS_{mix}, and the average melting temperature $T_m(K)$ of an MPEA, providing an alternative solution for the numerical fingerprinting of HEAs' Gibbs energy of mixing complexities. Additionally, the feature pool includes the average melting temperature $T_m(K)$ of an MPEA and its asymmetry ΔT_m as independent features, further enhancing the robustness and relevance of data-driven methods for MPEA material design.

A comprehensive pool of 15 input features was constructed, as detailed in Table 1. These features encompass a range of elemental and alloying descriptors, including Mean Atomic Radius difference (δ), Electronegativity asymmetry ($\Delta\chi$), Average Melting Temperature ($T_m(K)$), Melting Temperature asymmetry (ΔT_m), Valence Electron Concentration (VEC), Average Atomic Number (AN), Thermal Conductivity (K), Average Bulk Modulus (B), Average Shear Modulus (G), Shear Modulus Asymmetry (ΔG), Average Molar Heat Capacity (δ_{Cp}), Entropy of Mixing asymmetry (ΔS_{mix}), Enthalpy of Mixing asymmetry (ΔH_{mix}), Geometrical Parameter (λ), and Dimensionless parameter (Ω). The mathematical expressions used for numerical fingerprinting of these features are detailed in **Supplementary Materials Table S1**. Notably, these features can be categorized into two groups: elemental descriptors, indicating alloy properties as an extension of the elements in the composition (S.N. 1-11), and alloying descriptors, highlighting property changes resulting from element interactions in alloy formation (S.N. 12-15). The entropy of mixing was evaluated using the *WenAlloys* class from the *matminer* library [30], while the enthalpy of mixing was derived from Miedema's model. Importantly, the feature pool intentionally excludes the feature corresponding to the manufacturing route or fabrication procedure (MR), signifying its exclusion in correlation analysis and principal component analysis, with selective utilization in the ensemble machine learning algorithm.

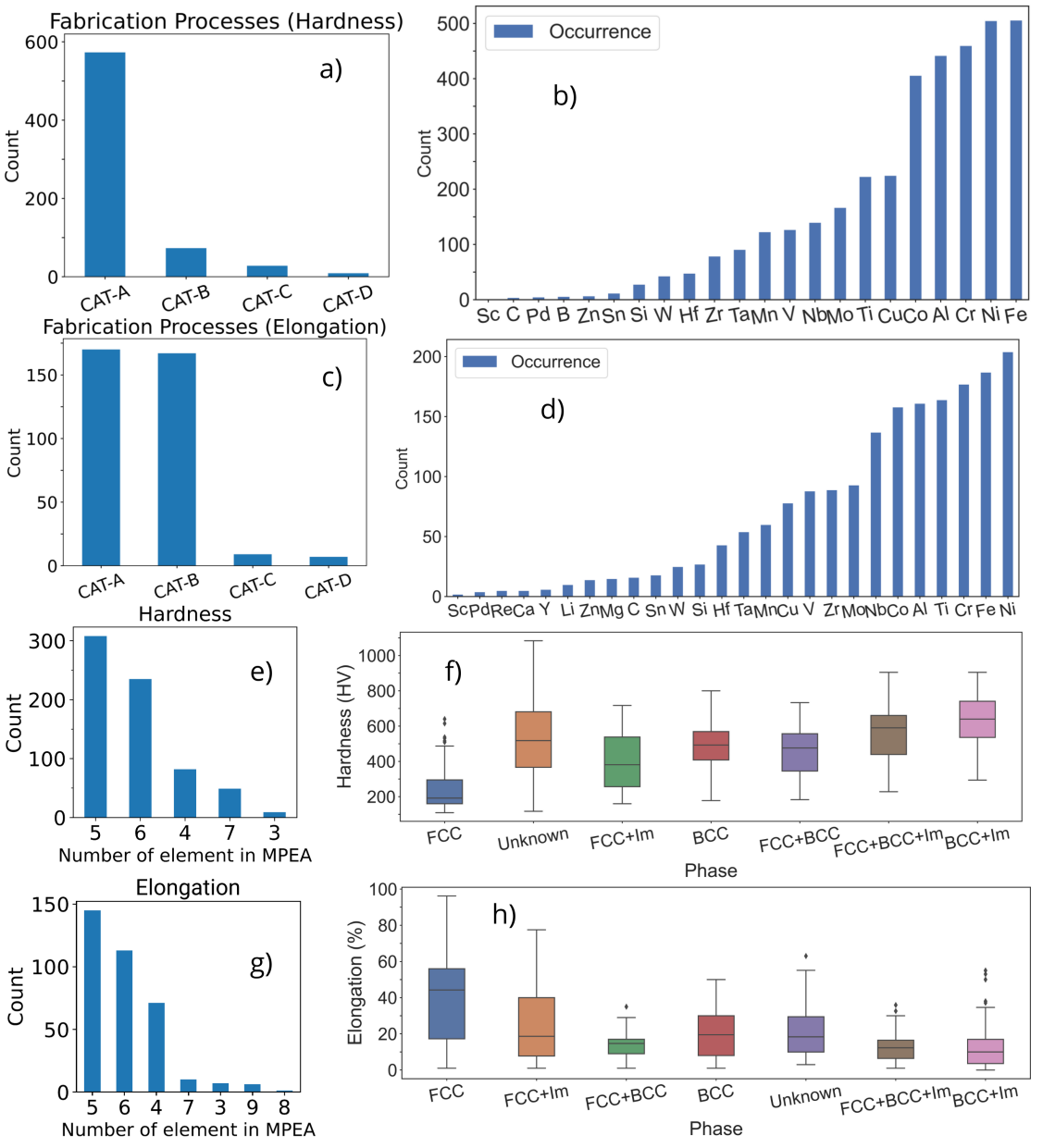

Figure 3: Understanding the data through visualization is a prelude to featurization. Number of MPEA for different fabrication routes for **a)** Hardness **c)** elongation. Number of occurrence of elements in **b)** hardness **d)** elongation. Number of elements in an alloy system for **e)** hardness **g)** elongation. Statistical distribution for seven phase systems with mean, median, and quartiles (25% and 75%) for **f)** hardness **h)** elongation

2.2. Data Preprocessing and Feature Engineering

The collected datasets were divided into training and testing sets to prevent data leakage during preprocessing and model training. This split ensures that the test data can provide an accurate representation of the model's performance on new MPEAs. The random split was conducted with a 90:10 ratio for training and testing data. The distribution of hardness and elongation values in the training and testing datasets is visualized in Figure 4 (a). Figure 4 (a) i) displays the distribution of 614 training hardness data points, with a mean of 500 HV, a median of 506 HV, and 10th and 90th percentiles at 207 HV and 782 HV, respectively. In Figure 4 (a) ii), the distribution of 69 test hardness data points closely resembles the diversity seen in the training data, with percentiles ranging from 218 HV to 715 HV and a mean

Table 1
The table's first column lists the initial 15 input features considered for the feature pool, applicable to both the hardness and elongation datasets. In the hardness dataset, the output feature of interest is hardness (HV), while in the elongation dataset, it is elongation (EL). To assess multicollinearity within the feature pool, variance inflation factor (VIF) analysis is conducted. It's worth noting that PCC stands for Pearson's correlation coefficient, and a comprehensive examination of PCC will be provided in Section 2.2.

Name of Features	Hardness VIF		Elongation VIF	
	Before PCC	After PCC	Before PCC	After PCC
Mean Atomic Radius difference (δ)	8.3	6.43	5.02	2.2
Electronegativity asymmetry ($\Delta\chi$)	3.98	1.66	3.37	Dropped
Average Melting Temperature ($T_m(K)$)	63.1	Dropped	60.48	Dropped
Melting Temperature asymmetry (ΔT_m)	4.16	3.19	2.97	2.0
Valence Electron Concentration (VEC)	21.48	2.35	11.1	3.0
Average Atomic Number (AN)	18.55	Dropped	14.46	Dropped
Thermal Conductivity (K)	5.55	Dropped	7.40	Dropped
Average Bulk Modulus (B)	16.55	Dropped	31.21	Dropped
Bulk Modulus Asymmetry (ΔB)	7.5	2.88	6.35	3.32
Average Shear Modulus (G)	3.32	Dropped	7.47	Dropped
Shear Modulus Asymmetry (ΔG)	3.9	1.8	3.25	1.26
Entropy of Mixing asymmetry (ΔS_{mix})	1.22	Dropped	1.65	1.32
Enthalpy of Mixing asymmetry (ΔH_{mix})	4.8	3.07	2.99	1.57
Geometrical Parameter (λ)	2.2	1.99	2.08	Dropped
Dimensionless parameter (Ω)	1.17	Dropped	1.17	Dropped

of 458 HV. Similarly, Figure 4 (a) iv) represents the distribution of 36 test elongation observations, capturing the variation observed in the training data shown in Figure 4 (a) iii). The mean elongation values for the training and test sets are 22% and 25%, respectively.

Following the split, the training set is standardized using Sci-Kit Learn's *StandardScalar()* library to achieve a mean of zero and a standard deviation of one, a common practice in machine learning to mitigate the impact of feature magnitude variations. The test data is also standardized using the statistics from the training set. However, it's worth noting that the four features corresponding to fabrication routes (CAT-A, CAT-B, CAT-C, and CAT-D) are not standardized. These categorical inputs are one-hot encoded into columns of zeros and ones, representing the presence or absence of each route for a given MPEA. For example, if an MPEA is manufactured via the casting process (CAT-A), its corresponding column would have a value of 1, while the other columns (CAT-B, CAT-C, CAT-D) would have 0 values, resulting in a clear representation of the fabrication route (MR) for that MPEA.

In the course of machine learning model construction, feature selection is defined as a technique of identifying the subset from a given set of initial features, which can eventually help in realizing the simplification of the future model and solve problem such as the curse of dimensionality. In other words, feature selection is an important task to perform for the identification and elimination of redundant input features. The regression type model which gives a numerical target as output needs a numerical feature selection technique. Two of the most commonly used approaches for the numerical feature selection for regression models are Correlation metrics and Principal component analysis (PCA).

2.2.1. Variable reduction with PCC heatmaps and multicollinearity analysis

Pearson's correlation coefficient (PCC) assesses linear relationships among variables, vital for classification or regression tasks [59, 60]. PCC heatmaps in **Supplementary Figure S1 and S2** show correlations between 15 input variables and target hardness (HV) and elongation (EL). The coefficients range from -1 to 1, with higher absolute PCC values indicating stronger correlations. Features with PCC above 0.9 are reduced to one, and those below 0.2 with the target variable are excluded, ensuring relevant input features for model development. Eight features (δ, $\Delta\chi$, ΔT_m, VEC, ΔB, ΔG, λ, ΔH_{mix}) were selected alongside the target HV feature for ML model development. And, In the case of elongation seven input features (δ, ΔT_m, VEC, ΔB, ΔG, ΔS_{mix}, ΔH_{mix}) emerged as finalists, following similar PCC criteria. The PCC heatmap in Fig. 4 (b) reveals that each of these input features has a PCC score of absolute magnitude larger than 0.2 with target , i.e., HV or EL, and less than 0.9 with other input features. This refined dataset, named DB1-HV-PCC, comprises these eight features and HV. The corresponding refined dataset for elongation elongation

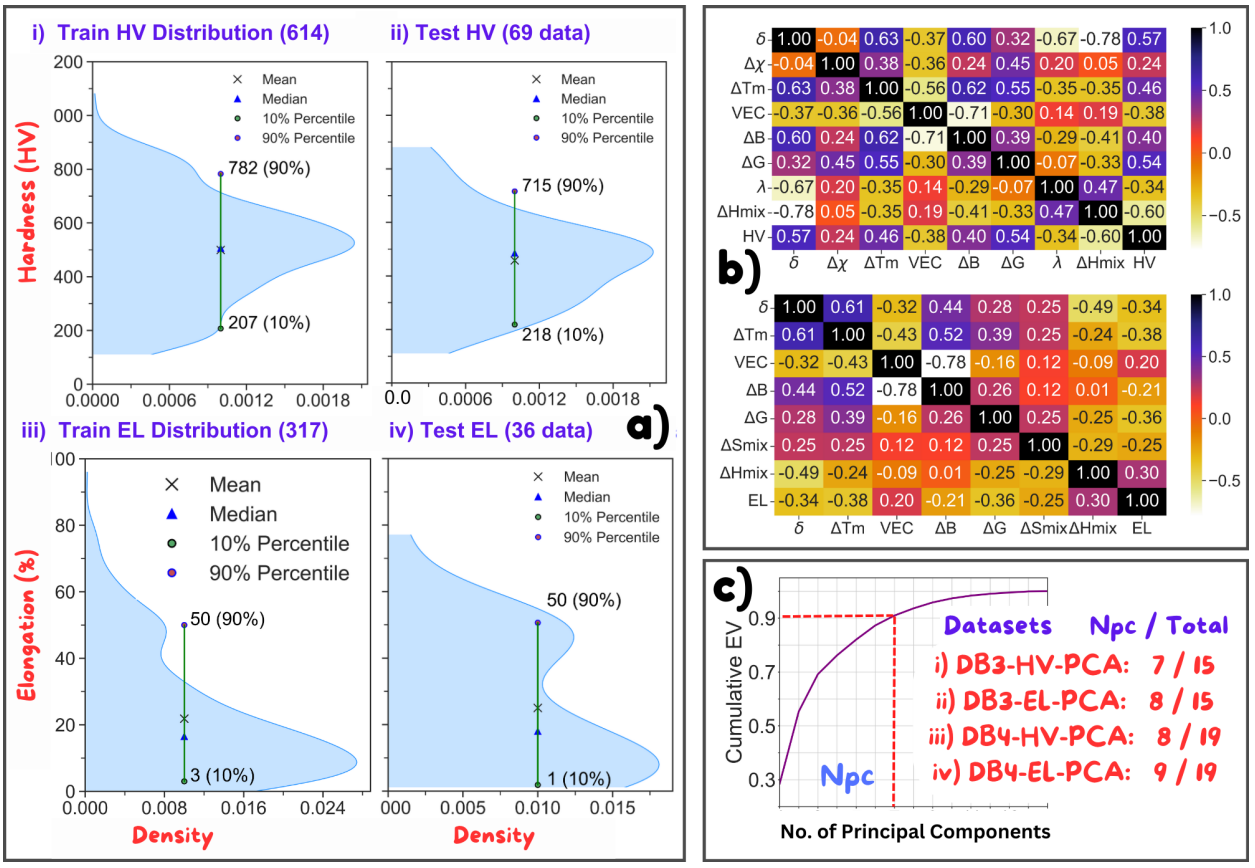

Figure 4: Data preprocessing and analysis. a) Distribution of Train-Test split. hardness has 614 train and 69 test data while elongation has 317 train and 36 test datasets. The plot shows test and train distribution follows similar distribution) **b) Heatmap** after feature selection by PCC correspondings to the features of the refined hardness database DB1-HV-PCC and the elongation database DB1-EL-PCC. The inclusion of ΔB (denominator in Pugh's ratio), ΔG (numerator in Pugh's ratio) and VEC in the feature pool verifies that the information associated with relevant indicators of hardness and ductility is well preserved within the training datasets. **c) Cumulative Explained Variances (EVs) for PCA.** This figure illustrates the feature sets' ability to capture 90% of the explained variance. DB3-HV-PCA achieves this with 7 out of 15 components, DB3-EL-PCA with 8 out of 15 components, DB4-HV-PCA with 8 out of 19 features, and DB4-EL-PCA with 9 out of the same 19 features, as determined by PCA. Additional details are available in **Supplementary Material S1 and Figure S3**

is labeled DB1-EL-PCC. To account for the influence of manufacturing routes on mechanical properties, the MR feature was manually added to the DB1-HV-PCC and DB1-EL-PCC datasets, forming DB2-HV-PCC (for hardness) and DB2-EL-PCC (for elongation). These databases are detailed in Table 2.

The assessment of input feature relevance in our analysis is complemented by the Variance Inflation Factor (VIF), a metric used to detect multicollinearity. VIF quantifies the correlation strength between independent features by regressing one feature against all others. Mathematically, for the i^{th} predictor feature, VIF_i is calculated as

$$\mathrm{VIF}_i = \frac{1}{1 - R_i^2} \tag{1}$$

Where R_i^2 represents the R^2 value obtained by regressing the i^{th} predictor feature with the remaining predictors in the dataset. VIF typically ranges from 1 to infinity, with values exceeding 4.00 warranting attention and values surpassing 10.00 indicating severe multicollinearity, suggesting that a feature is redundant and can be expressed as a linear combination of others [61]. In our analysis, this criterion was applied to both the hardness and elongation datasets before and after PCC analysis, as shown in Table 1. Among the 15 hardness data attributes, the average

melting temperature (T_m(K)) exhibited the highest VIF of 63.1, signifying strong correlation with other variables. Given its PCC score of 0.00 with HV, T_m(K) was excluded as a less relevant and highly redundant feature. Similarly, AN (VIF = 18.55, PCC score = -0.11 with HV) and B (VIF = 16.55, PCC score = -0.11 with the output attribute) were removed from the feature pool. Conversely, despite multicollinearity (VIF = 21.48), VEC was retained due to its strong negative correlation (PCC score = -0.38) with HV. Features δ (VIF = 8.3) and ΔH_{mix} (VIF = 4.8) exceeded the VIF threshold of 4.0, but their high correlations with HV (PCC scores of 0.57 and -0.60, respectively) justified their inclusion. λ displayed a PCC score of -0.34 with HV and a VIF of 2.2, meeting the criteria for inclusion based on minimum redundancy and maximum relevance. However, ΔS_{mix} (VIF = 1.22) and Ω (VIF = 1.17) were dropped due to weak correlations with the output attribute. After removing seven input features, multicollinearity analysis yielded VIF values well below 10.00. VEC, originally problematic with a VIF of 21.48, now had an updated VIF of 2.35, resolving the multicollinearity issue. In the final list of eight selected features, only δ (VIF = 6.43) exceeded the warning limit of 4.00, but its high correlation with the HV feature (PCC score = 0.57) underscored its relevance and utility in the model.

The combined use of Pearson's correlation coefficient (PCC) and Variance Inflation Factor (VIF) scores guided feature selection for the elongation dataset. Features like T_m(K), AN, and B, which displayed poor correlations with elongation (EL) and significant multicollinearity issues with other input features (PCC scores of -0.08, -0.04, and 0.00 with EL, and VIF values of 60.48, 14.46, and 31.21, respectively), were removed from the feature pool. Features Ω (VIF = 1.17) and λ (VIF = 2.08), despite lacking multicollinearity issues, were also eliminated due to their weak correlations with EL. This led to the exclusion of 8 features ($\Delta\chi$, $T_m(K)$, AN, K, B, λ, and Ω) from the elongation dataset. The remaining 7 features, each exhibiting an absolute PCC score with EL equal to or greater than 0.2, were subjected to multicollinearity analysis, resulting in VIFs below 4.0 for all selected features (Table 1). Importantly, these analyses underscored the limited relevance of average values of physical quantities in multi-principal element alloys (MPEAs), with most averaged quantities, initially included in the feature pool, being eliminated. Instead, the asymmetry factor in the magnitudes of physical properties of constituent elements within MPEAs emerged as a significant determinant of the output features (HV or EL). Asymmetry features related to melting temperature, bulk modulus, shear modulus, and enthalpy of mixing, along with the Mean Atomic Size Difference, were included in both the hardness and elongation datasets, highlighting their role in data-driven alloy property design (Fig. 4(b)).

It is noteworthy to mention that the reduced pool of selected features from the PCC correlation method must include the attributes considered as the significant indicators of hardness and ductility metrics from the viewpoint of physics. Pugh's ratio [41], defined as the ratio of shear modulus and bulk modulus, is known to be a de-facto indicator of hardness [46, 62] and ductility [40, 42, 46] for several classes of materials. Besides, Pugh's ratio; Cauchy pressure is also regarded a significant indicator for the elongation and hardness properties. In other words, Pugh's criterion [41] and Pettifor criterion [43, 44] are the two classical criteria to estimate whether a material is ductile or brittle [63]. By establishing the relationship between Pugh's ratio and Cauchy pressure, Senkov and Miracle [63] have revealed that the two criteria are identical for cubic phase materials and alloys. It can be thus inferred that using either Pugh's criterion or Pettifor criterion would be sufficient in the study of hardness and ductility of materials. Moreover, microhardness values and percentage elongation for the FCC and BCC multi-principal element alloys are influenced by their VECs [40, 64, 65, 66]. Owing to the presence of hard elements at VEC range 5-7, BCC-phase MPEAs with VECs in the range 4-5.5 are known to exhibit the increment of hardness with increase in VEC [67]. Balasubramanian et al. [46] have described VEC as a unified indicator for several mechanical properties including hardness and ductility. Presenting for rock-salt structure binary and ternary metal carbides, nitrides and carbonitrides; they have reported that the ductility in general increases with VEC whereas hardness first increasdes with increase in VEC but later on decreases at VEC = 9.5 and beyond. Since these relationship is established in materials defined with rock-salt structure using first principles calculations, it would be important to associate hardness and ductility with VEC for MPEAs. In Fig. 4(b), the features ΔB and ΔG are associated with Pugh's ratio, and the list also includes VEC. Hence, the training data for machine learning will include the features that are considered as the significant indicators of ductility and hardness.

2.2.2. PCA for feature selection in the datasets

Principal component analysis (PCA) is a valuable statistical technique used to condense extensive feature sets, facilitating data visualization and analysis [68]. It accomplishes dimensionality reduction by breaking down a data matrix into two components: direction and magnitude, yielding multiple data directions. These directions are used to transform the original data, aligning it with possible directions. By identifying essential directions significant for regression analysis, less crucial components can be removed.

In this study, two sets of hardness and elongation data were considered, one excluding manufacturing route features, and the other including them. Each dataset, denoted as D_i (D_H for hardness and D_E for elongation), is a k × N matrix, where k is the dimension of the dataset (15 for datasets without manufacturing route features, and 19 for those including route features), and N is the number of observations. PCA aims to project these k-dimensional datasets into a lower-dimensional p-dimensional subspace (where p < k) to enhance computational efficiency while preserving over 90PCA involves eigendecomposition of the covariance matrix (A_i) to extract meaningful insights from the dataset D_i. This process yields eigenvectors [[ν_1], [ν_2], ...,[ν_k]] and their corresponding eigenvalues [ψ_1, ψ_2, ..., ψ_k]. Each eigenvector defines a direction in the new feature space, with associated eigenvalues indicating their importance. Explained variance (EV) quantifies the variance explained by each principal component, reflecting its relative significance within the feature space. EV is calculated as the ratio of eigenvalue ψ_j to the sum of all k eigenvalues for the j^{th} principal component [ν_j]. The orthogonal nature of the eigenvectors ensures uncorrelated principal components. Details on eigendecomposition and PCA procedures, including manufacturing route information, are provided in **Supplementary Materials Section S1.3** for the hardness dataset, with similar methods applied to other datasets.

$$EV = \frac{\psi_j}{\sum_{i=1}^{k} \psi_i} \tag{2}$$

From Eq. 2, it becomes evident that eigenvalues serve as indicators of the variances within the dataset along the new feature axes generated by PCA. To establish a feature subspace consisting of p principal components (PCs), a cumulative explained variance (cumulative EV) greater than 90% (0.9 in fractional value) is the chosen criterion for information retention. This criterion determines the reduced number of principal components that will exclusively represent the post-PCA dataset in the new feature space. The cumulative explained variances (EVs) for the datasets are visually presented in Figure 4 c). For DB3-HV-PCA, it is observed that 7 out of the initial 15 components are capable of capturing 90% of the explained variance. Similarly, in the case of DB3-EL-PCA, 8 out of the original 15 components demonstrate the ability to account for 90% of the explained variance. Conversely, for DB4-HV-PCA, 8 out of the expanded set of 19 features exhibit the capability to capture this 90% explained variance, and in the context of DB4-EL-PCA, 9 out of the same 19 features achieve this 90% explained variance through Pearson's correlation coefficient analysis. The inverse transformation matrices of these selected principal components along with their corresponding output feature (in original feature space) are arranged in databases, and the names of the databases are also listed in Table 2.

2.3. AlloyManufacturingNet - trained to learn the hardness and elongation dataset

After completing data preprocessing and feature selection, the machine learning model training phase commences. Specifically, regression machine learning models are employed for predicting the hardness and elongation of MPEAs. Regression analysis, a form of supervised learning, establishes relationships between input features and target variables. In contrast to classification analysis, which yields discrete or categorical outputs, regression produces continuous functions or numerical target values [69]. Artificial Neural Networks (ANNs) are used in this study for regression analysis, as they can capture complex and non-linear relationships between inputs and targets through the application of non-linear activation functions in each layer. These ANNs, trained with datasets containing information about the manufacturing routes of MPEAs, are denoted as AlloyManufacturingNet.

Table 2 presents four distinct sets of models for hardness data (DB1-HV-PCC, DB2-HV-PCC, DB3-HV-PCA, and DB4-HV-PCA) and four different models/databases for elongation data (DB1-EL-PCC, DB2-EL-PCC, DB3-EL-PCA, and DB4-EL-PCA). For instance, DB2-HV-PCC incorporates additional information about the manufacturing process's influence on hardness, while DB1-HV-PCC lacks this information but comprises fewer input features. This reduced feature set in DB1-HV-PCC helps mitigate the curse of dimensionality compared to DB2-HV-PCC. It allows for a more pronounced measurement of the effect of changes in electronegativity difference on hardness, as it is less influenced by other input features. On the other hand, the selected input features from PCA analysis in DB3-HV-PCA and DB4-HV-PCA are uncorrelated with each other, enhancing the prediction potential of machine learning models. Similarly, the diversity among the four databases for elongation data follows a similar pattern. The key question now is how to ensure that the unique informational and functional advantages offered by each database are proportionately integrated into the machine learning model(s). The answer lies in constructing ensemble neural network models.

Table 2
AlloyManufacturingNet as an ensemble of neural networks, will be built upon the different database types as outlined here. In context of feature selection using PCC, the input and output variables are in the same feature space of the data matrix. However, for the databases associated with PCA, the output feature (hardness or elongation) will be in a different feature space than those of the selected principal components. So, the inverse transformation of the principal component feature space to the original feature space will be performed to map input features with the output variable.

Databases/Models ID	Characteristics/Descriptions
DB1-HV-PCC	8 input features + hardness feature (HV) as exactly selected from PCC
DB2-HV-PCC	Features of DB1-HV-PCC + manufacturing route (MR) input features
DB3-HV-PCA	7 Principal Components of Hardness data w/o MR based features + HV feature
DB4-HV-PCA	8 Principal Components of Hardness data including MR based features + HV feature
DB1-EL-PCC	7 input features + elongation (EL) feature as selected via PCC
DB2-EL-PCC	Features of DB1-EL-PCC + MR features
DB3-EL-PCA	8 Principal Components of Elongation data w/o MR based features + EL feature
DB4-EL-PCA	9 Principal Components of Elongation data including MR based features + EL feature

In machine learning, an ensemble model combines multiple sets of models to improve overall predictive accuracy [70]. An ensemble neural network (NN) model is a committee of distinct models, where each model contributes to the final prediction. For mechanical property data, such as hardness, four unique databases are created after feature selection (see Table 2). The ensemble NN models built on these datasets combine the predictions of individual models through weighted averaging to maximize R^2. The weighted-average prediction represents the ensemble model's final output. Similarly, for elongation data, the ensemble learning is based on four distinct databases listed in Table 2.

For the design of the ensemble neural network of a given mechanical property (hardness/elongation), first of all the individual models (model no. 1-4) of Table 3 are trained. For a given model number, the selected features are supplied at th input and the model is trained with the most suitable hyper-parameters. 10% of the training data is used as a validation dataset. *Tensorflow 2.7* software with *keras* frontend is used for compiling and running the neural network model. The result of the machine learning was visualized with the help of *matplotlib* library. It is desirable that the individual/ensemble neural networks can perform well beyond the training data and metrics such as *mae, rmse* have been employed in this study to quantitatively ensure the cross-validation tasks.

Hyperparameters, like epochs, batch size, layer dimensions, optimization functions, activation functions, and more, exert significant control over the model's learning process. Weight initialization and constraints also influence initial weight values. Regularization and dropout rates are introduced to prevent overfitting during training. Hyperparameter tuning aims to find the optimal combination of these parameters to maximize scoring metrics, such as R^2. *RandomSearchCV* from the SK-learn library was employed for hyperparameter tuning, randomly selecting 300 configurations from a grid detailed in Supplementary Materials, Table S2. These configurations were evaluated using 10-fold cross-validation, resulting in a total of 3,000 model tests. The ensemble model's configuration was determined based on the highest average R^2 value from cross-validation. Additional evaluation metrics, including RMSE, MAE, and MSE (see Table 3), were considered to ensure performance consistency and generalization. These metrics bolster the model's robustness and validate the weighting methodology, aligning with the core objectives of ensemble modeling. Detailed hyperparameter values are provided in **Supplementary Materials, Tables S2 and S3**.

The test dataset undergoes standardization to align with the training data standardization, preventing data leakage and ensuring realistic test results. During model training, *Callbacks* are employed to track validation RMSE, helping identify the model with the best validation RMSE. This optimal model is then used as a component in the ensemble of four models, as shown in Table 2, for both hardness and elongation. Given that individual models' predictions differ, a simple average might not yield the best ensemble outcomes. To optimize model significance, the best-weighted

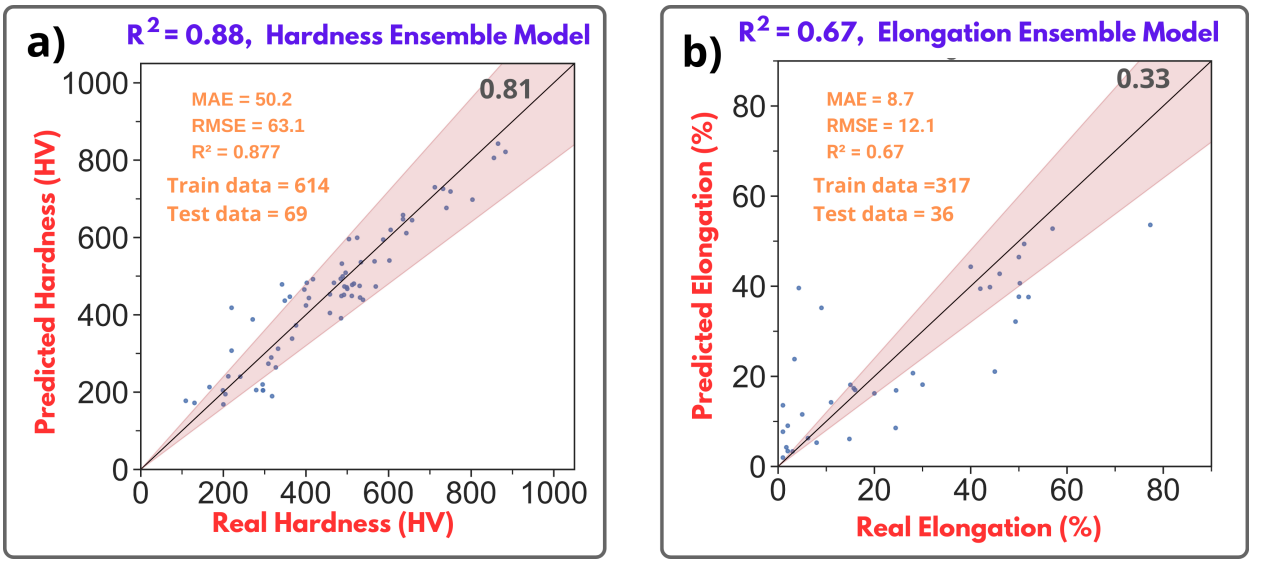

Figure 5: Parity plot for test datasets. Parity plots along with the Mean Absolute Error (MAE), Root Mean Squared Error (RMSE), and coefficient of determinant (R^2) for **a)** hardness (614 alloys from training data and 69 from test data alloys) **b)** elongation (317 alloys from training data and 36 from test data). The dataset of elongation shown in the b) corresponds to the mixture set of tensile and compression test specimens. The shaded region represents an 80 % accuracy region with a number at the top right edge indicating the fraction of test predictions having $>$ 80 % accuracy.

fractions are determined. By employing the entire dataset used to build the model (combining both train and test data), weighted averages of predictions from individual models within the ensemble are computed to obtain the final model predictions. Results for each individual model and the ensemble models are detailed in Table 3. Further elaboration on cross-validation results will be provided in Sec. 3.1.

3. Results and Discussions

3.1. Cross-validation results for ANN models and ensemble model design optimization

Moving forward, we focus on developing deterministic neural network prediction models. These ensemble neural network models, as discussed in Sec. 2.3, combine the strengths of four deterministic models to ensure balanced information integration. Consequently, these ensemble models will serve as our prediction models for mechanical properties.

Before adopting the ensemble neural network as the prediction model, thorough validation on an independent test dataset is essential. The results for the ensemble models on the test dataset are concisely summarized in parity plots in Fig. 5, accompanied by key performance metrics. For hardness analysis (refer Fig. 5a)) , the ensemble model boasts an MAE of 50.2 HV, RMSE of 63.1 HV, and an impressive R^2 of 0.877. Notably, 81% of the test data falls within the 80% accuracy region. In the case of elongation analysis presented in Fig. 5b) for training datasets consisting of mixture set of both compression and tensile test specimens, the ensemble model exhibits MAE = 8.7% , RMSE= 12.1% RMSE, and $R^2 = 0.67$, with 33% of the test data residing within the 80% accuracy region.

The optimization criterion for determining weighted fractions of predictions from individual member neural network models is the maximum R^2 value. In the hardness ensemble model, models 1-4 (Table 3) are assigned weighted fractions of 0.3, 0.3, 0.1, and 0.3, respectively, yielding the highest R^2. This same order of weighted fractions is applied in designing the ensemble models. Notably, the influence of DB2-HV-PCC (weighted fraction = 0.3) and DB4-EL-PCA (weighted fraction = 0.3), which include variables related to the fabrication route, is substantial, underscoring the manufacturing route's significant role in shaping the hardness feature.

For elongation analysis, models corresponding to databases DB1-EL-PCC, DB2-EL-PCC, DB3-EL-PCA, and DB4-EL-PCA receive respective weight fractions of 0.3, 0.3, 0.2, and 0.3. Once again, the model derived from DB3-EL-PCA carries less weight compared to the other three models, highlighting the importance of including the manufacturing route in elongation prediction. This optimization procedure also confirms that PCC-based feature

Table 3
Metrics and weight factors of the individual models for hardness and elongation analyses are presented in the first four rows. The final row provides the metrics associated with the Ensemble NN. For the column of feature selection, the technique or method remarked with an asterisk (PCC* or PCA*) means that the final databases include the features corresponding to fabrication routes. Those rows with PCC and PCA not marked with asterisk imply that the databases exclude the features associated with the manufacturing route.

Model numbering	Feature Selection	Hardness Models	Elongation Models
1	PCC	Database = DB1-HV-PCC MAE = 58.6 RMSE = 75.9 R^2 = 0.822 ideal weights = 0.3	Database = DB1-EL-PCC MAE = 7.9 RMSE = 12 R^2 = 0.67 ideal weights = 0.3
2	PCC*	Database = DB2-HV-PCC MAE = 51.9 RMSE = 71.7 R^2 = 0.841 ideal weights = 0.3	Database = DB2-EL-PCC MAE = 8.33 RMSE = 12.34 R^2 = 0.65 ideal weights = 0.3
3	PCA	Database = DB3-HV-PCA MAE = 57.7 RMSE = 75.5 R^2 = 0.824 ideal weights = 0.1	Database = DB3-EL-PCA MAE = 11.8 RMSE = 15.55 R^2 = 0.45 ideal weights = 0.2
4	PCA*	Database = DB4-HV-PCA MAE = 54.8 RMSE = 70 R^2 = 0.848 ideal weights = 0.3	Database = DB4-EL-PCA MAE = 12.26 RMSE = 16.27 R^2 = 0.4 ideal weights = 0.3
Ensemble model		MAE = 50.2 RMSE = 63.1 R^2 = 0.877	MAE = 9.7 RMSE = 12.1 R^2 = 0.67

selection holds greater weight than PCA-based feature selection. In the hardness ensemble machine learning model, the two PCC-based models each receive a weight fraction of 0.3, while the two PCA-based models receive corresponding weight fractions of 0.1 and 0.3. Similarly, in the elongation ensemble neural network, the two PCC-based models are assigned identical weight fractions of 0.3, while the two PCA-based models receive weight fractions of 0.2 and 0.3, respectively.

3.2. AlloyManufacturingNet as prediction model in hardness-ductility synergy design

The successful completion of cross-validation and ensemble model optimization now paves the way for the practical application of these neural network models in predicting mechanical properties for new multi-principal element alloys. To put our models to the test, we predicted the properties of an alloy, $Al_{0.5}Nb_{0.5}TiV_2Zr_{0.5}$, which was absent from the training and test datasets of the individual models. The results are summarized in Table 4. Notably, the experimental hardness value for this alloy is 577.7 HV [57], and our ensemble model predicts it with exceptional accuracy, yielding a prediction error of just 1.63%. This underscores the model's intelligence and its ability to provide reliable predictions for previously unencountered alloys. Moreover, the model effectively captures the broader trend that alloys with a higher proportion of Nb and Zr tend to exhibit higher hardness values, as evident in the prediction for $Al_{0.5}NbTiV_2Zr$, aligning closely with its experimental hardness of 614.1 HV [57]. Table 4 also presents a comparison between the experimental and predicted elongation values for the $Al_{0.5}Nb_{0.5}TiV_2Zr_{0.5}$ alloy. The experimental elongation stands at 12.72% [57], while the model predicts it to be 14.1% with an error of less than 10%. This indicates the model's ability to provide reasonably accurate predictions for elongation properties, further emphasizing its utility and reliability in predicting mechanical properties for a wide array of alloys, including those not covered in the training dataset.

In the era of artificial intelligence, the integration of machine learning into materials science has ushered in the era of inverse alloy design [71]. Simultaneously, it has advanced the accelerated design and discovery of new materials

Table 4
Evaluation of trained ensemble models by predicting hardness and elongation for $Al_{0.5}Nb_{0.5}TiV_2Zr_{0.5}$ alloy previously unknown to the model. The values for the experimental hardness and elongation of this MPEA are obtained from Jiang et al. [57].

Hardness (HV)		Elongation (EL)	
Predicted HV	587.16	Predicted EL (%)	12.72
Experimental HV	577.7	Experimental EL (%)	14.1
% Error	1.63	% Error	9.8
MAE	9.46	MAE	1.38

[72], which exhibit a diverse range of mechanical properties. In practical terms, the prediction model developed through the training and validation procedures serves as a versatile virtual tool for materials design and discovery. In this study, the prediction models encompassing hardness and elongation ensemble neural networks act as crucial tools for forecasting the properties of various multi-principal element alloy (MPEA) compositions. Given that neural networks can approximate a wide range of functions, they are also capable of aiding in the reverse engineering of compositions that meet specific hardness and/or elongation criteria. Notably, these data-driven techniques can be employed to optimize MPEA compositions while adhering to the constraints defined by the hardness-ductility synergy criterion.

We employ ensemble neural networks, denoted as AlloyManufacturingNet, to facilitate the prediction-driven inverse design of two multi-principal element alloys (MPEAs). Our focus centers on two medium entropy alloys (MEAs), specifically ZrHfNb and VNbTa, as our foundational materials. Our objective revolves around gauging the impact of introducing two refractory elements simultaneously as dopants on their hardness and elongation properties. Furthermore, we delve into evaluating the significance of different manufacturing routes in the context of these doped MEAs. To provide context, it's worth noting that the reference hardness values for ZrHfNb and VNbTa stand at 365.9 HV and 403.82 HV, respectively, while their corresponding elongation values are 31.37% for ZrHfNb and 20.96% for VNbTa. In our approach, we introduce two dopant elements, D1 and D2, drawn from the list [Cr, W, Mo, Ta, and Ti], into ZrHfNb for a given fabrication route. These dopants are incorporated in varying proportions, enabling our prediction model to estimate the hardness and elongation characteristics of $D1_xD2_y(ZrHfNb)_{1-x-y}$ at diverse composition proportions represented by x and y. Similarly, for different variants of manufacturing routes, we select a pair of dopant elements (D1, D2) from the list [Zr, W, Hf, Mo, Ti, and Cr] to introduce into the base VNbTa MEA. Our ensemble neural networks then predict the properties of $D1_xD2_y(VNbTa)_{1-x-y}$ MPEAs. This data-driven approach primarily focuses on the design of quinary MPEAs, offering a cost-effective and time-efficient alternative to traditional alloy design processes.

In contrast to conventional experimental methodologies that necessitate numerous trials to fabricate and test alloys with varying dopant levels, our machine learning models adeptly manage the complexity of simultaneously introducing two dopants without incurring substantial additional cost and time. Capitalizing on this advantage, our study explores the effects of different manufacturing routes when including two dopants in base MEAs simultaneously. We also ascertain the compositions of dopants that yield maximum hardness and elongation values under a given manufacturing method. Furthermore, we predict the specific compositions that achieve optimal hardness-elongation values, filtering out alloys with extreme values for one property but not the other. From this pool of candidates, including several others, we discern the best candidate through the formulation of an optimization problem. If $(HV)_{x,y}$ and $(EL)_{x,y}$ are the predicted values of the hardness feature and elongation feature resulted in a given fabrication procedure for the composition proportion x and y of dopants D1 and D2 respectively.

Hardness and elongation, vital material properties measured in different units, pose a challenge due to their disparate measurement scales rooted in distinct physics and theoretical concepts. To align these properties, a statistical approach is employed. Both hardness and elongation undergo standardization based on mean and standard deviation, a process rendering them dimensionless. This standardization facilitates composition optimization by enabling the direct

comparison of these scale-invariant properties. This method results in the definition of the following objective function defined as:

$$F(x,y) = \frac{(HV)_{x,y} - \overline{HV}}{\sigma_{HV}} + \frac{(EL)_{x,y} - \overline{EL}}{\sigma_{EL}} \tag{3}$$

The objective function $F(x, y)$ in Eq. 3 is maximized after subjected to the constraints: $x \geq 0$, $y \geq 0$, $782HV \geq (HV)_{x,y} \geq 207HV$ and $60\% \geq (EL)_{x,y} \geq 5\%$. $\overline{HV} = 495.3$ HV and $\sigma_{HV} = 196.75$ HV are the respective mean and standard deviation values of the originally collected hardness feature. Similarly, $\overline{EL} = 22.16$ % and $\sigma_{EL} = 19$ % are respectively the mean and standard deviation of the elongation variable. While the sample hardness and elongation features are specified for a given manufacturing route, it's worth noting that the statistical mean and standard deviation values, as defined previously, remain unaffected by changes in the fabrication procedure. With the hardness feature ranging from 207 HV to 782 HV and elongation falling between 5% and 60% (as shown in Figure 3), it becomes evident that the combined non-standardized values of HV and EL are predominantly influenced by the HV feature due to its larger range. To mitigate the bias introduced by variables with differing scales during mathematical calculations and to prevent errors, we employ a standardization procedure in this optimization task. By utilizing standardized features in the objective function, the inherent differences in scale between the hardness and elongation variables cease to impact the mathematical determination of the optimal alloy composition. This ensures scale-invariant composition optimization when dealing with two predicted unique variables of dissimilar ranges or scales.

It's important to emphasize that the standardized objective function in Equation (3) can yield positive, negative, or zero values. If a predicted hardness variable falls below the mean value, the numerator of the first term in the right-hand side of Equation (3) is negative, resulting in a standardized hardness feature below zero. Conversely, when the estimated value exceeds the mean hardness, the standardized hardness takes on a positive value. Similarly, depending on the magnitude of the predicted elongation feature, the standardized elongation feature (the second term on the right-hand side of the equation) can be either greater or less than zero. From an optimization perspective, a more positive function value indicates the suitability of the multi-principal element alloy (MPEA) for structural and materials applications. Specifically, an MPEA designed with both standardized variables (hardness and elongation) represented as positive real numbers is considered favorable in materials design. Conversely, an MPEA with either one or both standardized features as negative real numbers is deemed unsuitable for structural material applications. Therefore, the necessary and sufficient condition for a multi-principal element alloy to be deemed appropriate for technological applications is that it must exhibit positive values for standardized hardness and standardized elongation while maximizing the positive real number value of the standardized objective function.

The relationship between the composition of the first generic $D1_xD2_y(ZrHfNb)_{1-x-y}$, manufacturing routes, and the specified hardness features at room temperature is visually depicted in the ternary plots of Figure 4. Corresponding information regarding elongation for these alloy systems is provided in Figure 5. Additionally, presentations detailing hardness and elongation for the second generic $D1_xD2_y(VNbTa)_{1-x-y}$ are presented in Figures 6 and 7, respectively. These ternary plots serve as the cornerstone of inverse alloy design. The significant coordinate points (x, y) representing dopant composition proportions in the ternary plots, along with the specific manufacturing route associated with the maximum hardness value (independently established from the hardness plots) and the maximum elongation value (solely derived from the elongation plots), are listed in Table **Supplementary Table S4** for the first generic alloy system and **Table S5** for the second generic MPEA system. The manufacturing route corresponding to the assigned property value is also presented.

3.2.1. Predictive design of maximum hardness and maximum elongations for undiscovered MPEA

In the context of alloy systems $D1_xD2y(ZrHfNb)1-x-y$ and $D1_xD2y(VNbTa)1-x-y$, we present graphical representations of alloy compositions and the corresponding hardness and/or elongation properties at room temperature for different manufacturing routes in ternary plots (**Supplementary Figure S10, S11, S12, S13**). These ternary plots play a pivotal role in inverse alloy design.

For the $Cr_xWy(ZrHfNb)_{1-x-y}$ system, doping ZrHfNb with Cr and W elements leads to significantly elevated hardness values across all four manufacturing routes. Notably, the [W, Ta] dopant pair, followed by [Mo, Ta], imparts intermediate hardness to the base ZrHfNb system, while the [Ti, Ta] dopant pair results in lower hardness values. Analysis of ternary plots for dopants pair yielding maximum hardness and maximum elongation as represented in 6

a) i) infers Powder metallurgy produces the highest hardness of 684.49 HV for $x = 0.4$ and $y = 0.5$, making it the recommended MPEA system for applications prioritizing hardness. Regarding elongation, predictions made by our machine learning model for elongation values in the $D1_xD2_y(ZrHfNb)_{1-x-y}$ system are as follows: Each ternary plot corresponds to a specific dopant pair [D1,D2] and a particular manufacturing route. As detailed and demonstrated in Fig. 6 c), the alloy system $Ti_xTa_y(ZrHfNb)_{1-x-y}$, when manufactured through annealing, exhibits regions with significantly greater elongation values. The maximum elongation, reaching 43.52%, occurs at $x = 0.7$ and $y = 0$. This suggests that $Ti_{0.7}(ZrHfNb)_{0.3}$, when produced via annealing, possesses the highest ductility. This observation extends to another alloy system where Ti also proves to be a favorable dopant.

In the case of the $D1_xD2_y(VNbTa)_{1-x-y}$ system, the dopant pairs [Cr, W] and the powder metallurgy-based manufacturing route favor increased hardness. The alloy $Cr_{0.5}W_{0.3}(VNbTa)_{0.2}$, manufactured via sintering, exhibits the maximum hardness of 733.42 HV. This value represents the highest hardness among all alloy systems considered. Powder metallurgy emerges as the preferred method for preparing alloys with the highest hardness across all dopant pairs in $D1_xD2_y(VNbTa)_{1-x-y}$. Similarly, for predicted elongation distribution in the $D1_xD2_y(VNbTa)_{1-x-y}$ MPEA system. Analysis of the ternary diagrams indicates that when [Mo,Ti] dopants are added to the base VNbTa system, they provide the highest attainable ductility in the resulting MPEA. The maximum elongation value, 34.36%, is achieved by the $Mo_{0.1}Ti_{0.8}(VNbTa)_{0.1}$ MPEA when using wrought or miscellaneous fabrication procedures as represented in triangular contour in Fig. 6 a) ii).

Comparing the bar charts for elongation values of the $D1_xD2_y(ZrHfNb)_{1-x-y}$ and $D1_xD2_y(VNbTa)_{1-x-y}$ MPEA systems in Figure 6 c), it becomes evident that alloys compositionally designed with ZrHfNb generally exhibit superior ductility compared to those designed with VNbTa systems. Unlike the maximum hardness property (where powder metallurgy emerges as the most favorable fabrication route), there is no single preferred fabrication procedure associated with enhanced ductility for all dopant pairs and composition variants.

3.2.2. Optimal composition and fabrication route corresponding to hardness-ductility synergy

Advanced structural materials require an optimal balance between hardness and ductility. AlloyManufacturingNet enables the prediction of suitable fabrication routes and alloy compositions that exhibit favorable hardness-elongation synergy. By combining independent hardness and elongation (Sec. 3.2.1) models with the mathematical model represented by Eq. 3, an ensemble of neural networks can forecast specific MPEA (Multi-Principal Element Alloy) compositions and the corresponding manufacturing routes that yield optimal hardness and elongation values.

For ZrHfNb-based alloys, as shown in Fig. 6 c), $Cr_{0.8}W_{0.1}(ZrHfNb)_{0.1}$ produced through wrought processing exhibits excellent hardness at 511.81 HV and moderate elongation at 17.14%, making it suitable for applications where achieving high hardness is essential. Conversely, $Ti_{0.3}Ta_{0.4}(ZrHfNb)_{0.3}$, also manufactured via wrought processing, offers an excellent elongation of 37.95% with lower hardness (374.56 HV), making it a suitable choice for applications emphasizing high ductility. **Supplementary Table S4** reveals that the base ZrHfNb alloy, when cast, possesses hardness and elongation values of 426.91 HV and 32.99%, respectively. Meanwhile, using powdered metallurgy, the same alloy exhibits hardness and elongation of 383.54 HV and 31.68%. Hence, the first of the two alloys ($Cr_{0.8}W_{0.1}(ZrHfNb)_{0.1}$ and $Ti_{0.3}Ta_{0.4}(ZrHfNb)_{0.3}$) prepared via the wrought process suits applications requiring elevated hardness, whereas the second is more appropriate for applications requiring higher ductility. It can be inferred that wrought processing is recommended for fabricating MPEAs from the base ZrHfNb alloy to enhance either hardness or elongation. However, it is worth noting that a trade-off between hardness and elongation often exists in ZrHfNb alloys, making it challenging to achieve hardness-elongation synergy with the given dopants and various manufacturing processes.

Similarly, alloy combinations derived from VNbTa MEA, both $Cr_xW_y(VNbTa)_{1-x-y}$ and $Mo_xTi_y(VNbTa)_{1-x-y}$ systems fabricated using wrought processing appear to exhibit regions with favorable hardness-elongation synergy, as depicted in Fig. 6 c). For instance, $Cr_{0.7}(VNbTa)_{0.3}$ manufactured via the wrought process is predicted to possess excellent hardness (575.87 HV) and moderately good elongation (23.73%). Consequently, the alloy $Cr_xW_y(VNbTa)_{1-x-y}$ with x=0.7 and y=0, manufactured by wrought method (**Supplementary Table S5**), is suitable for structural applications that require high hardness. Similarly, when wrought processed, $Mo_xTi_y(VNbTa)_{1-x-y}$ alloys show hardness and elongation values of 566.43 HV and 27.79% at x=0.3 and y=0, respectively. Thus, $Mo_{0.3}(VNbTa)_{0.7}$ MPEA offers nearly equal hardness to $Cr_{0.7}(VNbTa)_{0.3}$ but with improved ductility. $Mo_{0.3}(VNbTa)_{0.7}$ alloy manufactured through wrought processing is estimated to possess excellent hardness-ductility synergy, especially favoring hardness. On the other hand, $Zr_{0.4}(VNbTa)_{0.6}$ MPEA produced via powder metallurgy is predicted to exhibit a hardness of 542.60 HV and elongation of 30.22%. This alloy also demonstrates a perfect combination of hardness-ductility synergy, albeit

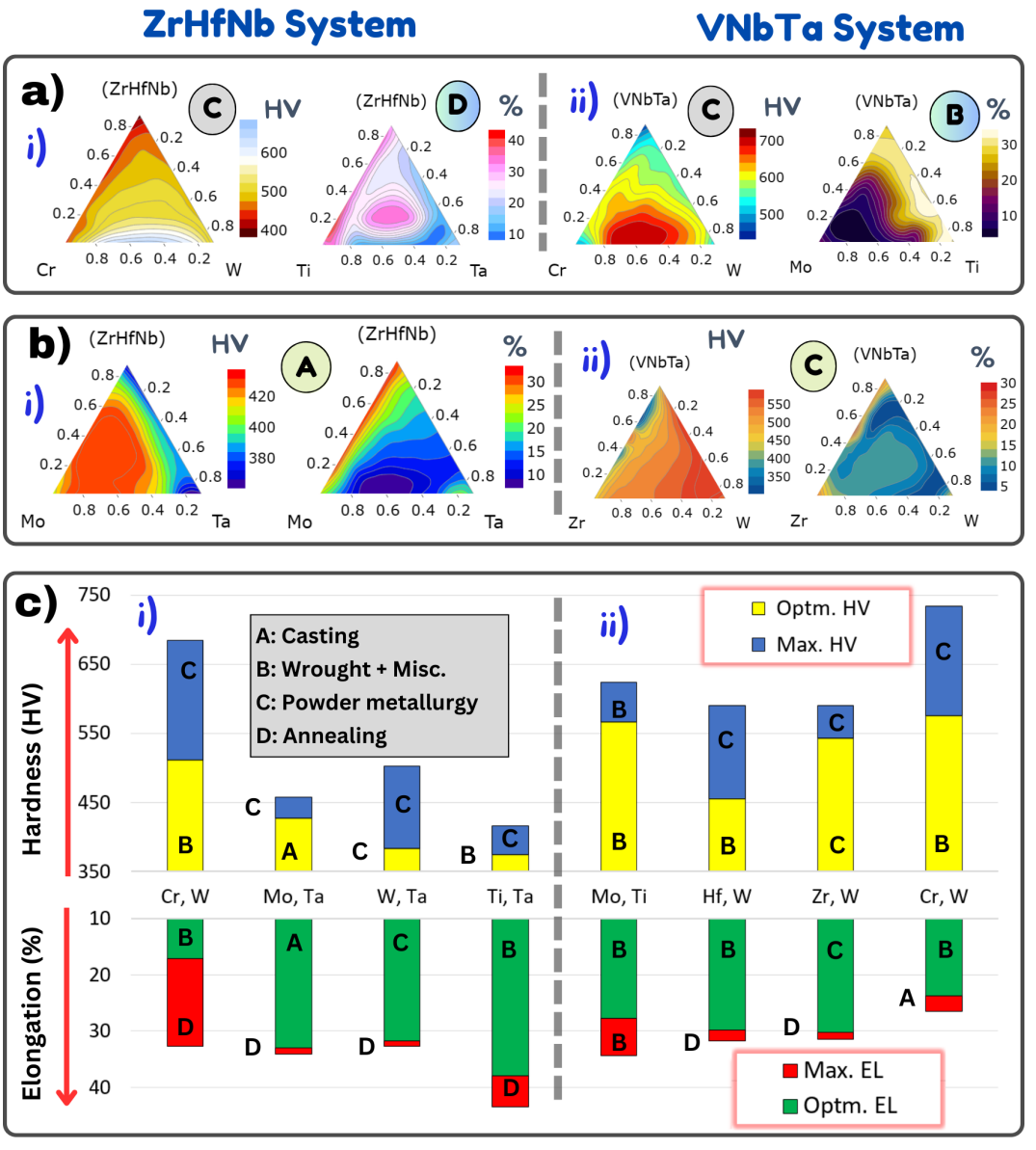

Figure 6: a) Maximum Hardness and Maximum Elongation Powder metallurgy results in the highest hardness (684.49 HV) when Cr = 0.4 and W = 0.5 in ZrHfNb. In the case of elongation, [Ti=0.7, Ta=0] with annealing yields 43.52%. For VNbTa, powder metallurgy with Cr = 0.5 and W = 0.3 achieves a hardness of 733.42 HV, while an elongation of 34.36% is obtained with Mo = 0.1 and Ti = 0.8 in the Wrought + Misc route. **b) Optimized hardness-elongation pairs** For, $Mo_0.6(ZrHfNb)_0.4$ with obtained from prediction model of AlloyManufacturingNet. **c)** The manufacturing route associated with the predictions is also provided as labels in the bar diagrams. It is to be noted that the single alloy composition and a single manufacturing route are associated with a specific optimal hardness-elongation pair. It is to be noted that the letters A, B, C and D drawn inside the colorful circles of a) and b) denote the manufacturing methods labeled in c) The detailed version of the specially highlighted results presented in this figure is provided in **Supplementary section S4**

favoring ductility. Notably, these MPEAs with improved hardness-elongation synergy typically comprise four elements, with a relatively higher proportion of the base alloy VNbTa. In terms of elements doped into the VNbTa system, wrought manufacturing and powder metallurgy are considered preferable methods for achieving a balance between elongation and hardness properties.

In contrast to alloys derived from the ZrHfNb system, MPEAs obtained from the base VNbTa system exhibit robust hardness-ductility synergy, quantitatively expressed through standardized and summed values of optimal hardness and optimal elongation features (refer to Eq. 3). For instance, in the case of $Cr_{0.8}W_{0.1}(ZrHfNb)_{0.1}$ (fabrication route = wrought + misc), the standardized hardness is +0.084, while the corresponding elongation is -0.264, resulting in an objective function value of -0.1802. This alloy falls into the category of less preferable candidates due to its negative standardized objective function value, despite having an overall positive objective function value. In contrast, $Ti_{0.3}Ta_{0.4}(ZrHfNb)_{0.3}$ MPEA (manufacturing route = wrought + misc) exhibits a highly favorable standardized elongation value (+0.83) but an undesirable standardized hardness value (-0.61), yielding an objective function value of +0.217. Although the objective function is positive, the negative hardness value renders this MPEA unsuitable for technological applications. The maximum attainable positive value of the overall objective function for ZrHfNb-derived MPEAs is +0.2229, found in the case of $Mo_{0.6}(ZrHfNb)_{0.4}$ alloy fabricated using the casting process. The standardized values of hardness and elongation for this alloy are -0.34 and +0.57, respectively. The lower value of the overall objective function in ZrHfNb-derived MPEAs can also be observed in ternary plots (**Supplementary Figs. S10 and S11**). For example, triangular diagrams corresponding to $Cr_xW_y(ZrHfNb)_{1-x-y}$ alloys prepared by the wrought procedure are positioned second from the top left corner in both figures. The region near the top corner of the triangle, highlighted by a rectangular box, consists of a large proportion of ZrHfNb (i.e., 1-x-y $\geq$ 0.8) and is characterized by high elongation and low hardness. Observing the 32 ternary plots in these figures, it can be inferred that, most of the time, a given composition of a $D1_xD2_y(ZrHfNb)_{1-x-y}$ alloy prepared by a specific manufacturing route corresponds to above-average hardness when elongation is below average, and vice versa. This observation implies that doping the ZrHfNb alloy system with these dopant pairs is unsuitable when aiming to achieve hardness-ductility synergy. However, MPEAs derived from the VNbTa base alloy system offer solutions to mitigate the trade-off between hardness and ductility. $Mo_{0.3}(VNbTa)_{0.7}$ (MR = wrought + misc) and $Zr_{0.4}(VNbTa)_{0.6}$ (MR = sintering) represent composition values and manufacturing routes that result in positive values for all three standardized quantities: the objective function, hardness, and elongation. These alloys are recommended for applications requiring a combination of enhanced hardness and greater ductility. $Mo_{0.3}(VNbTa)_{0.7}$ alloy exhibits standardized hardness and elongation values of +0.36 and +0.296, respectively, with a combined sum of +0.656 according to Eq. 3. Similarly, $Zr_{0.4}(VNbTa)_{0.6}$ alloy has standardized hardness and elongation values of +0.24 and +0.42, respectively, resulting in a sum of +0.6648 (the maximum value predicted thus far). Interestingly, it has been discovered that $Zr_xW_y(VNbTa)_{1-x-y}$ alloys offer composition values for each of the four manufacturing routes that exhibit positive standardized values for all three quantities (hardness, elongation, and the objective function). In **Supplementary Figs. S12 and S13**, triangular diagrams for $Zr_xW_y(VNbTa)_{1-x-y}$ for the four manufacturing routes are positioned on the top row. The region near the mid-length of the left side of these triangles, highlighted by a rectangular box, exhibits both excellent hardness and excellent ductility. Notably, this region is present in the alloy for all four manufacturing routes, making $Zr_xW_y(VNbTa)_{1-x-y}$ an optimal candidate for applications requiring excellent hardness-ductility synergy. The hardness-ductility favoring regions also exist in $Mo_xTi_y(VNbTa)_{1-x-y}$ alloys for three manufacturing routes, except for the casting process. In the context of $Cr_xW_y(VNbTa)_{1-x-y}$ MPEA, casting, wrought, and annealing processes offer composition proportions favoring hardness-ductility synergy, characterized by regions with high hardness and elongation. However, powder metallurgy does not favor this synergy. When using the dopant pairs Hf and W, the behavior of the VNbTa system is similar to that of the ZrHfNb alloy doped with [Cr,W], [Mo,Ta], [W,Ta], and [Ti,Ta] in most cases. This means that a given composition coordinate in the triangular diagrams of $Hf_xW_y(VNbTa)_{1-x-y}$ MPEA for wrought, sintering, and annealing procedures represents low hardness when elongation is high, and vice versa. In the case of casting, the situation is even worse, with overall hardness and elongation values for $Hf_xW_y(VNbTa)_{1-x-y}$ consistently below average throughout the composition points, indicating an absence of hardness-ductility synergy.

It is noteworthy to mention that the Figs. 6 a) and b) have a big prospect for being utilized in the design of digital manufacturing (metamorphic manufacturing) methods. The given composition of an MPEA can be checked in the ternary diagrams for hardness or elongation at different manufacturing methods. Importantly, the triangular diagrams have values of hardness and elongation for all sets of composition, so each and every composition value can be inspected. The information about any two different manufacturing routes imparting different hardness for a single alloy composition, then this information can be utilized to design a digitally controlled incremental forming system.

An online software tool can enable the performance of test, design, and discovery tasks for MPEAs, expediting the pursuit of hardness-ductility synergy in these class of materials. The prediction model of **AlloyManufacturingNet** has been launched online as a software app [73]. In the web interface, the user can perform two distinct operations - (i) ALLOY DESIGN, and (ii) HARDNESS-DUCTILITY OPTIMIZATION. The ALLOY DESIGN operation

is associated with the task of obtaining the hardness and elongation values independently for a given new alloy composition manufactured by a given process. When input information about the multi-principal element alloy's composition and fabrication type is provided by the user, the estimated hardness (in HV) and percentage elongation values are presented on the screen. Besides the target values, the input features (including VEC) and Pugh's ratio are also automatically shown by the software. The user can select between default category (which includes the mixture set of tension and compression datasets), compression tests only, and tensile tests only to find the corresponding values of estimated elongation percentage. It is important to note that the software predicts well for ductile and highly ductile MPEAs and it is not recommended for use in materials with ductility less than 5 %. The software performs well for all range of hardness values. In context of the HARDNESS-DUCTILITY SYNERGY OPTIMIZATION task, besides providing the information about base alloy composition, manufacturing route, and test type; the user also has to supply the names of two dopant elements. The software then outputs two ternary diagrams one for hardness distribution and another for ductility distribution in the doped MPEAs. In addition to this, AlloyManufacturingNet also maps the composition data in the Hardness-Elongation chart. Such scatter data can inform the user in knowing the compositions (for a given manufacturing process) that possess good hardness+good ductility; excellent hardness only and excellent ductility only.

3.3. Coupling nanoscale simulation with prediction result at macroscale for Nb-doped CoCrNi MPEA to analyze the hardness

The medium entropy alloy CoCrNi has piqued the interest of materials scientists and engineers for various reasons. It has been demonstrated that this ternary equiatomic MEA possesses greater toughness and strength than the quinary equiatomic CrCoFeMnNi high entropy alloy [74]. This notable strength-ductility synergy in CoCrNi MEA has been attributed to its low stacking fault energy [75]. Numerous efforts have been made to improve the mechanical properties of CoCrNi MEA by introducing dopants in varying proportions [76]. In our pursuit of enhancing hardness, we present our study on doping CoCrNi with Nb atoms. Figure 7(a) displays the hardness values estimated by the AlloyManufacturingNet for Nb-doped CoCrNi alloys fabricated via the casting procedure. It can be observed that hardness increases with an increasing amount of Nb in the $CoCrNiNb_x$ MPEA. To optimize the material properties, we employ the ensemble model to predict the elongation feature of $CoCrNiNb_x$ alloy (manufactured using the casting route), and the results are presented in Figure 7(b). The data reveals that the elongation of the CoCrNi alloy initially decreases with the addition of Nb, reaching its lowest point at $x = 0.25$. In other words, Nb has a negative impact on ductility in $CoCrNiNb_x$ for values of $x \leq 0.25$. While the CoCrNi alloy exhibits the highest ductility, with an elongation of nearly 30%, the $CoCrNiNb_{0.25}$ alloy has the lowest ductility, with an elongation slightly below 20%. However, for $x > 0.25$, ductility is observed to increase again with the rise in Nb content.

From the perspective of hardness-ductility synergy, it is recommended to design materials and devices with $CoCrNiNb_x$ compositions where the Nb proportion (x) exceeds 0.25, particularly when employing the casting manufacturing procedure. At $x = 0.6$, the $CoCrNiNb_x$ MPEA exhibits a hardness of approximately 600 HV and an elongation well above 20%. Although the exact property values (hardness and elongation) may vary, and the specific value of x associated with minimum elongation may change with different manufacturing routes, it has been confirmed that the trends in hardness and elongation curves are consistent across all four manufacturing categories. Therefore, we will focus on the MPEA produced via the casting procedure in this section to understand the mechanism of hardness enhancement with Nb content. It is to be noted that the training datasets for hardness in the ensemble learning models correspond to millimeters (continuum scale) sized samples. For accurate understanding of the materials science of the MPEAs, it is always important to relate the macroscale behavior with structure-property relationship studied at atomic scale or nanoscale.

In the context of predicting the hardness of $CoCrNiNb_x$ MPEA, understanding the structure-property relationship is crucial. While CoCrNi typically has a face-centered cubic (FCC) crystal structure, $CoCrNiNb_x$ with a higher Nb proportion can exhibit a different crystal structure. Our previous work [27] highlighted that $CoCrNiNb_{0.5}$ MPEA exists as an IMC phase, while Lu et al. [77] reported that the Nb-rich phase in $CoCrNiNb_x$ MPEA corresponds to a hexagonal close-packed (HCP) Laves phase. These different crystal structures can influence the mechanical behavior of Nb-rich and Nb-deficient $CoCrNiNb_x$ MPEA / CoCrNi MEA. A nanoscale computational analysis can provide insights into the behavior of these alloys.

In this study, we selected MEA CoCrNi (with atoms arranged in an FCC structure) and $CoCrNiNb_{0.6}$ MPEA (with a unit cell of HCP structure) for nanoscale indentation tests. We conducted atomistic simulations for nanoindentation using Molecular Dynamics (MD) methods with LAMMPS software [78]. The supercells of CoCrNi and $CoCrNiNb_{0.6}$

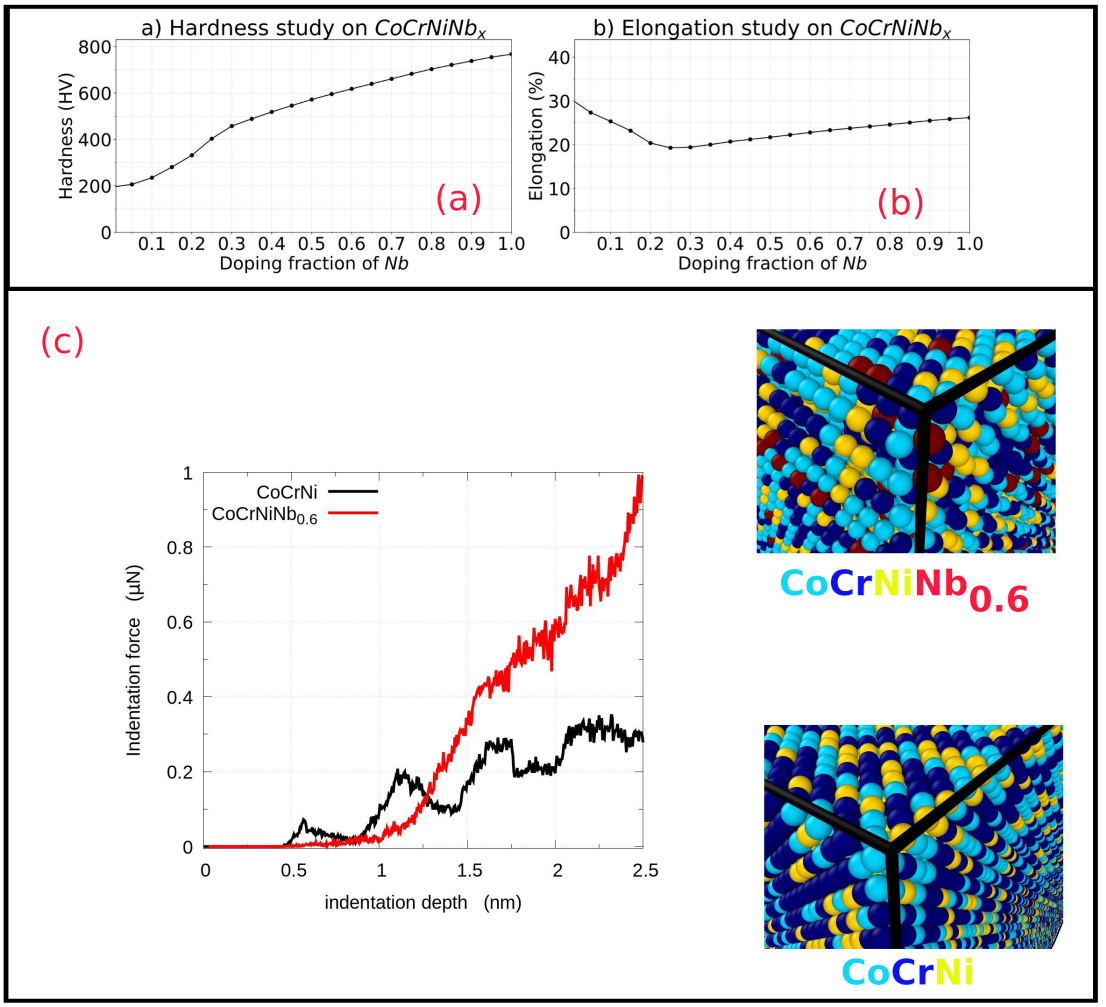

Figure 7: Predicting the variation of (a) hardness and (b) elongation with the change of Nb dopant proportion (x) in the CoCrNiNb$_x$ MPEA at macroscale (specimen samples in the dimension of mm) using the ensemble neural networks. The manufacturing route for the predicted alloys is casting process. The two alloy variants CoCrNi (absence of Nb element) and CoCrNiNb$_{0.6}$ are chosen as the candidates for the virtual nanoindentation test using molecular dynamics (MD). The results for the plots of indentation force against indentation depth during the MD simulations are presented in (c). The color of atoms of a given element in the slabs of these two alloys are expressed by the font color of the element in the alloy name (below the image of the nano slab). In the CoCrNi and CoCrNiNb$_{0.6}$ nano slab, Co, Cr, and Ni atoms are represented by spheres of sky blue, dark blue and yellow colors respectively. Nb atoms, present in CoCrNiNb$_{0.6}$ nanoslab but absent in CoCrNi nano slab, are represented by red color. The atomic arrangement in the slabs cores. The nanoscale simulation being in line with the macroscale prediction of hardness, reveals that the macroscale response of a MPEA regarding hardness is contributed by mechanisms occuring at nanoscale or atomic scale.

MPEAs were constructed using Atomsk software [79]. The CoCrNi nanoslab consisted of 600,000 atoms, while the CoCrNiNb$_{0.6}$ nanostructure consisted of 602,688 atoms. We visualized the nanoslabs and analyzed the MD simulation results using OVITO software [80]. We used a non-atomic spherical indenter (radius = 5 nm, specific force constant = 1000 eV/Å^3). The indenter initially touched the top of the nano slabs and then moved vertically downward at a rate of 0.5 Å/ps. The results of the MD simulation, showing the variation of indentation force (in μN) with the indentation depth (in nm), are presented in Fig.7(c).

The black curves in the figure represent the indentation force exerted on the spherical indenter by the constituent atoms (Co, Cr, and Ni) of the FCC CoCrNi alloy. The force shows a peak-valley profile, starting from near-zero and

reaching a peak value of 0.2 μN, then decreasing before rising again with larger peaks. In contrast, the red curve represents the indentation force for HCP $CoCrNiNb_{0.6}$. It remains negligible until the indenter reaches a depth of 1 nm. Beyond this depth, the force increases continuously as the indenter penetrates the material, without a peak-valley profile. When the indenter reaches a depth of 2.5 nm, the indentation force for CoCrNi MPEA is around 0.3 μN, while that for $CoCrNiNb_{0.6}$ is approaching 1.0 μN. These different indentation profiles provide mechanistic insight into the role of Nb-doping in promoting the hardness of the alloy. The presence of Nb in larger amounts alters the interaction mechanism among the constituent atoms, strengthening their cohesion and resistance to the indenter. The initial arrangement of Co, Cr, Ni, and Nb in an HCP unit cell allows for enhanced flexibility in atom rearrangement through dislocation motions and twinning, leading to a robust nanostructure that provides greater resistance force. The MD simulation results (performed at nanoscale) confirm the predictions from the ensemble model (built on the data obtained from continuum scale experiments), validating the latter as a physically explainable machine learning model.

4. Conclusion

In this study, we developed a data-driven machine learning ensemble neural network model to predict the hardness and elongation of multi-principal element alloys (MPEAs). We trained the model using selected features and fabrication routes, optimizing hyper-parameters through hyper-parameter tuning. The trained model allowed us to make predictions for both hardness and elongation of the MPEA system. Additionally, we visualized how hardness and elongation vary with changes in the composition of certain elemental components using ternary plots. An online software application has been developed to estimate hardness-elongation values. The software currently provides accurate predictions across a wide range of hardness levels but is particularly effective for ductile and highly ductile MPEAs.

Here are the key conclusions from our work:

- We constructed a weighted ensemble of four neural networks based on feature sets derived from feature selection engineering techniques, including PCC heatmap, VIF, and PCA for predicting hardness and elongation.
- Alloy design was performed for both ZrHfNb- and VNbTa-derived MPEAs based on maximum hardness criteria. The optimal combinations were [Cr, W] dopant pairs and sintering (powder metallurgy) manufacturing routes, resulting in hardness values of 684.49 HV for $Cr_{0.4}W_{0.5}(ZrHfNb)_{0.1}$ and 733.42 HV for $Cr_{0.5}W_{0.3}(VNbTa)_{0.2}$.
- Elongation-based alloy design revealed $Ti_{0.7}(ZrHfNb)_{0.3}$ prepared via annealing as the alloy with the highest elongation of 43.52% among all candidates. For VNbTa-derived MPEAs, $Mo_{0.1}Ti_{0.8}(VNbTa)_{0.1}$ processed through the wrought manufacturing route exhibited an elongation of 34.36%. Ti was identified as a favorable dopant for improving elongation properties in both alloy categories.
- To achieve a hardness-ductility synergy-based composition design of MPEAs, we introduced a scale-invariant optimization technique for maximizing the objective function of both mechanical properties. The results indicated that VNbTa-derived MPEAs were more suitable for achieving an optimal combination of hardness and elongation.
- We also investigated the hardness enhancement in Nb-doped CoCrNi alloys manufactured by casting. The study revealed that as the Nb content (x) increased in $CoCrNiNb_x$ MPEAs, hardness increased proportionally. Elongation decreased for $x \leq 0.25$ and increased for $x > 0.25$, indicating that a higher proportion of Nb is preferable for hardness-elongation synergy.
- Finally, we used a numerical approach, specifically the MD method, to perform nanoindentation tests on FCC CoCrNi and HCP $CoCrNiNb_{0.6}$ alloys. This allowed us to gain mechanistic insights into how the dopant influences the mechanical behavior of MPEAs.

Declaration of Competing Interests

The authors declare that they have no known competing financial interests or personal relationships that could have appeared to influence the work reported in this paper.

Data Availability

The codes and data of AlloyManufacturingNet for the construction of the machine learning models in this study are made available at https://github.com/Sachinscnpdl/MPEA_HV-EL. The visualization and interactive web application of the code is available at https://mpeanet.streamlit.app/.

Acknowledgments

This work was supported by the National Science Centre, Poland (UMO-2021/42/E/ST5/00339), the University Grants Commission, Nepal (Award No.: MRS-78-79-Engg-10) and the European Research Council (ERC) under the European Union's Horizon 2020 research and innovation program (INTERDIFFUSION, Grant Agreement No. 714754).

Author Contributions

Sachin Poudel: Conceptualization, Methodology, Investigation, Validation, Formal analysis, Software, Data curation, Visualization, Funding acquisition, Writing - original draft. **Upadesh Subedi:** Methodology, Validation, Visualization, Formal analysis, Writing - review & editing. **Mohammed O.A. Hamid:** Validation, Formal analysis, Writing - review & editing. **Khem Gyanwali:** Supervision, Validation, Resources, Writing - review & editing. **Nele Moelans:** Methodology, Validation, Supervision, Funding acquisition, Writing - review & editing. **Anna Timofiejczuk:** Validation, Supervision, Data curation, Visualization, Resources, Writing - review & editing. **Anil Kunwar:** Conceptualization, Investigation, Methodology, Software, Validation, Visualization, Data curation, Formal analysis, Resources, Supervision, Project administration, Funding acquisition, Writing – review & editing.

Supplementary Information

The supplementary material is attached as a pdf file along with this manuscript.

References

[1] C. Zhang, J. Zhu, H. Zheng, H. Li, S. Liu, G. J. Cheng, A review on microstructures and properties of high entropy alloys manufactured by selective laser melting, International Journal of Extreme Manufacturing 2 (2020) 032003.

[2] B. MacDonald, Z. Fu, B. Zheng, W. Chen, Y. Lin, F. Chen, L. Zhang, J. Ivanisenko, Y. Zhou, H. Hahn, et al., Recent progress in high entropy alloy research, Jom 69 (2017) 2024–2031.

[3] O. N. Senkov, D. B. Miracle, K. J. Chaput, J.-P. Couzinie, Development and exploration of refractory high entropy alloys—a review, Journal of materials research 33 (2018) 3092–3128.

[4] D. B. Miracle, O. N. Senkov, A critical review of high entropy alloys and related concepts, Acta Materialia 122 (2017) 448–511.

[5] X. Tan, Y. Tang, Y. Tan, Q. Deng, H. Jiao, Y. Yang, H. Xu, Correlation between microstructure and soft magnetic parameters of fe-co-ni-al medium-entropy alloys with fcc phase and bcc phase, Intermetallics 126 (2020) 106898.

[6] J.-W. Yeh, S.-K. Chen, S.-J. Lin, J.-Y. Gan, T.-S. Chin, T.-T. Shun, C.-H. Tsau, S.-Y. Chang, Nanostructured high-entropy alloys with multiple principal elements: novel alloy design concepts and outcomes, Advanced engineering materials 6 (2004) 299–303.

[7] W. Lu, X. Luo, Y. Yang, W. Le, B. Huang, P. Li, Co-free non-equilibrium medium-entropy alloy with outstanding tensile properties, Journal of Alloys and Compounds 833 (2020) 155074.

[8] Y. Han, H. Li, H. Feng, K. Li, Y. Tian, Z. Jiang, Enhancing the strength and ductility of cocrfemnni high-entropy alloy by nitrogen addition, Materials Science and Engineering: A 789 (2020) 139587.

[9] F. Thiel, D. Geissler, K. Nielsch, A. Kauffmann, S. Seils, M. Heilmaier, D. Utt, K. Albe, M. Motylenko, D. Rafaja, et al., Origins of strength and plasticity in the precious metal based high-entropy alloy aucunipdpt, Acta Materialia 185 (2020) 400–411.

[10] F. Průša, M. Cabibbo, A. Šenková, V. Kučera, Z. Veselka, A. Školáková, D. Vojtěch, J. Cibulková, J. Čapek, High-strength ultrafine-grained cocrfeninb high-entropy alloy prepared by mechanical alloying: Properties and strengthening mechanism, Journal of Alloys and Compounds 835 (2020) 155308.

[11] F. Tian, L. K. Varga, N. Chen, J. Shen, L. Vitos, Empirical design of single phase high-entropy alloys with high hardness, Intermetallics 58 (2015) 1–6.

[12] S. Yang, Z. Liu, J. Pi, Microstructure and wear behavior of the alcrfeconi high-entropy alloy fabricated by additive manufacturing, Materials Letters 261 (2020) 127004.

[13] V. Soni, B. Gwalani, T. Alam, S. Dasari, Y. Zheng, O. N. Senkov, D. Miracle, R. Banerjee, Phase inversion in a two-phase, bcc+ b2, refractory high entropy alloy, Acta Materialia 185 (2020) 89–97.

[14] Y. Zhao, T. Yang, Y. Li, L. Fan, B. Han, Z. Jiao, D. Chen, C. Liu, J. Kai, Superior high-temperature properties and deformation-induced planar faults in a novel l12-strengthened high-entropy alloy, Acta Materialia 188 (2020) 517–527.

[15] B. Gludovatz, A. Hohenwarter, D. Catoor, E. H. Chang, E. P. George, R. O. Ritchie, A fracture-resistant high-entropy alloy for cryogenic applications, Science 345 (2014) 1153–1158.
[16] Z. Li, D. Raabe, Strong and ductile non-equiatomic high-entropy alloys: design, processing, microstructure, and mechanical properties, Jom 69 (2017) 2099–2106.
[17] D. Miracle, High entropy alloys as a bold step forward in alloy development, Nature communications 10 (2019) 1–3.
[18] S. Guo, Phase selection rules for cast high entropy alloys: an overview, Materials Science and Technology 31 (2015) 1223–1230.
[19] S.-M. Liang, R. Schmid-Fetzer, Evaluation of calphad approach and empirical rules on the phase stability of multi-principal element alloys, Journal of Phase Equilibria and Diffusion 38 (2017) 369–381.
[20] Y.-c. Liu, S.-y. Yen, S.-h. Chu, S.-k. Lin, M.-H. Tsai, Mechanical and thermodynamic data-driven design of al-co-cr-fe-ni multi-principal element alloys, Materials Today Communications 26 (2021) 102096.
[21] P. Singh, A. V. Smirnov, A. Alam, D. D. Johnson, First-principles prediction of incipient order in arbitrary high-entropy alloys: exemplified in ti0. 25crfenialx, Acta Materialia 189 (2020) 248–254.
[22] J. Startt, A. Kustas, J. Pegues, P. Yang, R. Dingreville, Compositional effects on the mechanical and thermal properties of monbtati refractory complex concentrated alloys, Materials & Design 213 (2022) 110311.
[23] S. Mishra, S. Maiti, B. Rai, Computational property predictions of ta–nb–hf–zr high-entropy alloys, Scientific Reports 11 (2021) 1–12.
[24] L. Zhang, K. Qian, B. W. Schuller, Y. Shibuta, Prediction on mechanical properties of non-equiatomic high-entropy alloy by atomistic simulation and machine learning, Metals 11 (2021) 922.
[25] Z. Pei, J. Yin, J. A. Hawk, D. E. Alman, M. C. Gao, Machine-learning informed prediction of high-entropy solid solution formation: Beyond the hume-rothery rules, npj Computational Materials 6 (2020) 1–8.
[26] S. Hernandez, Development of Methods for Reducing the Cost of Density Functional Theory and Time-Dependent Density Functional Theory, Ph.D. thesis, UCLA, 2015.
[27] U. Subedi, A. Kunwar, Y. A. Coutinho, K. Gyanwali, pympealab toolkit for accelerating phase design in multi-principal element alloys, Metals and Materials International 28 (2022) 269–281.
[28] N. Islam, W. Huang, H. L. Zhuang, Machine learning for phase selection in multi-principal element alloys, Computational Materials Science 150 (2018) 230–235.
[29] M. Chausov, A. Pylypenko, P. Maruschak, A. Menou, Phenomenological models and peculiarities of evaluating fatigue life of aluminum alloys subjected to dynamic non-equilibrium processes, Metals 11 (2021) 1625.
[30] C. Wen, Y. Zhang, C. Wang, D. Xue, Y. Bai, S. Antonov, L. Dai, T. Lookman, Y. Su, Machine learning assisted design of high entropy alloys with desired property, Acta Materialia 170 (2019) 109–117.
[31] Y.-J. Chang, C.-Y. Jui, W.-J. Lee, A.-C. Yeh, Prediction of the composition and hardness of high-entropy alloys by machine learning, Jom 71 (2019) 3433–3442.
[32] U. Bhandari, C. Zhang, C. Zeng, S. Guo, A. Adhikari, S. Yang, Deep learning-based hardness prediction of novel refractory high-entropy alloys with experimental validation, Crystals 11 (2021) 46.
[33] M. Bakr, J. Syarif, I. A. T. Hashem, Prediction of phase and hardness of heas based on constituent elements using machine learning models, Materials Today Communications 31 (2022) 103407.
[34] D. Beniwal, P. Singh, S. Gupta, M. Kramer, D. Johnson, P. Ray, Distilling physical origins of hardness in multi-principal element alloys directly from ensemble neural network models, npj Computational Materials 8 (2022) 1–11.
[35] A. Paganotti, C. Bessa, L. Silva, R. Silva, Metallic sample preparation for phase transformation analysis, MethodsX 6 (2019) 2348–2366.
[36] W.-H. Lee, K. B. Park, K.-W. Yi, S. Y. Lee, K. Park, T. W. Lee, T.-W. Na, H.-K. Park, Synthesis of spherical v-nb-mo-ta-w high-entropy alloy powder using hydrogen embrittlement and spheroidization by thermal plasma, Metals 9 (2019) 1296.
[37] Y. Dong, Y. Lu, J. Kong, J. Zhang, T. Li, Microstructure and mechanical properties of multi-component alcrfenimox high-entropy alloys, Journal of alloys and compounds 573 (2013) 96–101.
[38] P. Yasnii, P. Marushchak, V. Hlad'o, D. Y. Baran, Correlation of the microdislocation parameters with the hardness of plastically deformed heat-resistant steels, Materials Science 44 (2008) 194–200.
[39] A. Jha, B. Prasad, O. Modi, S. Das, A. Yegneswaran, Correlating microstructural features and mechanical properties with abrasion resistance of a high strength low alloy steel, Wear 254 (2003) 120–128.
[40] P. Singh, B. Vela, G. Ouyang, N. Argibay, J. Cui, R. Arroyave, D. D. Johnson, A ductility metric for refractory-based multi-principal-element alloys, Acta Materialia 257 (2023) 119104.
[41] S. Pugh, Xcii. relations between the elastic moduli and the plastic properties of polycrystalline pure metals, The London, Edinburgh, and Dublin Philosophical Magazine and Journal of Science 45 (1954) 823–843.
[42] M. A. Hadi, M. T. Nasir, M. Roknuzzaman, M. A. Rayhan, S. H. Naqib, A. K. M. A. Islam, First-principles prediction of mechanical and bonding characteristics of new t2 superconductor ta5geb2, physica status solidi (b) 253 (2016) 2020–2026.
[43] D. G. Pettifor, M. Aoki, J. N. Murrell, A. Cottrell, A. M. Stoneham, R. Haydock, J. E. Inglesfield, J. B. Pendry, Bonding and structure of intermetallics: a new bond order potential, Philosophical Transactions of the Royal Society of London. Series A: Physical and Engineering Sciences 334 (1991) 439–449.
[44] D. G. Pettifor, Theoretical predictions of structure and related properties of intermetallics, Materials Science and Technology 8 (1992) 345–349.
[45] T. Yang, Y. L. Zhao, W. H. Liu, J. H. Zhu, J. J. Kai, C. T. Liu, Ductilizing brittle high-entropy alloys via tailoring valence electron concentrations of precipitates by controlled elemental partitioning, Materials Research Letters 6 (2018) 600–606.
[46] K. Balasubramanian, S. V. Khare, D. Gall, Valence electron concentration as an indicator for mechanical properties in rocksalt structure nitrides, carbides and carbonitrides, Acta Materialia 152 (2018) 175–185.
[47] G. S. Daehn, A. Taub, Metamorphic manufacturing: The third wave in digital manufacturing, Manufacturing Letters 15 (2018) 86–88. Industry 4.0 and Smart Manufacturing.

[48] Z. Liu, D. Kumar, S. Jirathearanat, W. H. Wong, A multiple-tool method for fast fem simulation of incremental sheet forming process, The International Journal of Advanced Manufacturing Technology (2023).
[49] S. Dasari, V. Chaudhary, B. Gwalani, A. Jagetia, V. Soni, S. Gorsse, R. V. Ramanujan, R. Banerjee, Highly tunable magnetic and mechanical properties in an al0.3cofeni complex concentrated alloy, Materialia 12 (2020) 100755.
[50] V. Bolon-Canedo, B. Remeseiro, Feature selection in image analysis: a survey, Artificial Intelligence Review 53 (2020) 2905–2931.
[51] H. Kabir, N. Garg, Machine learning enabled orthogonal camera goniometry for accurate and robust contact angle measurements, Scientific Reports 13 (2023) 1497.
[52] C. K. Borg, C. Frey, J. Moh, T. M. Pollock, S. Gorsse, D. B. Miracle, O. N. Senkov, B. Meredig, J. E. Saal, Expanded dataset of mechanical properties and observed phases of multi-principal element alloys, Scientific Data 7 (2020) 1–6.
[53] J. Xiong, S.-Q. Shi, T.-Y. Zhang, Machine learning of phases and mechanical properties in complex concentrated alloys, Journal of Materials Science & Technology 87 (2021) 133–142.
[54] S. Gorsse, M. Nguyen, O. N. Senkov, D. B. Miracle, Database on the mechanical properties of high entropy alloys and complex concentrated alloys, Data in brief 21 (2018) 2664–2678.
[55] G. Salishchev, M. Tikhonovsky, D. Shaysultanov, N. Stepanov, A. Kuznetsov, I. Kolodiy, A. Tortika, O. Senkov, Effect of mn and v on structure and mechanical properties of high-entropy alloys based on cocrfeni system, Journal of Alloys and Compounds 591 (2014) 11–21.
[56] S. S. Thomas Chan Hien Dam, Ductilizing refractory high entropy alloys (2016).
[57] W. Jiang, X. Wang, H. Kang, B. Jiang, D. Dong, Y. Wang, D. Zhu, Microstructure and mechanical properties of alnbtivzr system refractory high entropy alloys, Journal of Alloys and Compounds 925 (2022) 166767.
[58] U. Subedi, Y. A. Coutinho, P. B. Malla, K. Gyanwali, A. Kunwar, Automatic featurization aided data-driven method for estimating the presence of intermetallic phase in multi-principal element alloys, Metals 12 (2022) 964.
[59] A. Roy, I. Roy, L. J. Santodonato, G. Balasubramanian, Data-guided feature identification for predicting specific heat of multicomponent alloys, JOM 74 (2022) 1406–1413.
[60] H. Khakurel, M. Taufique, A. Roy, G. Balasubramanian, G. Ouyang, J. Cui, D. D. Johnson, R. Devanathan, Machine learning assisted prediction of the young's modulus of compositionally complex alloys, Scientific reports 11 (2021) 1–10.
[61] V. Revi, S. Kasodariya, A. Talapatra, G. Pilania, A. Alankar, Machine learning elastic constants of multi-component alloys, Computational Materials Science 198 (2021) 110671.
[62] Z. T. Y. Liu, D. Gall, S. V. Khare, Electronic and bonding analysis of hardness in pyrite-type transition-metal pernitrides, Phys. Rev. B 90 (2014) 134102.
[63] O. N. Senkov, D. B. Miracle, Generalization of intrinsic ductile-to-brittle criteria by pugh and pettifor for materials with a cubic crystal structure, Scientific Reports 11 (2021) 4531.
[64] J. Kitagawa, K. Hoshi, Y. Kawasaki, R. Koga, Y. Mizuguchi, T. Nishizaki, Superconductivity and hardness of the equiatomic high-entropy alloy hfmonbtizr, Journal of Alloys and Compounds 924 (2022) 166473.
[65] F. Tian, L. K. Varga, N. Chen, J. Shen, L. Vitos, Empirical design of single phase high-entropy alloys with high hardness, Intermetallics 58 (2015) 1–6.
[66] J. Kitagawa, Magnetic properties, electrical resistivity, and hardness of high-entropy alloys feconipd and feconipt, Journal of Magnetism and Magnetic Materials 563 (2022) 170024.
[67] T. Hattori, Y. Watanabe, T. Nishizaki, K. Hiraoka, M. Kakihara, K. Hoshi, Y. Mizuguchi, J. Kitagawa, Metallurgy, superconductivity, and hardness of a new high-entropy alloy superconductor ti-hf-nb-ta-re, Journal of Alloys and Metallurgical Systems 3 (2023) 100020.
[68] A. Kunwar, P. B. Malla, J. Sun, L. Qu, H. Ma, Convolutional neural network model for synchrotron radiation imaging datasets to automatically detect interfacial microstructure: An in situ process monitoring tool during solar pv ribbon fabrication, Solar Energy 224 (2021) 230–244.
[69] A. Kunwar, Y. A. Coutinho, J. Hektor, H. Ma, N. Moelans, Integration of machine learning with phase field method to model the electromigration induced cu6sn5 imc growth at anode side cu/sn interface, Journal of Materials Science & Technology 59 (2020) 203–219.
[70] S. Kwak, J. Kim, H. Ding, X. Xu, R. Chen, J. Guo, H. Fu, Machine learning prediction of the mechanical properties of γ-tial alloys produced using random forest regression model, Journal of Materials Research and Technology 18 (2022) 520–530.
[71] Z. Pei, K. A. Rozman, O. N. Dogan, Y. Wen, N. Gao, E. A. Holm, J. A. Hawk, D. E. Alman, M. C. Gao, Machine-learning microstructure for inverse material design, Advanced Science 8 (2021) 2101207.
[72] J. Yu, S. Xi, S. Pan, Y. Wang, Q. Peng, R. Shi, C. Wang, X. Liu, Machine learning-guided design and development of metallic structural materials, Journal of Materials Informatics 1 (2021) 9.
[73] S. Poudel, A. Kunwar, AlloyManufacturingNet: Hardness-Ductility Synergy Design Tool, https://mpeanet.streamlit.app/, 2023. Accessed: 21.09.2023.
[74] F. G. Coury, K. D. Clarke, C. S. Kiminami, M. J. Kaufman, A. J. Clarke, High throughput discovery and design of strong multicomponent metallic solid solutions, Scientific Reports 8 (2018) 8600.
[75] J. Ge, C. Chen, R. Zhao, Q. Liu, Y. Long, J. Wang, Z. Ren, S. Yin, Strength-ductility synergy of cocrni medium-entropy alloy processed with laser powder bed fusion, Materials & Design 219 (2022) 110774.
[76] H. Chang, T. Zhang, S. Ma, D. Zhao, R. Xiong, T. Wang, Z. Li, Z. Wang, Novel si-added crconi medium entropy alloys achieving the breakthrough of strength-ductility trade-off, Materials & Design 197 (2021) 109202.
[77] Effects of nb additions on structure and mechanical properties evolution of cocrni medium-entropy alloy, Materials Express 9 (2019).
[78] S. Plimpton, Fast parallel algorithms for short-range molecular dynamics, Journal of Computational Physics 117 (1995) 1–19.
[79] P. Hirel, Atomsk: A tool for manipulating and converting atomic data files, Computer Physics Communications 197 (2015) 212–219.
[80] A. Stukowski, Visualization and analysis of atomistic simulation data with OVITO-the Open Visualization Tool, Modelling and Simulation in Materials Science and Engineering 18 (2010).

Supplementary Information:

AlloyManufacturingNet for discovery and design of hardness-elongation synergy in multi-principal element alloys

S1. Feature Engineering

In order to start a machine learning model, the initial task is to roughly establish a set of features that are deemed useful in relation to modeling the prescribed mechanical behavior in the multi-principal element alloys (MPEAs). As illustrated in Table S1, this study initially considers 15 variables in the original feature pool. The mathematical expressions needed to perform the numerical fingerprinting of these features are also provided in the table.

In the mathematical expression, the subscript i and j associated with a term corresponds respectively to element i and element j in the MPEA. For an example, C_i is the mole fraction, z_i is atomic number, and r_i is the atomic radius of the i^{th} element in the MPEA. The overline associated with a property denotes the composition weighted sum ofthe properties of the individual elements in the alloy. R = 8.314 $Jmol^{-1}K^{-1}$ is gas constant, and ΔH_{AB} is the binary entropy of mixing at equal composition.

Table S1: Each input feature in the feature pool is provided with a corresponding mathematical expression.

SN	Name of Features	Mathematical expression	Ref.
1	Mean Atomic Radius difference (δ)	$\delta = \sqrt{\sum_{i=1}^{n} C_i \left(1 - \frac{r_i}{\bar{r}}\right)^2}$	Yang & Zhang (2012)
2	Electronegativity asymmetry ($\Delta\chi$)	$\Delta\chi = \sqrt{\sum_{i=1}^{n} C_i \left(\chi_i - \bar{\chi}\right)^2}$	Fang et al. (2003)
3	Average Melting Temperature (T_m)	$T_m = \sum_{i=1}^{n} C_i \left(T_i\right)$	Senkov et al. (2010)
4	Average Melting Temperature asymmetry (ΔT_m)	$\Delta T_m = \sqrt{\sum_{i=1}^{n} C_i \left(T_i - \bar{T}\right)^2}$	
5	Valence Electron Concentration (VEC)	$VEC = \sum_{i=1}^{n} C_i \left(VEC\right)_i$	Guo et al. (2011)
6	Average Atomic Number (AN)	$AN = \sum_{i=1}^{n} C_i \left(z_i\right)$	
7	Thermal Conductivity (K)	$K = \sum_{i=1}^{n} C_i \left(K_i\right)$	
8	Average Bulk Modulus (B)	$B = \sum_{i=1}^{n} C_i \left(B_i\right)$	
9	Bulk Modulus asymmetry (ΔB)	$\Delta B = \sqrt{\sum_{i=1}^{n} C_i \left(1 - \frac{B_i}{\bar{B}}\right)^2}$	
10	Average Shear Modulus (G)	$G = \sum_{i=1}^{n} C_i \left(G_i\right)$	
11	Shear Modulus asymmetry (ΔG)	$\Delta G = \sqrt{\sum_{i=1}^{n} C_i \left(1 - \frac{G_i}{\bar{G}}\right)^2}$	
12	Entropy of Mixing asymmetry (ΔS_{mix})	$\Delta S_{mix} = -R \sum_{i=1}^{n} \left(C_i ln C_i\right)$	Takeuchi & Inoue (2005)
13	Enthalpy of Mixing asymmetry (ΔH_{mix})	$\Delta H_{mix} = \sum_{i=1, i\neq j}^{n} \left(\Delta H_{AB} C_i C_j\right)$	Guo et al. (2011)
14	Geometrical Parameter (λ)	$\lambda = \frac{\Delta S_{mix}}{\delta^2}$	Singh et al. (2014)
15	Dimensionless parameter (Ω)	$\Omega = \frac{T_m \, \Delta S_{mix}}{\lvert \Delta H_{mix} \rvert}$	Yang & Zhang (2012)

S1.1. Principal Component Analysis (PCC)

In this study, feature selection plays a pivotal role in determining which input attributes will contribute to the machine learning model's development. To be considered for inclusion, an input feature must exhibit a meaningful relationship with the target attribute. The Pearson's correlation coefficient (PCC) serves as a critical metric for assessing these relationships. For instance, when examining the correlation between T_m(K) and HV (Fig. S1), a PCC score of 0.00 indicates an absence of correlation, rendering T_m(K) irrelevant for the hardness (HV) prediction model. Furthermore, to mitigate multicollinearity and redundancy, it's imperative to select input features that not only correlate strongly with the target variable but also exhibit weaker or no correlations with fellow input features.

In line with these principles, a selection criterion has been established in this study: only input features with an absolute PCC score of 0.2 or higher with the target feature are considered for inclusion in the final machine learning model. In the case of T_m(K), its PCC score of 0.00 leads to its exclusion from the model for hardness prediction. Similarly, AN's absolute PCC score of less than 0.2, despite being nonzero, deems it ineligible for the model. This stringent selection process ensures that only features with strong linear correlations with the target attribute are retained.

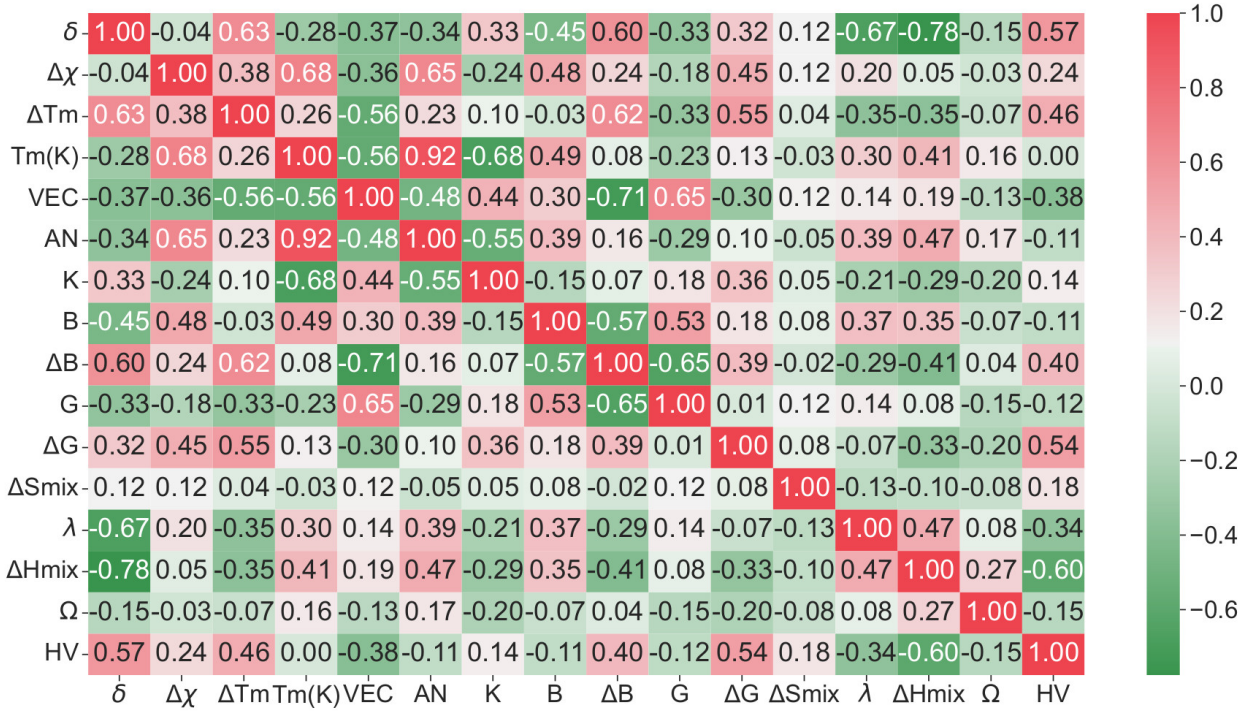

Figure S1: The simultaneous view of the correlationship among the 15 input features and with the HV feature in a hardness dataset can be enabled through the usage of a PCC heatmap. For the stronger correlationship between an input feature and HV feature, the value represented by a darker color (green or red) in the color scale shows the tendency of good relevance. In context of any two input features, inclusion of both of them in the aftermath of feature selection can be recommended only if they are weakly correlated with each other (represented by the light color in the color scale) and each of them are strongly correlated with the hardness feature.

S1.2. In-Depth Principal Component Analysis (PCA)

In the context of the hardness dataset (Fig. S3(c)), we examined the eigenvalues corresponding to its 19 principal components. These eigenvalues, ordered by magnitude, ranged from 4.29 (for ψ_1) to 0.00 (for ψ_{19}), with a total sum of $\sum_{i=1}^{19} \psi_i = 15.29$. The first principal component (PC 1) captured 28.06% of the total dataset information, while PC 2 contributed 26.42%, resulting in a cumulative explained variance (EV) of 54.48% for PC 1 and PC 2 together. PC 3, with an EV of 13.6%, pushed the cumulative EV to 68.08% for PC 1, PC 2, and PC 3. Impressively, the first three principal components retained over two-thirds of the dataset's information. Furthermore, the cumulative EV of

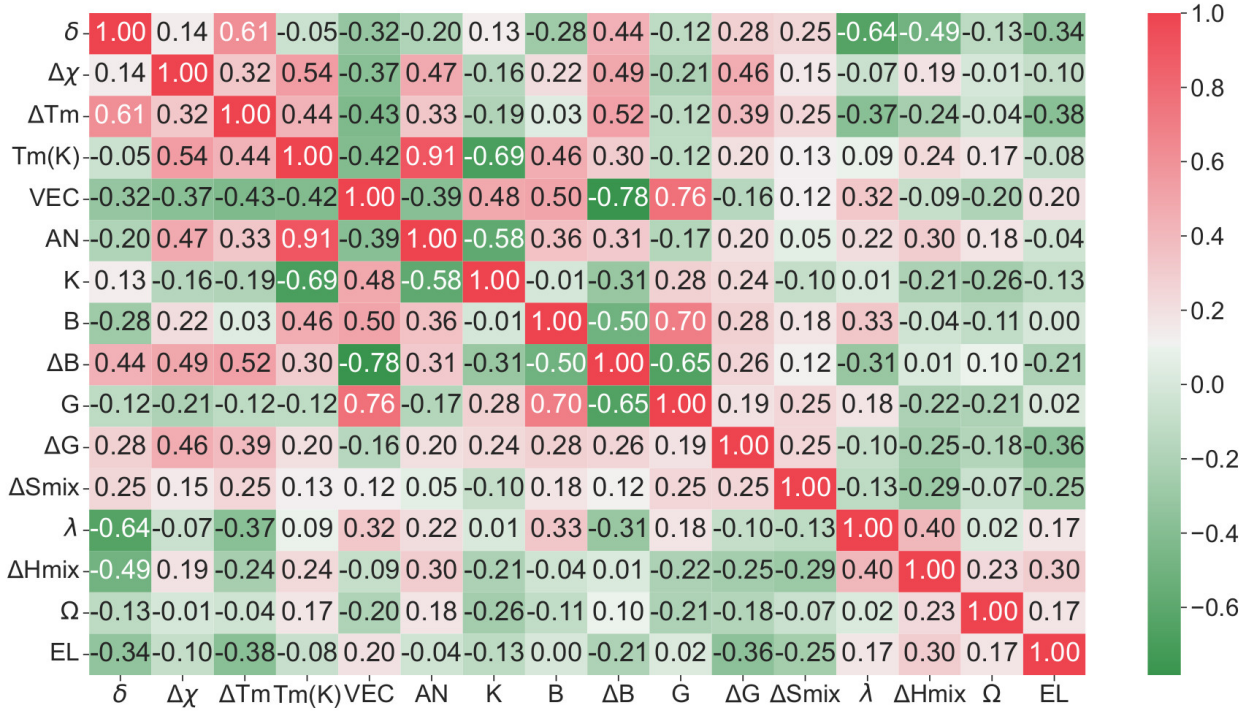

Figure S2: Pearson's correlation coefficient heatmap provides the simultaneous overview of the corelationship between the 15 input features of the original feature pool and with the elongation (EL) output feature. Any two input features are deemed maximally relevant and minimally redundant for the context of further use in the model if there exists a weaker correlationship between each other (represented by lighter green/red color in the color scale) whereas each of them has a stronger correlationship with the EL feature (represented by darker green/red color in the color scale).

the first eight principal components reached 92.27%, demonstrating their suitability for machine learning models. The remaining 11 less informative components, with a cumulative EV of 7.73%, were omitted.

The graphical representations of cumulative explained variances (EVs) for the datasets are presented in Fig. S3. In Fig. S3(a) and Fig. S3(b), corresponding to the hardness and elongation datasets without manufacturing route attributes, 15 principal components were considered. However, for simplicity, the horizontal axes are labeled up to 14 only. In Fig. S3(c), representing the hardness dataset with manufacturing route features, 19 eigenvalues were obtained. These eigenvalues, listed in descending order of magnitude, ranged from 4.29 to 0.0. The cumulative EV of the first three principal components was 68.08%, indicating their significance in retaining dataset information. Notably, the cumulative explained variance of the first eight principal components was 92.27%, validating their selection for machine learning. Consequently, these eight components were chosen, while the remaining 11 less informative features were discarded.

In the cases of the hardness dataset without manufacturing route features (Fig. S3(a)), elongation dataset without manufacturing route features (Fig. S3(b)), and elongation dataset with manufacturing route features (Fig. S3(d)), 7, 8, and 9 principal components were respectively required to capture over 90% of the explained variance. This strategic selection ensured substantial dimensionality reduction while preserving the dataset's critical information. The choice of the number of principal components was influenced by the magnitude of their eigenvalues, with larger eigenvalues signifying more significant features. For instance, in the hardness dataset with manufacturing route features (Fig. S3(c)), the cumulative EV for the first two principal components was 54.48%, while in the elongation dataset with manufacturing route features (Fig. S3(d)), it was 47.26%. This distinction justified the selection of 8 features for the hardness data and 9 features for the elongation data, ensuring the retention of over 90% of the information in each scenario.

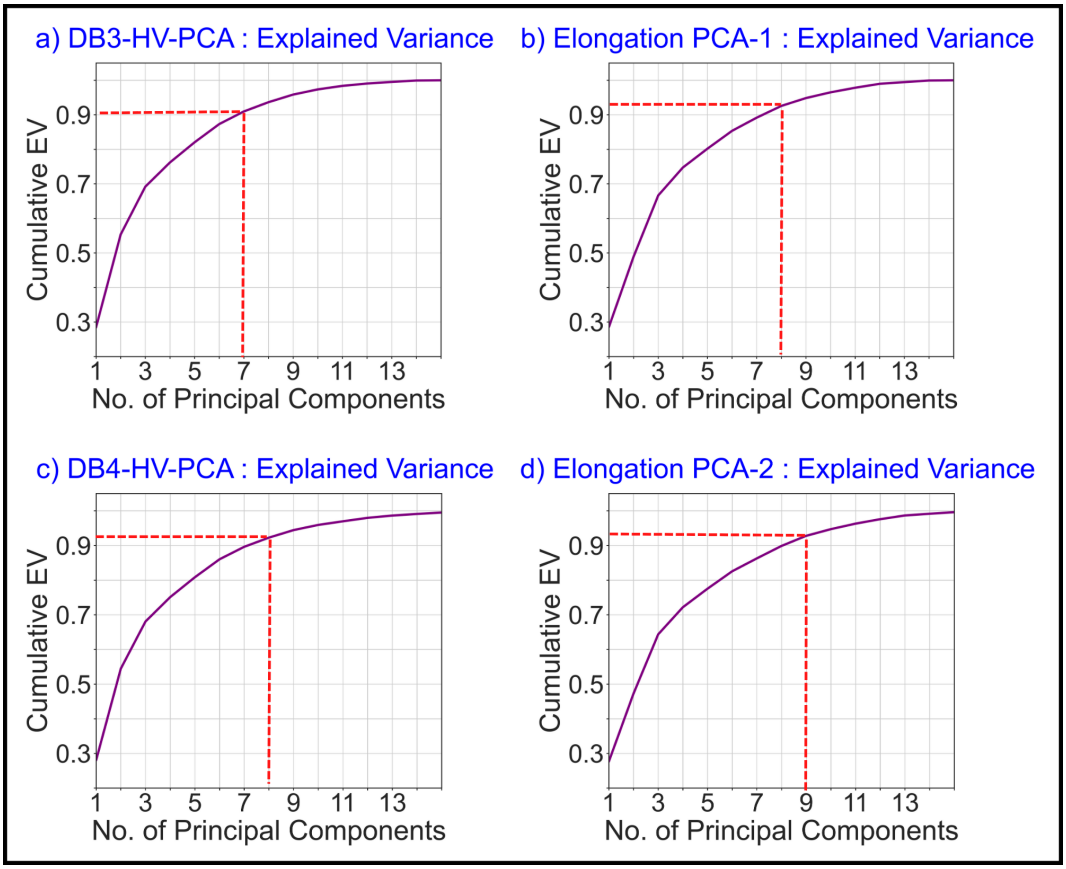

Figure S3: In the PCA carried out in the first step (PCA-1), the cumulative explained variance (EV) curves are obtained for (a) hardness and (b) elongation datasets excluding the manufacturing route (MR) features. Another PCA (a.k.a. PCA-2) is carried out again to obtain cumulative EV curves for (c) hardness and (d) elongation datasets including the MR features. The dotted lines are constructed in the images to highlight the minimum number of principal components that contribute to the cumulative EV larger than 90 % ($>$ 0.9). Illustrated through the use of dotted straight lines (green color), it is obvious from the criteria of information retention of above 0.9 that p takes the integer values of (a) 7, (b) 8, (c) 8, and (d) 9 in the four different datasets.

S1.3. Mathematical modeling of hardness and elongation datasets with PCA

For an input feature (X_k) of hardness/elongation database (D), there are N observations. The variance of the data for this input feature is defined as:

$$var(x) = \frac{1}{N-1}\sum_{i=1}^{N}(x_i - \bar{x})^2 \tag{1}$$

where, x_i is the element of a feature X_k. The quantity variance is used to understand the variation of dataset within a single feature e.g. variation of the mean atomic radius difference in the hardness dataset.

For the initial feature pool without fabrication route (MR) feature, there are 15 input features and with including MR feature, the list or pool consists of 19 features. In this section, the illustration of the methodology of PCA is done with the help of the hardness database (with 19 input features, i.e. 15 input features from the original feature pool of Table S1 + 4 MR feature). It must be noted that the same methodology has been applied for performing PCA in all the remaining three datasets (1 hardness dataset and 2 elongation datasets).

Having so many features in the hardness dataset,arises the topic of covariance, which is defined for any two features X_1 and X_2 by the following formula:

$$cov(x_1, x_2) = \frac{1}{N-1}\sum_{i=1}^{N}(x_{1,i} - \bar{x}_1)(x_{2,i} - \bar{x}_2) \tag{2}$$

In Eq. 2, $x_{1,i}$ is the observation of the variable X_1 and $x_{2,i}$ is the observation of the feature X_2. For an example, if mean atomic radius difference δ feature is chosen as the dimension X_1 and electronegativity asymmetry ($\Delta\chi_i$) as variable X_2, then relationship between the variation in δ of the hardness dataset to that of the change in $\Delta\chi_i$ is measured by $cov(x_1, x_2)$. And, if average melting temperature (T_m) is selected as the dimension X_3 , then the covariance between δ and T_m is denoted as $cov(x_1, x_3)$. It should be noted that $cov(x_1, x_2) = cov(x_2, x_1)$, and $cov(x_1, x_3) = cov(x_3, x_1)$. The covariance between two variables (attributes) can be positive, negative, or zero. A positive covariance indicates that the two features have a positive relationship whereas negative covariance shows that they have a negative relationship. If two attributes do not vary altogether with respect to each other, then they will display a zero covariance. A k-dimensional data has $\frac{k!}{(k-2)!\times 2}$ covariance values. In the initial feature pool consisting of 15 features and excluding the fabrication route (MR) feature, the number of covariance values $= \frac{15!}{(15-2)!\times 2} = 105$. When MR feature is included, the total dimension is 19 , and the total number of covariance values is $\frac{19!}{(19-2)!\times 2} = 171$. The number of variance values for list consisting of 15 features (excluding MR feature) is 15, and the feature pool consisting of 19 features (including MR feature) is 169

A variance-covariance matrix or simple, a covariance matrix, is a square matrix where the diagonal elements contain the variance and the non-diagonal elements contain the covariance. Since, $cov(x, y) = cov(y, x)$, it should be understood that the variance-covariance matrix is symmetrical about the main diagonal. The number of features in the hardness or elongation dataset determines the dimension of a variance-covariance matrix. The variance-covariance matrix (A) for a k-dimensional data is represented below:

$$A = \begin{bmatrix} var(x_1) & cov(x_1, x_2) & \dots & \dots & \dots & cov(x_1, x_{k-1}) & cov(x_1, x_k) \\ cov(x_1, x_2) & var(x_2) & \dots & \dots & \dots & cov(x_2, x_{k-1}) & cov(x_2, x_k) \\ \dots & \dots & & & & \dots & \dots \\ \dots & \dots & & & & \dots & \dots \\ \dots & \dots & & & & \dots & \dots \\ cov(x_1, x_{k-1}) & cov(x_2, x_{k-1}) & \dots & \dots & \dots & var(x_{k-1}) & cov(x_{k-1}, x_k) \\ cov(x_1, x_k) & cov(x_2, x_k) & \dots & \dots & \dots & cov(x_k, x_{k-1}) & var(x_k) \end{bmatrix} \tag{3}$$

For a dataset consisting of several features, a feature characterized with a larger variance will have more weightage in the model as compared to the feature with smaller variance. In order to ensure that all of the variables get a say over the outcome of the model, the features need to be standardized. In this study, the k features are standardized using *StandardScalar*. After the standardization procedure the mean of the data of each feature equals 0 whereas its variance is 1. Standardization automatically ensures the centering of the data as required by the PCA. The standardized hardness data matrix consisting of 19 features is denoted as D_H matrix. The size of the D_H matrix is s× k, where s = 614 (for training hardness dataset) is the number of observations, and k = 19 is number of input features. It is noteworthy to mention that the all of the elements of the main diagonal of the variance-covariance matrix of Eq. 3 equal to a unity value except for the 4 MR features as it was not standardized (no standardization to encoded categorical features). The structure of the covariance matrix (A_H) for the hardness dataset consisting of 19 input features is provided in the equation below:

In order to perform the PCA of the datasets of the MPEAs consisting of k features in the feature pool , it is first necessary to perform the Eigen decomposition of the variance-covariance matrix A_H. Defining the identity matrix I of size equal to that of A_H, it can be now possible to calculate the eigenvalues (ψ) of the square matrix A_H by the following formula:

$$det|A_H - \psi I| = 0 \tag{4}$$

With the eigenvalues ([ψ_1,ψ_2, ..., ψ_k]) computed using Eq. 4, the corresponding eigenvectors ([[v_1],[v_2], ..., [v_k]]) of A_H are then computed. Mathematically, the eigenvectors are defined as the family of non-zero vectors that satisfy the

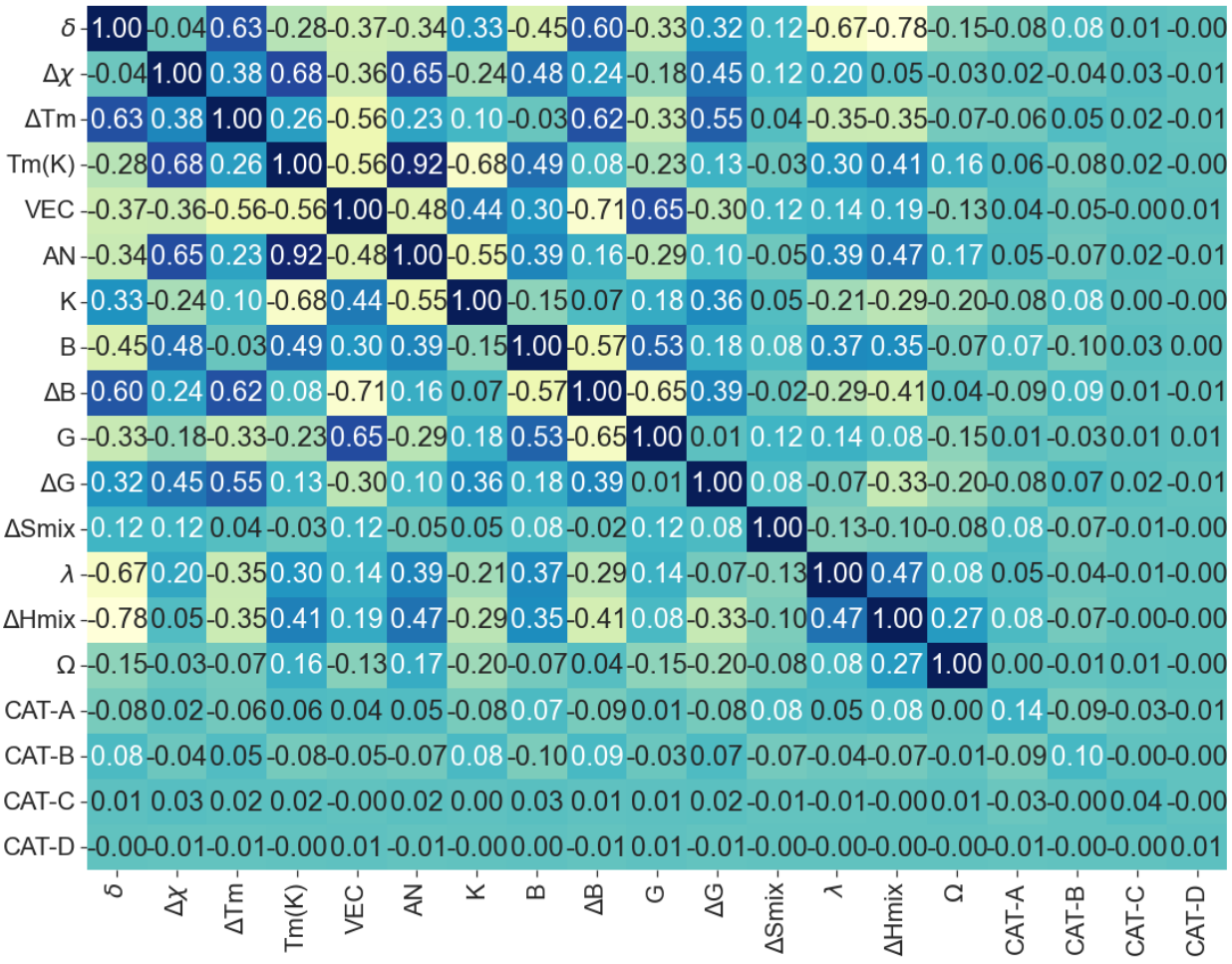

Figure S4: Structure of the covariance matrix (A_H) for the hardness dataset consisting of 19 input features

condition $A_H v = \psi v$. The computed values of eigenvalues (arranged in descending order) and their corresponding eigenvectors for A_H are listed below:
eigenvalues=[4.29, 4.04, 2.08, 1.07, 0.88, 0.79, 0.55, 0.41, 0.33, 0.23, 0.16, 0.15, 0.10, 0.07, 0.06, 0.05, 0.02, 0.01, 0.0] (the larger eigenvalue indicates more variance)

After the computation of eigenvalues and eigenvectors of the covariance matrix, the next step is to proceed towards finding the principal components and principal components scores. An eigenvector matrix (E) of size k× k is formed from the computed values of eigenvectors. The eigenvector corresponding to the largest eigenvalue is put as the first column, and the one corresponding to the lowest eigenvalue is put as the last column of the E matrix. Then the standardized data matrix (D_H) and the eigenvector matrix (E) are subjected to matrix multiplication. The resulting matrix P obtained from the matrix multiplication $D_H E$ provides an insight about the principal components of the dataset, and corresponding principal component scores. The variable corresponding to the first column of the P matrix is termed as the first principal component (PC 1), feature corresponding to the second column as PC 2, and the attribute corresponding to the last column is understood as PC 15. Any two principal components are uncorrelated to each other, which means they are orthonormal features.(PLEASE DRAW THE FIGURE OF PC 1 and PC 2 for the hardness data, and then show that their vectors are orthonormal, write in caption that the remaining PCs are not shown in the diagram.) The values or elements inside the transformed P matrix are called principal component scores. These PC scores represent the standardized features in the principal components space, ensuring that the PC 1 has the highest variance, followed by PC 2, and then by PC 3, and so on in the descending order.

-0.44	0.05	-0.07	-0.15	0.04	-0.18	-0.01	0.16	0.28	-0.12	-0.13	0.20	0.54	0.24	0.42	0.20	-0.04	-0.04	-0.00
0.00	-0.37	-0.32	-0.02	-0.06	0.11	-0.07	0.59	-0.25	0.29	0.00	-0.34	0.20	-0.27	0.10	0.01	-0.02	-0.03	0.00
-0.32	-0.23	-0.22	0.02	-0.08	-0.24	0.26	-0.21	0.57	0.07	0.07	-0.38	-0.27	-0.24	-0.00	-0.07	-0.01	0.04	-0.00
0.13	-0.46	-0.04	-0.11	0.10	-0.13	0.05	-0.07	-0.02	-0.12	-0.07	0.26	0.13	-0.01	-0.13	-0.03	-0.06	0.78	-0.00
0.25	0.37	-0.18	0.00	-0.12	0.04	0.19	0.31	0.13	0.18	0.05	-0.04	-0.38	0.32	0.36	0.18	-0.07	0.38	-0.00
0.14	-0.45	-0.00	0.01	-0.01	0.07	0.18	-0.02	0.07	0.20	-0.04	0.60	-0.30	-0.10	0.32	0.11	0.02	-0.35	0.00
-0.16	0.29	-0.27	0.36	-0.36	0.18	0.33	0.15	0.05	-0.02	-0.04	0.40	0.17	-0.29	-0.29	-0.13	0.02	0.08	-0.00
0.30	-0.13	-0.45	-0.04	0.02	-0.30	0.05	0.17	0.14	-0.19	-0.07	0.04	0.01	0.46	-0.45	0.03	0.06	-0.30	0.00
-0.39	-0.20	0.12	0.13	-0.11	0.24	-0.03	-0.09	-0.03	0.54	0.21	0.03	0.02	0.53	-0.29	0.06	0.00	0.07	-0.00
0.24	0.23	-0.36	-0.05	0.02	-0.32	-0.25	-0.40	-0.01	0.55	0.11	0.12	0.26	-0.17	0.06	0.02	-0.01	0.02	-0.00
-0.21	-0.14	-0.47	0.31	-0.19	0.06	-0.17	-0.34	-0.41	-0.36	0.10	-0.05	-0.15	0.16	0.30	0.06	-0.04	0.03	0.00
-0.03	0.03	-0.22	-0.75	-0.34	0.46	-0.04	-0.18	0.05	-0.05	-0.13	0.00	-0.02	-0.02	-0.07	-0.02	0.02	-0.02	-0.00
0.31	-0.12	-0.01	0.35	-0.05	0.45	-0.46	-0.04	0.54	-0.08	-0.05	-0.06	0.17	0.02	0.07	-0.00	-0.01	0.03	0.00
0.36	-0.13	0.15	0.10	-0.22	0.09	0.60	-0.29	-0.08	0.02	-0.02	-0.29	0.42	0.14	0.16	0.07	-0.03	-0.08	0.00
0.07	-0.10	0.32	-0.02	-0.79	-0.41	-0.28	0.12	0.01	-0.03	0.03	0.02	-0.04	-0.01	0.01	0.02	-0.01	0.00	-0.00
0.05	-0.01	0.00	-0.12	0.02	0.05	0.03	0.07	0.06	-0.18	0.76	0.06	0.09	-0.10	-0.03	0.23	0.20	0.00	0.50
-0.05	0.02	0.01	0.11	-0.01	-0.01	-0.03	-0.09	-0.06	0.08	-0.52	-0.09	-0.08	-0.10	-0.14	0.58	0.25	0.06	0.50
-0.00	-0.01	-0.02	0.01	-0.01	-0.04	0.00	0.02	-0.01	0.09	-0.17	0.01	0.01	0.18	0.21	-0.69	0.40	0.03	0.50
0.00	0.00	0.00	-0.00	0.01	-0.00	-0.01	-0.00	0.00	0.01	-0.07	0.02	-0.02	0.02	-0.05	-0.12	-0.85	-0.08	0.50
ν_1	ν_2	ν_3	ν_4	ν_5	ν_6	ν_7	ν_8	ν_9	ν_{10}	ν_{11}	ν_{12}	ν_{13}	ν_{14}	ν_{15}	ν_{16}	ν_{17}	ν_{18}	ν_{19}

Figure S5: Structure of the eigenvector matrix for the hardness dataset consisting of 19 input features

S2. Scatterplot of the variables of databases DB1-HV-PCC and DB1-EL-PCC

In the aftermath of the feature selection using PCC, it will be insightful if the visualization of the datasets of the databases DB1-HV-PCC and DB1-EL-PCC are performed. Seaborn library Waskom (2021) was utilized for the data visualization of the different features in the databases. The pairplots for the different features of the hardness database (8 input features + 1 hardness feature) were constructed using the seaborn library, and the pairplots are presented in Fig. S6. On the basis of maximum relevance and minimum redundancy criteria, the 8 input features δ, $\Delta\chi$, ΔT_m, VEC, ΔB, ΔG, λ, ΔH_{mix} have been selected using PCC from the initial pool of collected features, and stored in DB1-HV-PCC along with the HV feature. The value corresponding to number of components (N) has been chosen to select the hue of the pairplots. So, all of the points corresponding to medium entropy alloys (MEA) with $N < 4$ are represented with blue colored dots in a pairplot. Similarly, the feature points corresponding to high entropy alloy (HEA) with $N > 4$ are represented by dots of light brown colors. From the pairplots it is very clear to understand that the dataset consists of more number of HEA as compared to MEA.

In context of elongation datasets (DB1-EL-PCC database), the pairplots of Fig. S7 show the 7 features, namely, δ, ΔT_m, VEC, ΔB, ΔG, ΔS_{mix}, ΔH_{mix} and 1 EL feature. The seven input features have been screened with the help of PCC. Similar to the case of the pairplots of hardness data, the pairplots for elongation datasets also consists of more number of HEA than MEA. Comparing the two Figs. S6 and S6, it can be noted that the 6 input features δ, ΔT_m, VEC, ΔB, ΔG, ΔH_{mix} are common in the two databases DB1-HV-PCC and DB1-EL-PCC. The database DB1-HV-PCC consists of two additional input features $\Delta\chi$, and λ, unique to it and not consisted by DB1-EL-PCC. However, DB1-EL-PCC consists of ΔS_{mix} that is absent in DB1-HV-PCC.

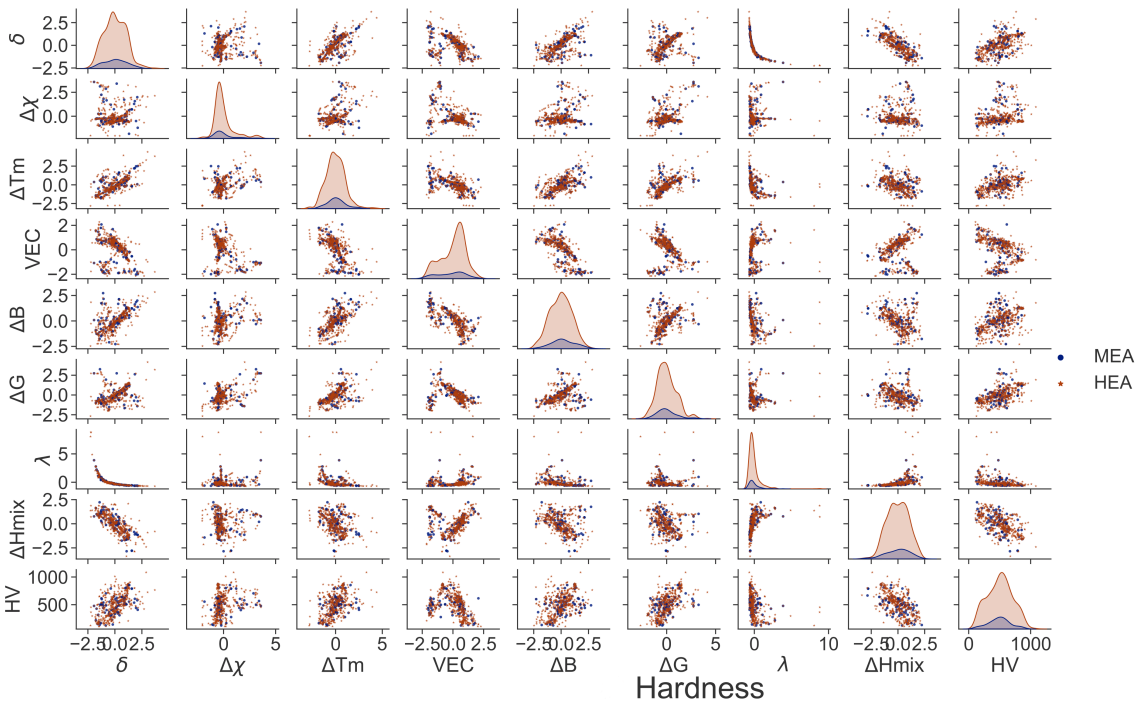

Figure S6: The distribution of the datasets of the features (8 input features and 1 HV feature) corresponding to the database DB1-HV-PCC is illustrated with the pairplots.

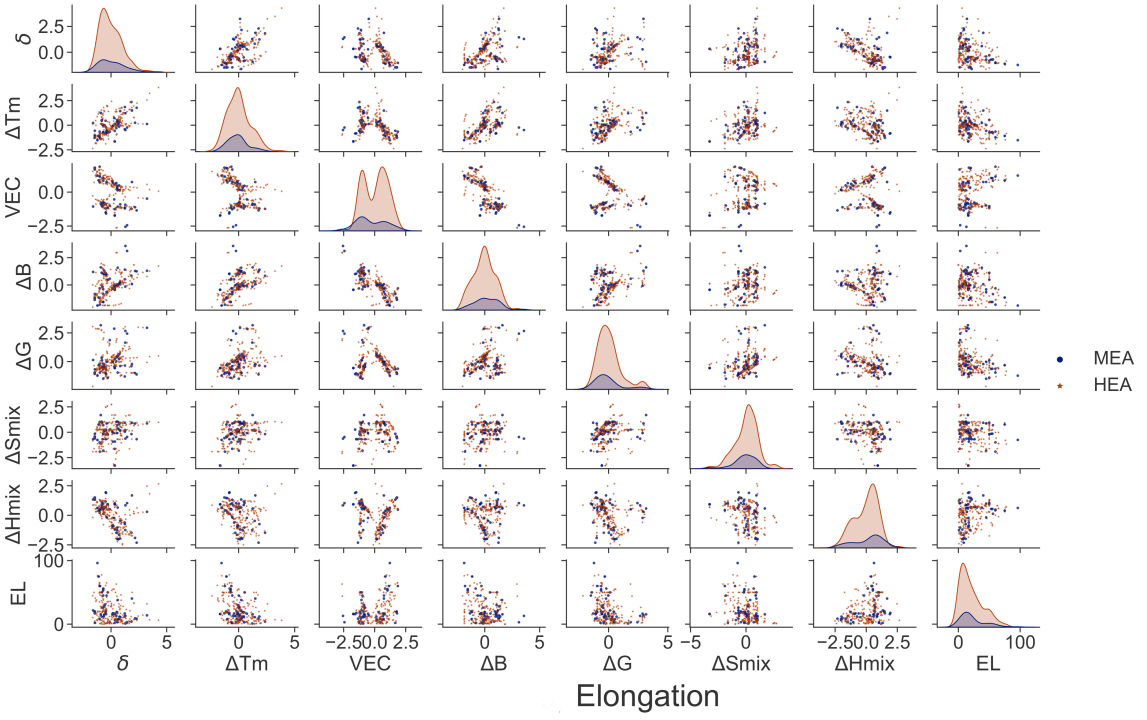

Figure S7: The pairplots reveal the distribution of the datasets of the features (7 input features and 1 EL feature) corresponding to the database DB1-EL-PCC.

S3. Hyper-parameter Tuning and Learning Curves of the Neural Networks

S3.1. Hyper-parameter Tuning

Hyper-parameter tuning is essential for obtaining the best configuration of the neural network models. The list consisting of the collective set of hyper-parameters tested for the set of ANN models is provided in able S2. These hyper-parameters are then specified individually for the individual NNs of the ensemble machine learning models as listed in Table S3 below. From the table, it can be inferred that same sets of hyperparameters have been utilized for the ANNs corresponding to a feature selection methodology and a given output feature. For an example, ANNs corresponding to DB1-HV-PCC and DB2-HV-PCC are constructed from features selected using Pearson's correlation coefficient method, and the output feature for both of these databases is hardness (HV). While the database DB1-HV-PCC does not include the features related to manufacturing route, the DB2-HV-PCC includes thes features in addition to those features recommended by PCC. Owing to the fact of the usage of a same feature selection technique, i.e. PCC and having the same output feature, i.e. hardness (HV); the two databases DB1-HV-PCC and DB2-HV-PCC have been assigned a same set of hyper-parameters.

Table S2: Hyper-Paramater value used to tune for best combination of hyper-parameters.

SN			Hyper parameters
1	Epochs	=	[100, 150, 200]
2	batch size	=	[2,4,6]
3	layers	=	[4,6,8]
4	neuron size	=	[32,48,64]
5	optimizer	=	[RMSprop, Adam, Nadam]
6	activation	=	[ReLU, selu, PReLU]
7	loss function	=	[mse, msle, huber with alpha=1.5]
8	drops	=	[0.05,0.075,0.1,0.2]
9	learning rate	=	[0.0001,0.00025,0.000375,0.0004,0.0005, 0.00075,0.001,0.005,0.01]
10	Regulirazation	:	[L1_L2 & L2]
	For weight initialization		
11	weight constraint	=	[1,2,3]
12	init weights	=	[uniform, normal, he_uniform]

S3.2. Learning Curves

The matrix *mean absolute error* was plotted for each epoch for the train and validation data. The Fig. S8 represent the train and validation mean absolute error for four different hardness models while the Fig. S9 is for four elongation models.

The plot presented in Fig. S8 clearly indicates that the MAE for the train and validation dataset for hardness model is in the range of 50-60. Similarly, Fig. S9 shows it is in the range 7-15 in the elongation model. The curve also points decline in MAE drastically for both the train and the validation datasets for epochs upto 50. As the epoch crosses 50, the decline is gradual and there seems to be a halt in decline once the epoch reaches over 120. So the choice of 150 epoch seems quite appropriate for this case.

The learning curve for the hardness model indicates that the model was trained quite well in comparison to the elongation model. There seems overfitting of the training model in the elongation. But that will hamper less in the model development as callback was used to save the model having minimum validation RMSE. As an advantage of

Table S3: The table provides a comprehensive overview of the hyper-parameters utilized within Artificial Neural Networks (ANNs) across various databases. It is crucial to highlight that ANNs sharing the same feature selection technique and output feature will exhibit identical sets of hyper-parameters. This standardized approach ensures a consistent and fair comparison between different ANN models, enhancing the reliability and interpretability of the results. These hyper-parameters play a pivotal role in shaping the performance and behavior of the ANNs, making them a critical aspect of the research methodology.

Feature Selection	Output Feature = Hardness (HV)	Output Feature = Elongation (EL)
PCC	Epochs = [150]	Epochs = [150]
	Batch size = [4]	Batch size = [6]
	Layers =[8]	Layers =[8]
	Neuron size = [48]	Neuron size = [48]
	Optimizer = ['Adam']	Optimizer = ['RMSprop']
	Activation = ['selu']	Activation = ['selu']
	Loss function =[mse]	Loss function =[mse]
	Drops = [0.05]	Drops = [0.05]
	Learning rate = [0.00075]	Learning rate = [0.001]
	Regulirazation =[L1_L2]	Regulirazation =[L1_L2]
	Weight constraint = [2]	Weight constraint = [2]
	Init weights = ['he_uniform']	Init weights = ['he_uniform']
PCA	Epochs = [150]	Epochs = [150]
	Batch size = [4]	Batch size = [6]
	Layers =[8]	Layers =[8]
	Neuron size = [48]	Neuron size = [64]
	Optimizer = ['Adam']	Optimizer = ['Nadam']
	Activation = ['selu']	Activation = ['selu']
	Loss function =[mse]	Loss function =[mse]
	Drops = [0.05]	Drops = [0.25]
	Learning rate = [0.00075]	Learning rate = [0.0005]
	Regulirazation =[L1_L2]	Regulirazation =[L1_L2]
	Weight constraint = [2]	Weight constraint = [2]
	Init weights = ['he_uniform']	Init weights = ['he_uniform']

this technique, the PCC-1 elongation model seems to have higher overfitting in Fig. S9 (a). But if we see result of individual elongation model, this model is the best performing model in elongation with $R^2 = 0.67$ and RMSE = 12. So, the effect of overfitting was avoided by taking the model at the epoch where validation RMSE is minimum.

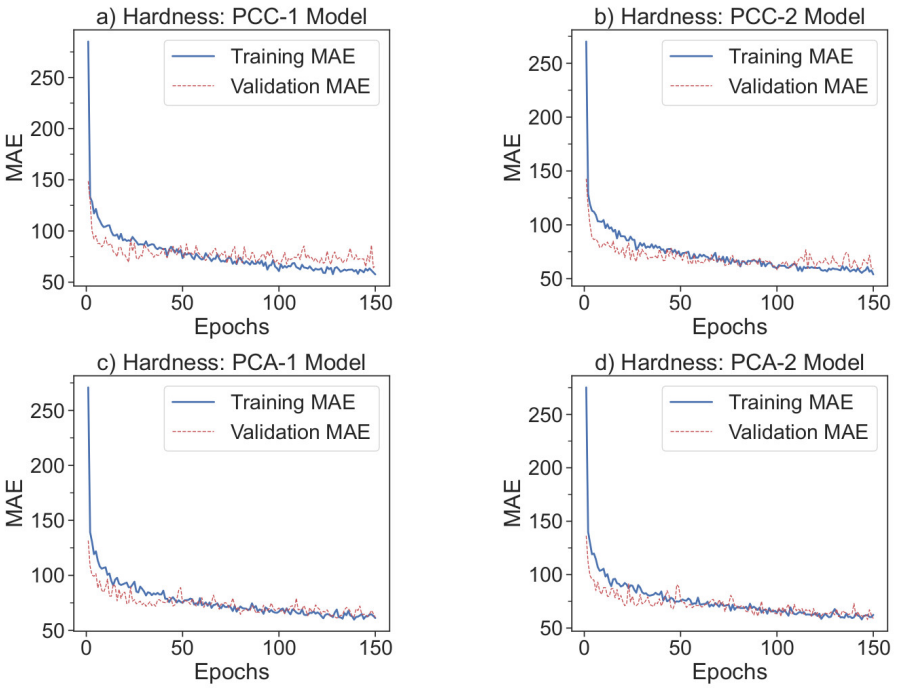

Figure S8: Mean absolute errors for individual ANN models of hardness corresponding to a) DB1-HV-PCC. b) DB2-HV-PCC. c) DB3-HV-PCA. d) DB4-HV-PCA.

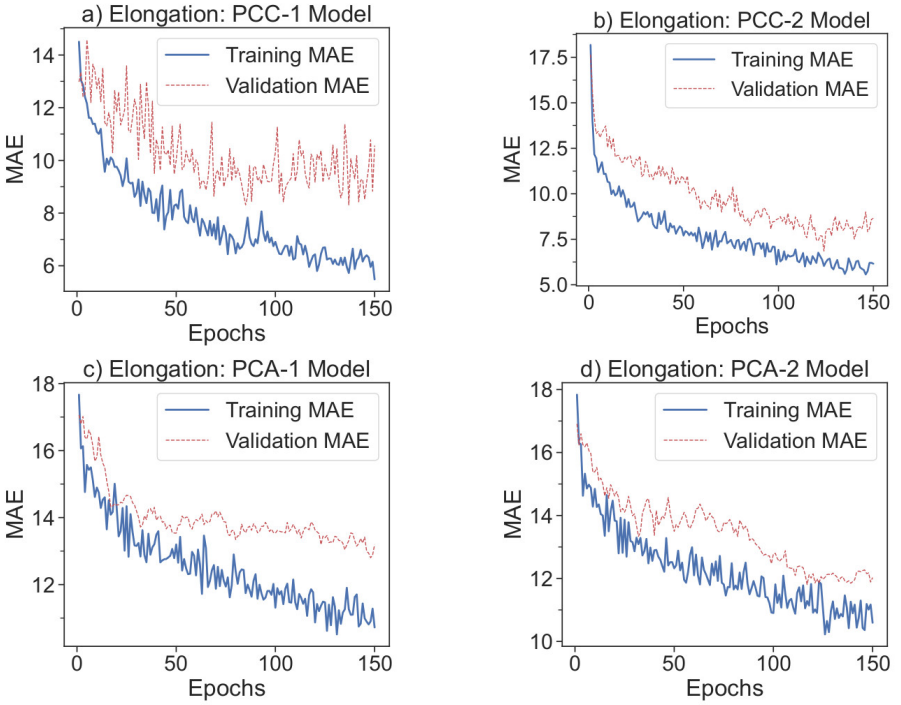

Figure S9: Mean absolute errors for individual ANN models of elongation corresponding to a) DB1-EL-PCC. b) DB2-EL-PCC. c) DB3-EL-PCA. d) DB4-EL-PCA.

S4. Results for MPEA: Optimized Hardness-Elongation synergy

For the $D1_xD2y(ZrHfNb)1-x-y$ alloy system, we have considered various dopant pairs and manufacturing routes to determine their influence on properties. The table summarizes the composition, manufacturing route, and resulting hardness (HV) and elongation (EL) properties for different alloy compositions. Notably, the [Cr,W] dopant pair, when fabricated through powder metallurgy, yields the highest hardness of 684.49 HV. The optimal alloy compositions and manufacturing routes for achieving maximum hardness and elongation values are detailed in Table S4.

In the case of the $D1_xD2y(VNbTa)1-x-y$ alloy system, we explore the effects of different dopant pairs and manufacturing routes on alloy properties. The table presents the composition, manufacturing route, and resulting hardness (HV) and elongation (EL) properties for various alloy compositions. It is observed that the [Cr,W] dopant pair, manufactured through powder metallurgy, exhibits the highest hardness value of 733.42 HV. The optimal alloy compositions and manufacturing routes for achieving maximum hardness and elongation values are highlighted in Table S4.

Table S4: Predicted composition proportions (x and y) of two dopant elements D1 and D2 in $D1_xD2_y(ZrHfNb)_{1-x-y}$ MPEAs for maximum hardness, maximum elongation, and optimum hardness-elongation pair, are presented in the table. The manufacturing routes (MR) corresponding to the property(-pair) and composition are also provided, and it should be noted that A, B, C and D respectively represent casting, wrought+misc, powder metallurgy and annealing. The composition design through the machine learning model is a very important application of the concept of inverse alloy design. The hardness is expressed in terms of HV and elongation is quantified as %.

Alloy systems	Composition proportion x and y of dopants for		
	Maximum hardness	Maximum elongation	Optimum hardness and elongation
$Cr_xW_y(ZrHfNb)_{1-x-y}$	HV = 684.49 Cr = 0.4 W = 0.5 MR = C	EL = 32.64 % Cr = 0 W = 0 MR = D	HV = 511.81 EL = 17.14 % Cr = 0.8 W = 0.1 MR = B
$Mo_xTa_y(ZrHfNb)_{1-x-y}$	HV = 457.86 Mo = 0.5 Ta = 0.2 MR = C	EL = 34.09 % Mo = 0.1 Ta = 0 MR = D	HV = 426.91 EL = 32.99 % Mo = 0 Ta = 0 MR = A
$W_xTa_y(ZrHfNb)_{1-x-y}$	HV = 502.41 W = 0.8 Ta = 0 MR = C	EL = 32.64 % W = 0 Ta = 0 MR = D	HV = 383.54 EL = 31.68 % W = 0 Ta = 0 MR = C
$Ti_xTa_y(ZrHfNb)_{1-x-y}$	HV = 415.75 Ti = 0.1 Ta = 0.4 MR = C	EL = 43.52 % Ti = 0.7 Ta = 0 MR = D	HV = 374.56 EL = 37.95 % Ti = 0.3 Ta = 0.4 MR = B

For the alloy system based on ZrHfNb, Figure 6 c) (from main article) highlights that $Cr_{0.8}W_{0.1}(ZrHfNb)_{0.1}$, when produced via the wrought procedure, exhibits excellent hardness at 511.81 HV and moderate elongation at 17.14%. This is significant for applications where achieving high hardness is paramount. Conversely, in technological applications that prioritize high ductility, the alloy $Ti_{0.3}Ta_{0.4}(ZrHfNb)_{0.3}$, manufactured using the same wrought process, offers an excellent elongation value of 37.95% with a lower hardness of 374.56 HV.

Table S4 presents data for the base ZrHfNb alloy, revealing hardness and elongation values of 426.91 HV and 32.99%, respectively, when fabricated through the casting procedure. When the same ZrHfNb alloy is manufactured

Table S5: Ensemble neural networks are deployed as a prediction model to determine the composition proportions (x and y) of two dopant elements D1 and D2 in $D1_xD2_y(VNbTa)_{1-x-y}$ corresponding to the constraints - maximum hardness, maximum elongation, and optimum hardness-elongation pair. The corresponding manufacturing (routes), namely A = casting, B = wrought + misc, C = sintering/powder metallurgy and D = annealing, are also presented along with the property/properties and compositions.

Alloy systems	Composition proportions x and y of dopants for Maximum hardness (HV)	Maximum elongation (%)	Optimum hardness-elongation
$Mo_xTi_y(VNbTa)_{1-x-y}$	HV = 623.21 Mo = 0.5 Ti = 0 MR = B	EL = 34.36 % Mo = 0.1 Ti = 0.8 MR = B	HV = 566.43 EL = 27.79 % Mo = 0.3 Ti = 0 MR = B
$Hf_xW_y(VNbTa)_{1-x-y}$	HV = 590.31 Hf = 0 W = 0.7 MR = C	EL = 31.70 % Hf = 0.3 W = 0 MR =D	HV = 454.77 EL = 29.87 % Hf = 0.3 W = 0 MR = B
$Zr_xW_y(VNbTa)_{1-x-y}$	HV = 590.31 Zr = 0 W = 0.7 MR = C	EL = 31.45 % Zr = 0.4 W = 0 MR =D	HV = 542.60 EL = 30.22 % Zr = 0.4 W = 0 MR = C
$Cr_xW_y(VNbTa)_{1-x-y}$	HV = 733.42 Cr = 0.5 W = 0.3 MR = C	EL = 26.45 % Cr = 0.7 W = 0 MR =A	HV = 575.87 EL = 23.73 % Cr = 0.7 W = 0 MR = B

using powder metallurgy, it exhibits hardness and elongation of 383.54 HV and 31.68%, respectively. Consequently, the first of the two alloys ($Cr_{0.8}W_{0.1}(ZrHfNb)_{0.1}$ and $Ti_{0.3}Ta_{0.4}(ZrHfNb)_{0.3}$) prepared via the wrought process is suitable for applications requiring high hardness, while the second one is better suited for applications requiring enhanced ductility.

It can be concluded that the wrought process is the recommended fabrication procedure for enhancing either hardness or elongation when producing MPEAs from the base ZrHfNb alloy. However, with ZrHfNb, there seems to be a trade-off between hardness and elongation, indicating that achieving optimal hardness-elongation synergy in this alloy, doped with the given set of elements and manufactured through the four different processes, is not straightforward.

When considering alloy combinations derived from the VNbTa MEA, specifically the $Cr_xW_y(VNbTa)_{1-x-y}$ and $Mo_xTi_y(VNbTa)_{1-x-y}$ systems fabricated using the wrought process, regions with a favorable blend of hardness-elongation synergy become apparent. This observation is clearly demonstrated in Fig. **6(c)** of the main text by the heights of the bars representing both hardness and elongation. For instance, $Cr_{0.7}(VNbTa)_{0.3}$, produced via the wrought process, is predicted to possess excellent hardness at 575.87 HV along with moderately good elongation at 23.73%. Consequently, the alloy $Cr_xW_y(VNbTa)_{1-x-y}$ with x=0.7 and y=0, manufactured using the wrought method (Table S5), is well-suited for structural applications where high hardness is preferred.

In the case of $Mo_xTi_y(VNbTa)_{1-x-y}$ fabricated via the wrought process, the same table reveals that at x=0.3 and y=0, it exhibits hardness and elongation values of 566.43 HV and 27.79%, respectively. Thus, the $Mo_{0.3}(VNbTa)_{0.7}$ MPEA demonstrates a hardness nearly equal to that of $Cr_{0.7}(VNbTa)_{0.3}$ but with improved ductility. It is estimated to possess an excellent hardness-ductility synergy, particularly favoring hardness. $Zr_{0.4}(VNbTa)_{0.6}$ MPEA, manufactured using powder metallurgy, is predicted to exhibit a hardness of 542.60 HV and elongation of 30.22%. This alloy also represents a perfect combination of hardness-ductility synergy, albeit leaning more toward ductility. Notably, these MPEAs with superior hardness-elongation synergy generally consist of four elements, with the proportion of the base

alloy VNbTa being relatively larger. In terms of the elements doped into the VNbTa system, wrought manufacturing, followed by powder metallurgy, are considered the two preferable methods for achieving a harmonious balance between elongation and hardness properties.

In contrast to alloys derived from the ZrHfNb system, MPEAs originating from the VNbTa base exhibit a more favorable hardness-ductility synergy, quantified by the standardized and summed values of optimal hardness and elongation features (refer to Eq. **3** in the main text). For the case of $Cr_{0.8}W_{0.1}(ZrHfNb)_{0.1}$ (manufactured using the wrought + misc route) has a standardized hardness of +0.084 but an elongation of -0.264, resulting in a negative objective function value of -0.1802. This places $Cr_{0.8}W_{0.1}(ZrHfNb)_{0.1}$ in the unfavorable category. On the other hand, $Ti_{0.3}Ta_{0.4}(ZrHfNb)_{0.3}$ (manufactured with the same wrought + misc process) exhibits a highly favorable standardized elongation (+0.83) but an undesirable standardized hardness (-0.61), yielding an objective function value of +0.217. While this objective function is positive, the negative hardness value makes this MPEA unsuitable for technological applications.

The maximum achievable positive value for the overall objective function in ZrHfNb-derived MPEAs is +0.2229, found in the case of $Mo_{0.6}(ZrHfNb)_{0.4}$ alloy fabricated using the casting process. In this system, standardized hardness and elongation values are -0.34 and +0.57, respectively. Lower values of the overall objective function in ZrHfNb-derived MPEAs can also be interpreted using the ternary plots of Figs. S10 and S12. For instance, the triangular diagrams corresponding to $Cr_xW_y(ZrHfNb)_{1-x-y}$, prepared via the wrought process, are positioned second from the top left corner in both figures. The region near the top corner of the triangle, highlighted by a rectangular box, represents maximum elongation and minimum hardness. Across the 32 ternary plots in these figures, it is generally observed that a given composition value of a $D1_xD2_y(ZrHfNb)_{1-x-y}$ alloy for a specific manufacturing route corresponds to above-average hardness when elongation is below average and vice versa. This observation suggests that doping the ZrHfNb alloy system with these dopant pairs is unsuitable when seeking hardness-ductility synergy.

In contrast, MPEAs derived from the VNbTa base alloy system offer solutions to mitigate the trade-off between hardness and ductility. $Mo_{0.3}(VNbTa)_{0.7}$ (MR = wrought + misc) and $Zr_{0.4}(VNbTa)_{0.6}$ (MR = sintering) represent composition values and manufacturing routes that result in positive standardized values for all three quantities: the objective function, hardness, and elongation. These alloys are recommended for applications requiring enhanced hardness and greater ductility. $Mo_{0.3}(VNbTa)_{0.7}$ alloy, for instance, has standardized hardness and elongation values of +0.36 and +0.296, respectively, resulting in a sum of +0.656. Similarly, the standardized values for hardness and elongation in $Zr_{0.4}(VNbTa)_{0.6}$ alloy are +0.24 and +0.42, leading to a sum of +0.6648 (the maximum sum observed so far). Interestingly, $Zr_xW_y(VNbTa)_{1-x-y}$ alloys exhibit positive standardized values for all three quantities—hardness, elongation, and the objective function—across various manufacturing routes. The triangular diagrams for $Zr_xW_y(VNbTa)_{1-x-y}$ for the four manufacturing routes are positioned in the top row in Figs. S11 and S13. The region near the mid-length of the left side of these triangles, highlighted with a rectangular box, consistently displays excellent hardness and ductility. This makes $Zr_xW_y(VNbTa)_{1-x-y}$ an optimal candidate for applications requiring outstanding hardness-ductility synergy.

In $Mo_xTi_y(VNbTa)_{1-x-y}$ alloys, three of the manufacturing routes, except casting, favor regions with a blend of high hardness and elongation. On the other hand, for $Cr_xW_y(VNbTa)_{1-x-y}$ MPEAs, casting, wrought, and annealing processes offer composition proportions that promote hardness-ductility synergy, exhibiting both high hardness and elongation. However, powder metallurgy does not favor this synergy. Notably, when using dopant pairs like Hf and W, the behavior of the VNbTa system is similar to that of the ZrHfNb alloy doped with [Cr,W], [Mo,Ta], [W,Ta], and [Ti,Ta] in most cases. This means that specific composition coordinates in the ternary diagrams of $Hf_xW_y(VNbTa)_{1-x-y}$ MPEA for wrought, sintering, and annealing procedures result in low hardness when elongation is high, and vice versa. For casting, overall hardness and elongation values for $Hf_xW_y(VNbTa)_{1-x-y}$ consistently remain below average throughout the composition points.

S5. Simulation setup for nanoindentation test of Multi-principal element Alloys

The nanostructures of CoCrNi and $CoCrNiNb_{0.6}$ MPEAs are modeled as nanoslabs of dimensions $L_x \times L_y \times L_z$ as shown in Fig. S14. A unit cell of face centered cubic (FCC) structure consisting of equiatomic proportions of Co, Cr and Ni is replicated in X, Y and Z directions to construct a supercell of dimensions $L_x = L_y = 178.55$ Å, and $L_z = 214.26$ Å. For the construction of the nanoslab of $CoCrNiNb_{0.6}$ MPEA, a unit cell of hexagonal closed pack (HCP) crystal structure consisting of the correct proportions of the constituent elements Co, Cr, Ni and Nb, is defined first. Replication in three directions is then performed upon this unit cell to form a supercell. During the replication task, an

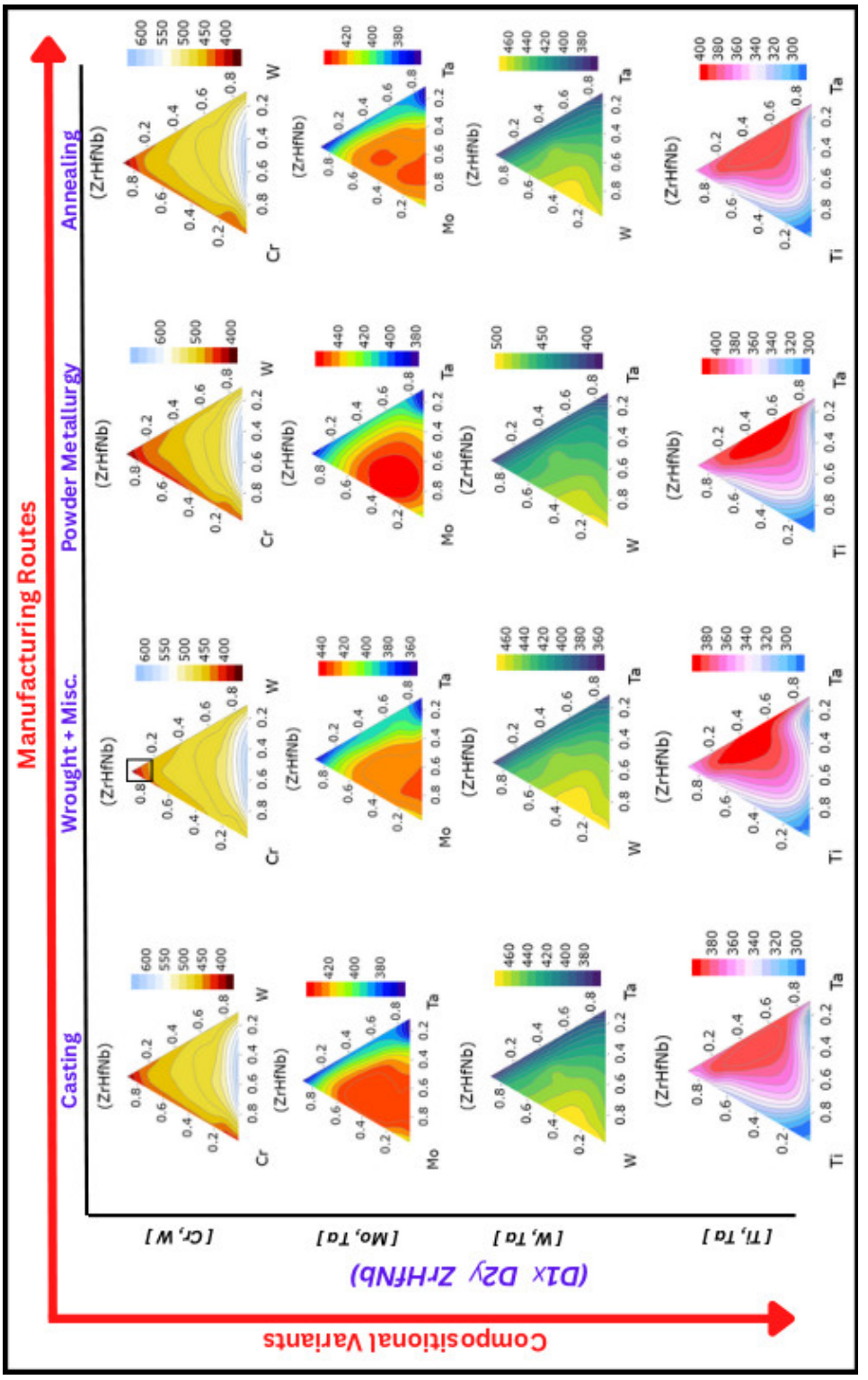

Figure S10: Ternary diagrams for hardness of $D1_xD2_y(ZrHfNb)_{1-x-y}$ MPEA with x as the proportion of dopant D1 and y is the proportion of D2. In the graphical representation, the variants of pair of dopant elements [D1, D2], namely, [Cr, W], [Mo, Ta], [W, Ta], and [Ti, Ta] are shown along the vertical axis, and the variants representing the manufacturing routes (casting, wrought + misc, powder metallurgy and annealing) are shown in the horizontal axis. The unit of the numbers in the color scale bar is HV. In case of $Cr_xW_y(ZrHfNb)_{1-x-y}$ (MR = wrought + misc), the corner region higlighted by the rectangular box shows the composition values with very low hardness. The dopant pair [Cr,W] are estimated as the most preferrable candidates in terms of imparting the large hardness values to the base ZrHfNb system. Powder metallurgy or sintering is seen as the most promising manufacturing route for obtaining $D1_xD2_y(ZrHfNb)_{1-x-y}$ MPEA with elevated hardness.

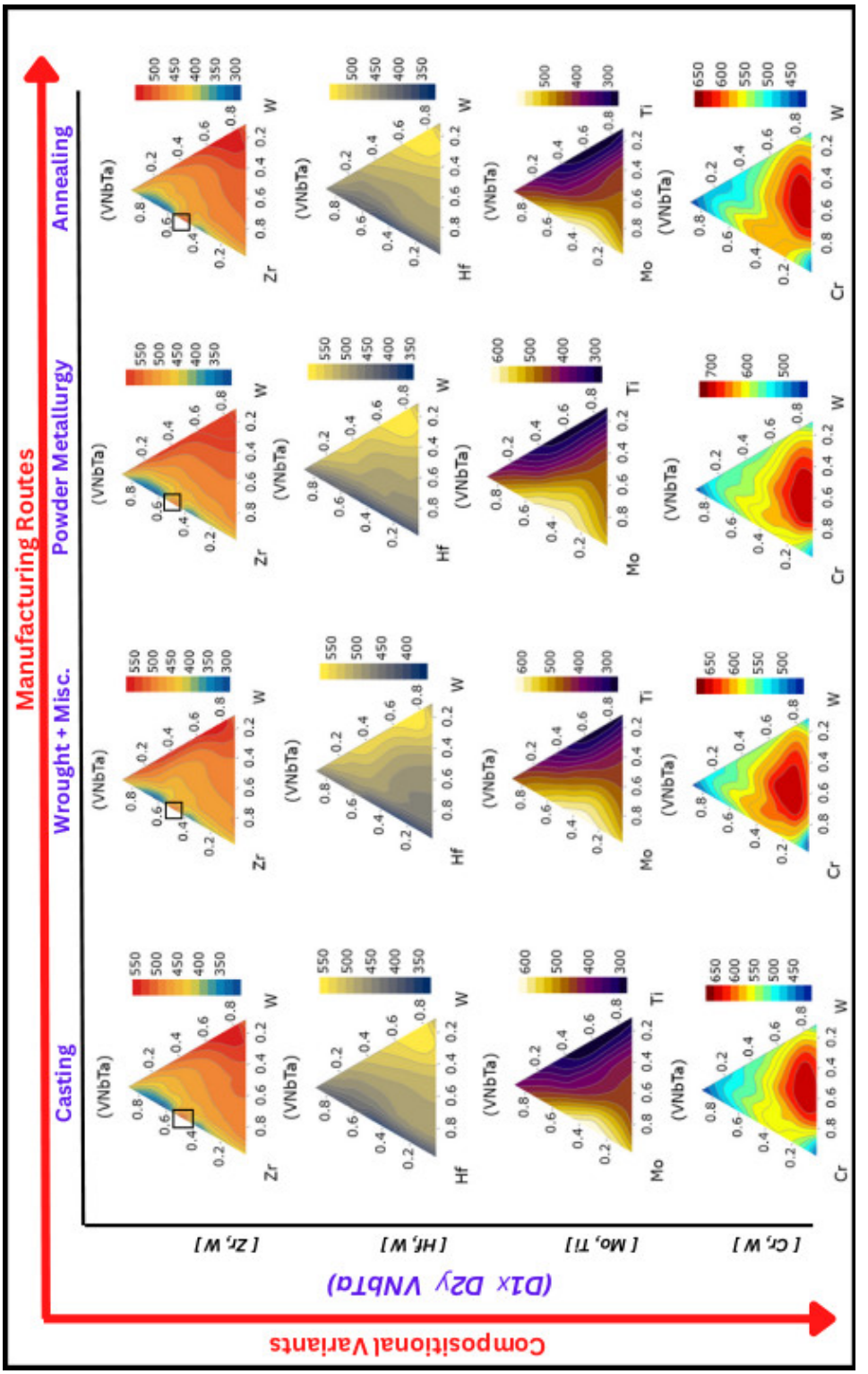

Figure S11: Hardness distribution in $D1_xD2_y(VNbTa)_{1-x-y}$ MPEA shown to be influenced not only by the composition variables but also by the manufacturing procedure involved. In $D1_xD2_y(VNbTa)_{1-x-y}$ MPEA , x represents the proportion of dopant D1 and y depicts the proportion of another dopant D2. The units of numbers of color scale corresponding to the ternary plots for hardness feature is HV. The dopant pairs [D1, D2] = [Zr, W], [Hf, W], [Mo, Ti] and [Cr, W] are the attributes affecting the composition design. Similarly, casting, wrought + misc, sintering (powder metallurgy) and annealing are the four categories of manufacturing routes. Among all of the triangular plots, the prediction diagram for $Cr_xW_y(VNbTa)_{1-x-y}$ corresponding to powder metallurgy possesses the regimes exhibiting the maximum hardness value larger than 700 HV, thus confirming that [Cr,W] dopant pair and sintering are the most preferred attributes for obtaining the MPEA with the largest hardness In context of $Zr_xW_y(VNbTa)_{1-x-y}$ (all manufacturing routes), the regime near the mid-length of left side of the triangles as higlighted by the rectangular box shows the composition values with relatively large hardness (above average value).

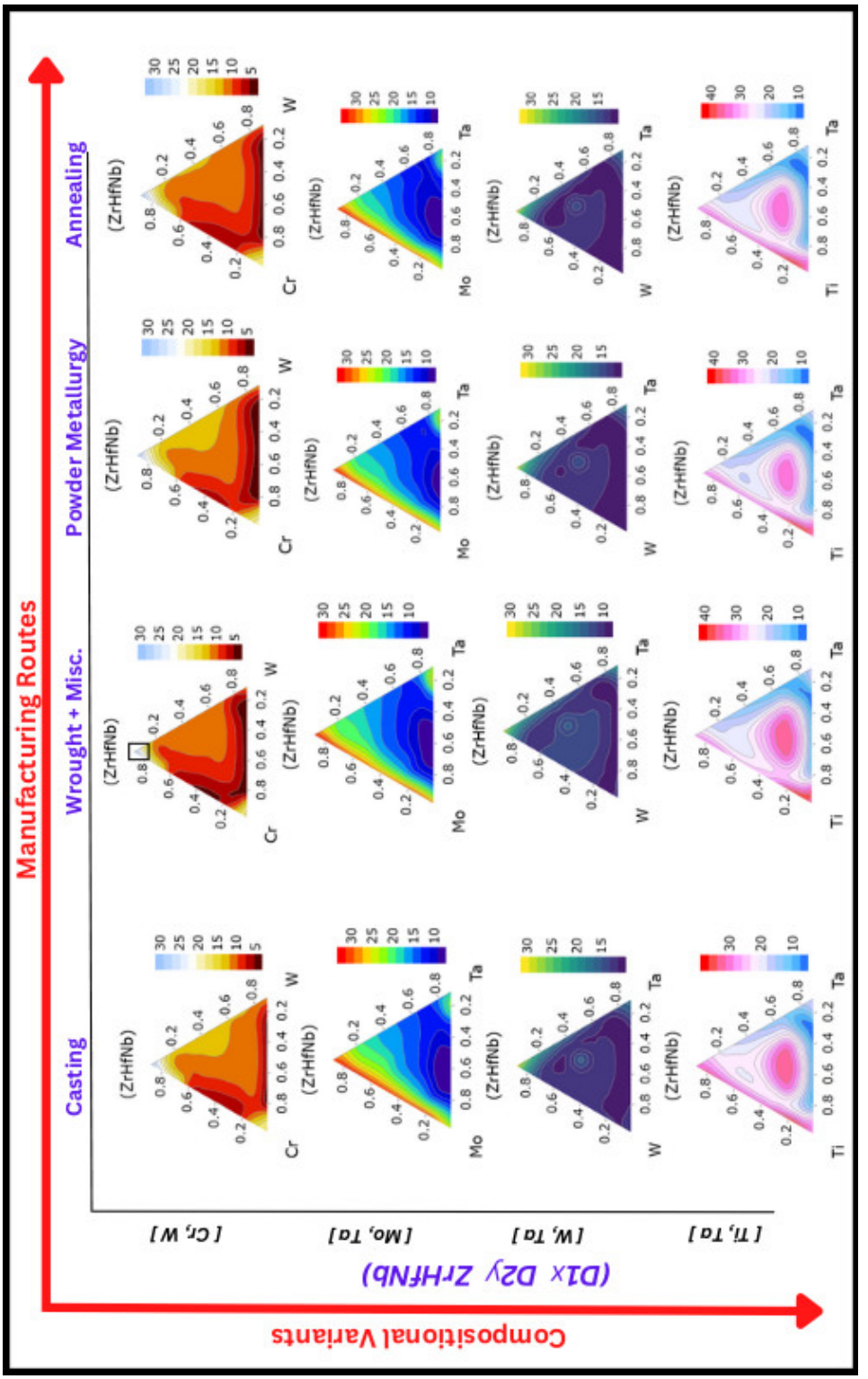

Figure S12: Influence of manufacturing routes and composition in the distribution of elongation feature in $D1_xD2_y(ZrHfNb)_{1-x-y}$ MPEA where, x as the proportion of dopant D1 and y is the proportion of D2. In the images, the pair of dopant elements [D1, D2], namely, [Cr, W], [Mo, Ta], [W, Ta], and [Ti, Ta] change along the vertical axis, and the variants representing the fabrication routes (casting, wrought + misc, powder metallurgy and annealing) are presented the horizontal axis. The numbers in color scale bar are expressed in terms of %. In context of $Cr_xW_y(ZrHfNb)_{1-x-y}$ (MR = wrought + misc), the corner region higlighted by the rectangular box corresponds to the alloy composition with large elongation value. For in-silico design with the dopant pair [Ti,Ta], large proportion of Ti and absence of Ta, is estimated to favour the elongation increment in the base ZrHfNb system. $Ti_{0.7}(ZrHfNb)_{0.3}$ MPEA prepared through annealing process is estimated to possess an unusually high elongation of value = 43.52 %..

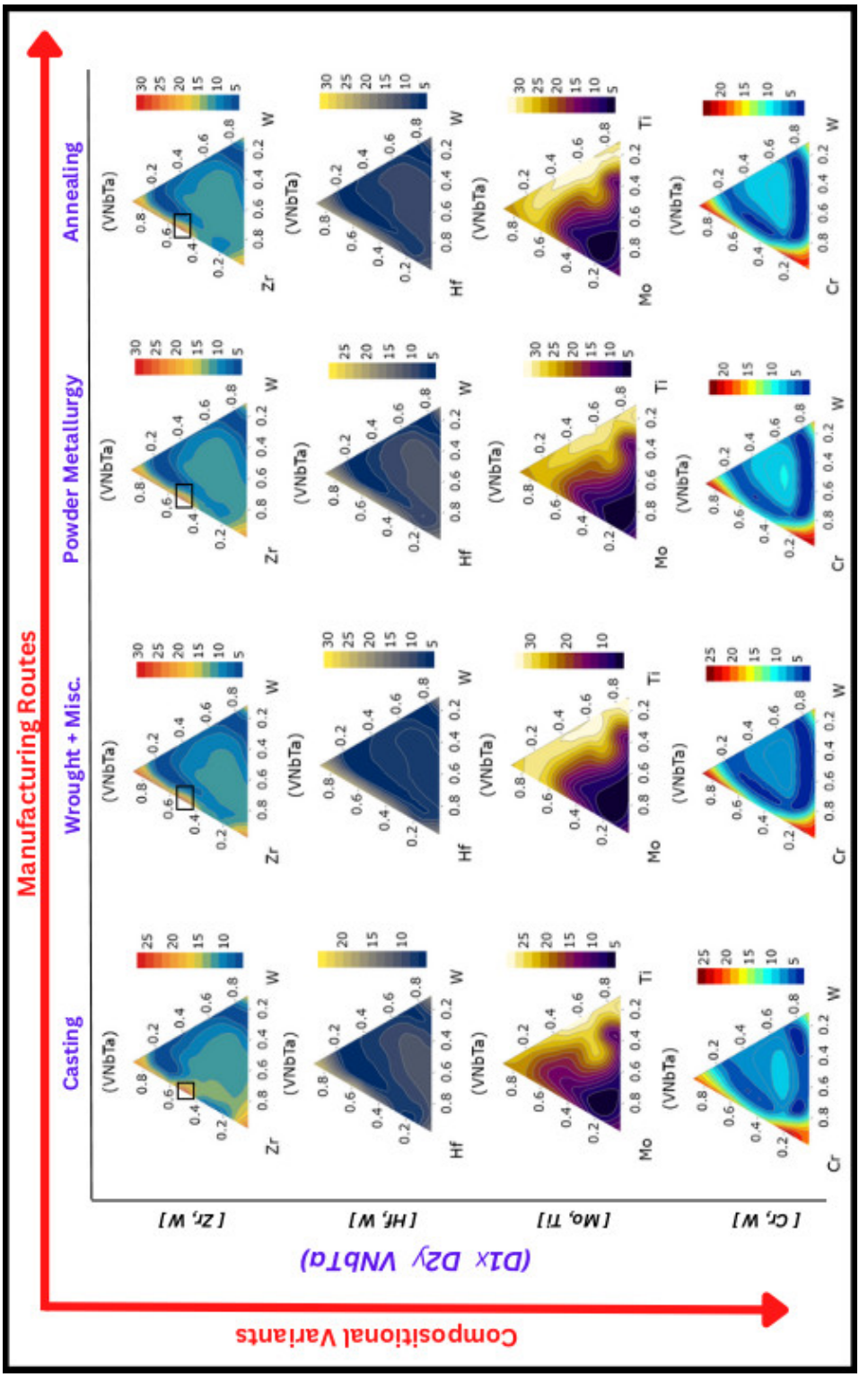

Figure S13: Elongation distribution in $D1_xD2_y(VNbTa)_{1-x-y}$ MPEA is affected not only by the composition variables but also by the manufacturing procedure involved. In the $D1_xD2_y(VNbTa)_{1-x-y}$ MPEA , x quantifies the proportion of dopant element D1 and y represents the proportion of second dopant element D2. The numbers of color scale bar corresponding to these ternary plots for elongation attribute are expressed in terms of %. The dopant pairs [D1, D2] = [Zr, W], [Hf, W], [Mo, Ti] and [Cr, W] are considered as the variables affecting the composition design. Moreover, casting, wrought + misc, sintering (powder metallurgy) and annealing are the four primary categories of fabrication routes. In the images corresponding to [Mo,Ti] dopant pair and wrought + misc fabrication route, the alloy composition $Mo_{0.1}Ti_{0.8}(VNbTa)_{0.1}$ is estimated to possess an elongation value of 34.36 % and is inferred as the largest possible value of elongation among all of the compositions and manufacturing routes represented by the 16 triangular diagrams. For $Zr_xW_y(VNbTa)_{1-x-y}$ (in all of the manufacturing routes), the region at the vicinity of the mid-length of left side of the triangles higlighted by a rectangular box shows the composition values with relatively large elongation (above average value).

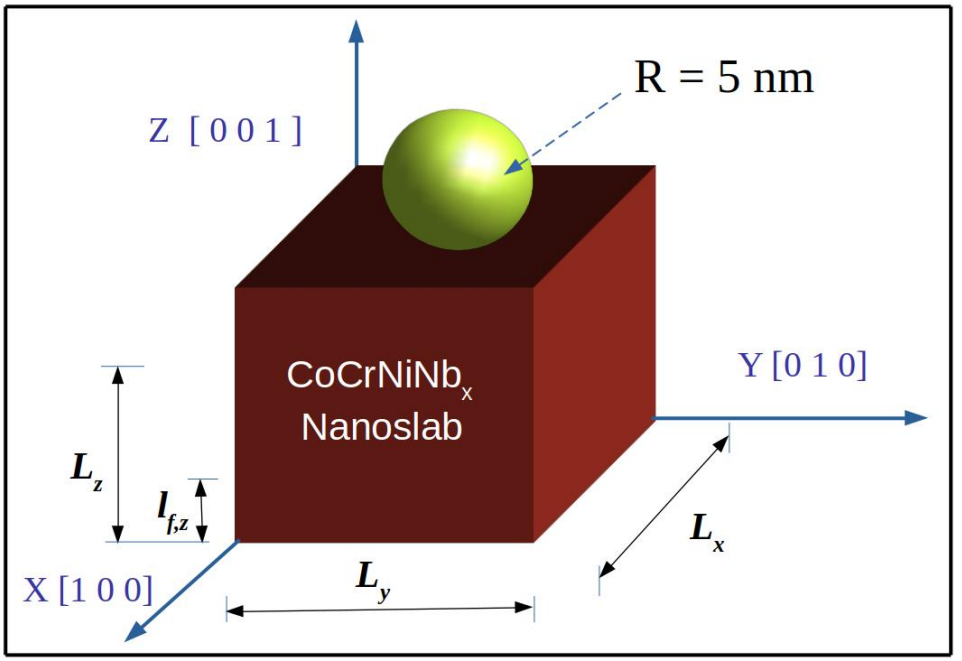

Figure S14: In the schematic sketch for nanoindentation test using a spherical indenter of radius (R) = 5 nm, the composition proportion x = 0 for CoCrNi medium entropy alloy, and x = 0.6 for $CoCrNiNb_{0.6}$ MPEA. In context of the CoCrNi supercell (constructed from FCC unit cell) , $L_x = L_y = 178.55$ Å, and $L_z = 214.26$ Å. For $CoCrNiNb_{0.6}$ supercell (built in an orthogonal mode for HCP unit cell) are $L_x = 203.816$ Å, $L_y = 207.943$ Å, and $L_z = 228.624$ Å. The atoms within the vertical distance of $l_{f,z} = 60$ Å from the base of the both nanostructures, are rigidly fixed in the entire duration of the simulation run.

operation is conducted to build it as an orthogonal supercell of $L_x = 203.816$ Å, $L_y = 207.943$ Å, and $L_z = 228.624$ Å. While the CoCrNi nanoslab consists of a total of 600000 atoms, the nanoslab of $CoCrNiNb_{0.6}$ MPEA includes 602688 atoms. It is assumed that the X, Y and Z axes are along crystallographic directions [1 0 0], [0 1 0] and [0 0 1] respectively. It is to be noted that the computational domain of Fig. S14 consists of two regions: top (active region which is being indented) and the bottom (fixed region). The atoms in the bottom region are maintained static during the entire simulation duration in order to ensure the rigid support and stability. This static region spans a length $l_{f,z} = 60$ Å upward from the base. The active region has then a length = L_z - $l_{f,z}$. The non-atomic rigid and repulsive sphere having radius (R) = 50 Å, is initially about to touch the top surface of the slab in such a way that the gap between them is a fraction of 1 Å. Upon touching the atoms of the MPEAs present in the nanostructures, the indenter will exert the following repulsive force P(r):

$$P(r) = \begin{cases} -K(r-R)^2; & r < R \\ 0; & r \geq R \end{cases} \tag{5}$$

where, K is termed as the specified force constant and has a value of 1000 $\frac{eV}{Å^3}$, and r is the variable distance from a random atom to the center point of the indenter. Upon the start of the simulation run, the indenter traverses vertically downward with a velocity of 0.5 Å/ps.

The nanoslabs of CoCrNi MEA and $CoCrNiNb_{0.6}$ MPEA constructed for the purpose of the simulations are presented in Fig. S15. The atomic interactions among the Co, Cr and Ni atoms in the CoCrNi and $CoCrNiNb_{0.6}$ MPEAs nanoslabs is described with the help of Embedded Atom Method (EAM) potential. The interaction of the pairs Nb-Nb and Nb-Ni in context of $CoCrNiNb_{0.6}$ MPEAs nanoslab, is also expressed with the help of EAM potential. Finally, the interaction Nb-Co and Nb-Cr in the $CoCrNiNb_{0.6}$ nanostructure is described with the usage of Morse potentials.

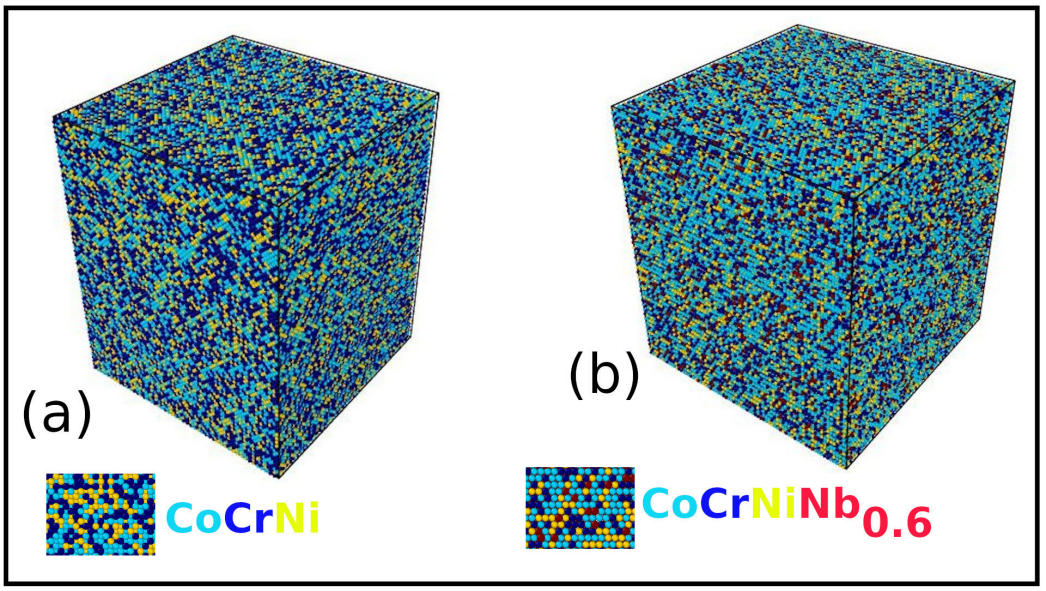

Figure S15: The nanoslabs of (a) CoCrNi and (b) $CoCrNiNb_{0.6}$ MPEAs are shown in the image. The atoms in the nanoslabs are identified through the colors of the fonts used in the symbol for the constituent element of the alloy. That is the atoms of Co, Cr, Ni and Nb are represented respectively by spheres of light blue, dark blue, yellow and red colors.

References

Fang, S., Xiao, X., Xia, L., Li, W., & Dong, Y. (2003). Relationship between the widths of supercooled liquid regions and bond parameters of mg-based bulk metallic glasses. *Journal of Non-Crystalline Solids*, *321*, 120–125. doi:10.1016/S0022-3093(03)00155-8.

Guo, S., Ng, C., Lu, J., & Liu, C. (2011). Effect of valence electron concentration on stability of fcc or bcc phase in high entropy alloys. *Journal of Applied Physics*, *109*, 103505. doi:10.1063/1.3587228.

Senkov, O., Wilks, G., Miracle, D., Chuang, C., & Liaw, P. (2010). Refractory high-entropy alloys. *Intermetallics*, *18*, 1758–1765. doi:10.1016/j.intermet.2010.05.014.

Singh, A. K., Kumar, N., Dwivedi, A., & Subramaniam, A. (2014). A geometrical parameter for the formation of disordered solid solutions in multi-component alloys. *Intermetallics*, *53*, 112–119. doi:10.1016/j.intermet.2014.04.019.

Takeuchi, A., & Inoue, A. (2005). Classification of bulk metallic glasses by atomic size difference, heat of mixing and period of constituent elements and its application to characterization of the main alloying element. *Materials Transactions*, *46*, 2817–2829. doi:10.2320/matertrans.46.2817.

Waskom, M. L. (2021). seaborn: statistical data visualization. *Journal of Open Source Software*, *6*, 3021. doi:10.21105/joss.03021.

Yang, X., & Zhang, Y. (2012). Prediction of high-entropy stabilized solid-solution in multi-component alloys. *Materials Chemistry and Physics*, *132*, 233–238. doi:10.1016/j.matchemphys.2011.11.021.